Important Notice

This copy may be used only for the purposes of research and private study, and any use of the copy for a purpose other than research or private study may require the authorization of the copyright owner of the work in question. Responsibility regarding questions of copyright that may arise in the use of this copy is assumed by the recipient.

THE UNIVERSITY OF CALGARY

Improving Seismic Resolution with Nonstationary Deconvolution

by

Alana R. Schoepp

A THESIS

SUBMITTED TO THE FACULTY OF GRADUATE STUDIES

IN PARTIAL FULFILLMENT OF THE REQUIREMENTS FOR THE

DEGREE OF MASTER IN SCIENCE

DEPARTMENT OF GEOLOGY AND GEOPHYSICS

CALGARY, ALBERTA

NOVEMBER, 1998

© Alana R. Schoepp 1998

THE UNIVERSITY OF CALGARY

FACULTY OF GRADUATE STUDIES

The undersigned certify that they have read, and recommend to the Faculty of Graduate Studies for acceptance, a thesis entitled "Improving seismic resolution with nonstationary deconvolution" submitted by Alana R. Schoepp in partial fulfillment of the requirements for the degree of Master of Science.

Supervisor, G. F. Margrave, Geology and Geophysics

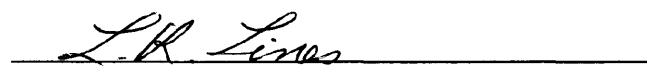

L. R. Lines, Geology and Geophysics

L. P. Bos, Mathematics and Statistics

4 Jan 1999

date

ABSTRACT

Nonstationary deconvolution operators can be designed directly from the seismic data and applied to the data using nonstationary filtering techniques. Such operators can be continuously time-variant and have any desired amplitude or phase spectra. The operator design uses time-variant Fourier spectra measured directly from the seismic data, which are smoothed, inverted and combined with a minimum-phase spectrum, if desired. This method of nonstationary deconvolution (NSD) approximately corrects the seismic data for the effects of anelastic attenuation, frequency dispersion, and source signature. The result is a one-dimensional nonstationary operation that extends the range of stationary deconvolution to a type of data-driven inverse-Q filter.

NSD has been applied to real seismic data and the results have been compared to results from Wiener deconvolution and inverse-Q filtering. The datasets deconvolved with NSD show improved vertical resolution and improved reflection character as compared to results from the other methods.

ACKNOWLEDGEMENTS

First, I would like to thank my supervisor and mentor, Gary Margrave, for his guidance and support throughout this degree. His patience and commitment have been a source of inspiration to me. I would also like to acknowledge the CREWES project support staff, especially Henry Bland, Darren Foltinek, Colin Potter, Brian Hoffe, and Han-xing Lu for their technical support and friendship. I'm grateful to my fellow students for their help and companionship. Finally, I wish to thank my family for their understanding and encouragement.

I would like to thank the CREWES Project and its sponsors for providing me with an excellent opportunity and environment for learning and research.

TABLE OF CONTENTS

APPROVAL PAGE ..... **I**

ACKNOWLEDGEMENTS ..... **IV**

TABLE OF CONTENTS ..... **V**

LIST OF TABLES ..... **IX**

LIST OF FIGURES ..... **X**

STRUCTURE OF THESIS ..... **XIV**

CHAPTER 1: INTRODUCTION **1**

1.1 OVERVIEW OF THE INTRODUCTION 1

1.2 ANELASTIC ATTENUATION 1

1.3 ADDITIONAL ATTENUATIVE MECHANISMS 8

1.4 NONSTATIONARITY 11

1.5 THE STATIONARY CONVOLUTIONAL MODEL AND SOURCE SIGNATURE 12

1.6 SPECTRAL RATIO METHOD OF Q ESTIMATION 15

1.7 SURFACE CONSISTENT MODEL 17

1.8 MINIMUM PHASE 19

1.8.1 Definition of minimum phase *19*

1.8.2 The minimum-phase assumption *19*

1.8.3 Estimation of minimum-phase spectrum *21*

1.8.4 Problems associated with digital minimum-phase estimation *22*

1.9 DECONVOLUTION AND INVERSE-Q FILTERING 27

1.9.1 Stationary deconvolution *28*

1.9.2 Inverse-Q filtering *32*

1.9.3 NSD *36*

CHAPTER 2: NONSTATIONARY FILTERS AND TIME-FREQUENCY ANALYSIS METHODS **38**

2.1 INTRODUCTION 38

2.2 NONSTATIONARY FILTERING 38

2.3 TIME-FREQUENCY DECOMPOSITION TECHNIQUES 41

2.3.1 Time-variant spectra *41*

2.3.2 Instantaneous frequency *47*

2.3.3 Wigner distribution *53*

2.3.4 Wavelet transforms *58*

2.3.5 Section summary *65*

CHAPTER 3: NSD **67**

3.1 INTRODUCTION 67

3.2 NONSTATIONARY SPECTRAL MODEL AND ASSUMPTIONS 67

3.2.1 Nonstationary spectral model *67*

3.2.2 Assumptions associated with NSD *69*

3.3 OPERATOR DESIGN AND APPLICATION 70

3.3.1 Overview *70*

3.3.2 Gain of input trace *72*

3.3.3 Calculation of |TVS| *75*

3.3.4 Smoothing *77*

3.3.5 Phase computation, inversion, and application of the operator *88*

3.4 FURTHER EXTENSIONS OF NSD 90

3.4.1 Introduction *90*

3.4.2 Profile-mode NSD *91*

3.4.3 Profile-mode NSD with random windows (fx-NSD) *92*

CHAPTER 4: PARAMETER TESTING **94**

4.1 INTRODUCTION 94

4.2 LENGTH OF TIME AND FREQUENCY SMOOTHERS 97

4.2.1 Frequency smoother lengths for simple-smoothing NSD *98*

4.2.2 Time smoother lengths for simple-smoothing NSD *103*

4.2.3 Frequency smoother lengths for residual-smoothing NSD *106*

4.2.4 Time smoother lengths for residual-smoothing NSD *109*

4.3 SMOOTHER GEOMETRY 112

4.3.1 Smoothing geometry in simple-smoothing NSD *114*

4.3.2 Residual-smoothing and smoother geometry *116*

4.4 SENSITIVITY OF NSD TO $\hat{Q}$ 119

4.5 WINDOW LENGTH IN THE |TVS| CALCULATION 124

4.6 WINDOW INCREMENT IN THE |TVS| CALCULATION 130

4.7 EXPONENTIAL GAIN FACTOR 133

4.8 COMPARISON OF NSD TO STATIONARY DECONVOLUTION 138

4.9 COMPARISON OF NSD TO BANDLIMITED REFLECTIVITY WITH CONSTANT PHASE ROTATIONS 143

4.10 COMPARISON OF HOW FINITE NUMERICAL PRECISION AFFECTS NSD 145

4.11 CHAPTER 4 SUMMARY 148

CHAPTER 5: EXAMPLES 152

5.1 INTRODUCTION 152

5.1.1 Processing the Blackfoot Broadband survey *153*

5.2 DETERMINATION OF PARAMETERS FOR THE BLACKFOOT BROADBAND SURVEY 157

5.2.1 Method of smoothing and operator phase *160*

5.2.2 Smoother lengths *162*

5.2.3 Phase of synthetic seismograms *164*

5.2.4 Variation of stab factor *165*

5.2.5 Conclusions from parameter testing *167*

5.3 COMPARISON OF NSD TO OTHER DECONVOLUTION TECHNIQUES 168

5.4 COMPARISON OF EXTENSIONS OF NSD 178

CHAPTER 6: CONCLUSIONS AND FUTURE WORK 184

6.1 CONCLUSIONS 184

6.2 FUTURE WORK 187

REFERENCES 189

LIST OF TABLES

TABLE 1.1: TYPICAL Q VALUES FOR P WAVES IN DIFFERENT ROCK TYPES 6

TABLE 4.1: DEFAULT PARAMETERS CHOSEN FOR NSD 149

LIST OF FIGURES

FIGURE 1.1: AN ILLUSTRATION OF THE CONVOLUTIONAL MODEL. 14

FIGURE 1.2: THE HILBERT OPERATOR.. 22

FIGURE 1.3: A DISPERSION CURVE FOR A CONSTANT Q PULSE. 26

FIGURE 1.4: THE MINIMUM-PHASE PULSES CORRESPONDING TO DIFFERENT SAMPLE RATES 27

FIGURE 1.5: A RANDOM TIME SERIES, WAVELET, AND TRACE (CREATED BY CONVOLVING THE RANDOM TIME SERIES AND WAVELET) AND THEIR SPECTRA. 29

FIGURE 2.1: CALCULATION OF A |TVS| FROM AN INPUT TRACE. 43

FIGURE 2.2: EXAMPLE OF HOW WINDOW LENGTH AFFECTS THE TIME AND FREQUENCY RESOLUTION OF THE |TVS|.. 46

FIGURE 2.3: COSINE SIGNAL CONTAINING NOISE OF A SHORT DURATION 54

FIGURE 2.4: A WIGNER DISTRIBUTION SHOWING NOISE.. 55

FIGURE 2.5: THE WAVELET OF SCALE, S, IS COMPARED TO THE SIGNAL AT VARIOUS TRANSLATIONS 62

FIGURE 2.6: A COMPARISON OF THE RESOLUTION OF THE |TVS| AND WAVELET TRANSFORM 65

FIGURE 3.1: THE WINDOW INCREMENT OF THE |TVS| CALCULATION DETERMINES THE TIME SAMPLE RATE OF THE |TVS|.. 74

FIGURE 3.2: A STEEP EXPONENTIAL DECAY CURVE IS SHOWN WITH ITS FOURIER SPECTRUM 75

FIGURE 3.3: THE |TVS| OF AN UNGAINED SYNTHETIC INPUT TRACE TO NSD, Q SURFACE (Q=50), STATIONARY SOURCE SPECTRUM AND BANDLIMITED REFLECTIVITY. 77

FIGURE 3.4: THE PROPAGATING WAVELET FROM THE SIMPLE-SMOOTHING METHOD. 81

FIGURE 3.5: THE RESIDUAL AMPLITUDE SPECTRUM AFTER SMOOTHING IN TIME AND FREQUENCY. 84

FIGURE 3.6: A COMPARISON OF THE AMPLITUDE SPECTRUM OF THE SOURCE WAVEFORM AND ITS ESTIMATION FROM THE RESIDUAL-SMOOTHING METHOD. 84

FIGURE 3.7: THE PROPAGATING WAVELET FROM THE RESIDUAL-SMOOTHING METHOD AND THE THEORETICAL PROPAGATING WAVELET 87

FIGURE 4.1: THE AUTOCORRELATION OF THE INPUT TRACE. 100

FIGURE 4.2: TEST OF THE SENSITIVITY OF MINIMUM-PHASE SIMPLE-SMOOTHING VERSION OF NSD TO FREQUENCY SMOOTHER LENGTH.. 101
FIGURE 4.3: |TVS| OF TRACES IN FIGURE 4.2.. 102
FIGURE 4.4: TEST OF THE SENSITIVITY OF MINIMUM-PHASE SIMPLE-SMOOTHING VERSION OF NSD TO THE TIME SMOOTHER LENGTH.. 104
FIGURE 4.5: |TVS| OF TRACES IN FIGURE 4.4. 105
FIGURE 4.6: TEST OF THE SENSITIVITY OF MINIMUM-PHASE RESIDUAL-SMOOTHING VERSION OF NSD TO FREQUENCY SMOOTHER LENGTH. 107
FIGURE 4.7: |TVS| OF TRACES IN FIGURE 4.6. 108
FIGURE 4.8: TEST OF THE SENSITIVITY OF MINIMUM-PHASE RESIDUAL-SMOOTHING VERSION OF NSD TO THE TIME SMOOTHER LENGTH. 110
FIGURE 4.9: |TVS| OF TRACES IN FIGURE 4.8.. 111
FIGURE 4.10: THE BOXCAR AND THE HANNING SMOOTHER AND THEIR FOURIER SPECTRA 114
FIGURE 4.11: COMPARISON OF MINIMUM-PHASE SIMPLE-SMOOTHING RESULTS CREATED WITH DIFFERENT SMOOTHER GEOMETRIES (HANNING SMOOTHER OR BOXCAR SMOOTHER) IN THE SIMPLE-SMOOTHING METHOD 115
FIGURE 4.12: THE |TVS| OF THE TRACES IN FIGURE 4.11. 116
FIGURE 4.13: COMPARISON OF MINIMUM-PHASE RESIDUAL-SMOOTHING RESULTS CREATED WITH DIFFERENT SMOOTHER GEOMETRY (HANNING SMOOTHER OR BOXCAR SMOOTHER) IN THE RESIDUAL-SMOOTHING METHOD 118
FIGURE 4.14: THE |TVS| OF THE TRACES IN FIGURE 4.13. 119
FIGURE 4.15: SENSITIVITY OF THE DECAY EXPONENT TO ESTIMATES OF Q. 121
FIGURE 4.16: TEST OF THE SENSITIVITY OF NSD TO ERRORS IN THE ESTIMATE OF Q, $\hat{Q}$ 123
FIGURE 4.17: THE |TVS| OF THE OUTPUT TRACES FROM FIGURE 4.16. 124
FIGURE 4.18: COMPARISON OF THE |TVS| OF THE GAINED INPUT TRACE FOR VARYING WINDOW LENGTHS. 127
FIGURE 4.19: OUTPUT TRACES FROM NSD THAT HAVE WHERE THE |TVS| OF THE UNGAINED INPUT TRACE HAS BEEN CALCULATED WITH DIFFERENT VALUES FOR THE WINDOW LENGTH. 128
FIGURE 4.20: THE |TVS| OF THE TRACES FROM FIGURE 4.19. 129

FIGURE 4.21: THE |TVS| OF THE INPUT TRACE CREATED WITH VARYING WINDOW INCREMENTS. 131

FIGURE 4.22: TEST OF THE SENSITIVITY OF MINIMUM-PHASE RESIDUAL-SMOOTHING NSD TO THE WINDOW INCREMENT OF THE |TVS| CALCULATION IN THE OPERATOR DESIGN STAGE. 132

FIGURE 4.23: THE |TVS| OF THE TRACES IN FIGURE 4.22. 133

FIGURE 4.24: INPUT TRACE GAINED WITH DIFFERENT VALUES OF THE EXPONENTIAL GAIN CONSTANT. 135

FIGURE 4.25: TEST OF SENSITIVITY OF MINIMUM-PHASE RESIDUAL-SMOOTHING NSD TO THE EXPONENTIAL GAIN OF THE INPUT TRACE. 136

FIGURE 4.26: THE |TVS| OF FIGURE 4.25. 137

FIGURE 4.27: A COMPARISON OF OUTPUT TRACES FROM VARIOUS DECONVOLUTION ALGORITHMS. 141

FIGURE 4.28: A COMPARISON OF THE |TVS| OF VARIOUS DECONVOLUTION TECHNIQUES, INPUT TRACE AND BANDLIMITED REFLECTIVITY. 142

FIGURE 4.29: COMPARISON OF MINIMUM-PHASE RESIDUAL-SMOOTHING NSD TO BANDLIMITED REFLECTIVITY THAT HAS BEEN PHASE ROTATED FROM -135 TO 180 ° 144

FIGURE 4.30: COMPARISON OF TRACES CREATED WITH DIFFERENT VALUES OF Q AND DECONVOLVED WITH MINIMUM-PHASE RESIDUAL SMOOTHING NSD. 147

FIGURE 4.31: |TVS| OF TRACE IN FIGURE 4.30. 148

FIGURE 5.1: A MAP SHOWING THE LOCATION OF WELLS 14-09 AND 4-16 IN RELATION TO THE BLACKFOOT BROADBAND SURVEY 157

FIGURE 5.2: A COMPARISON OF THE 4-16 SYNTHETIC SEISMOGRAM TO RESULTS FROM MINIMUM-PHASE RESIDUAL-SMOOTHING NSD, MINIMUM-PHASE SIMPLE-SMOOTHING NSD, ZERO-PHASE RESIDUAL-SMOOTHING NSD AND ZERO-PHASE SIMPLE-SMOOTHING NSD. 161

FIGURE 5.3: THE TIME SMOOTHER OF THE MINIMUM-PHASE RESIDUAL-SMOOTHING METHOD WAS VARIED FROM 0.05S TO 1.5S AND COMPARED TO THE SYNTHETIC SEISMOGRAM FROM THE 4-16 WELL 163

FIGURE 5.4: THE FREQUENCY SMOOTHER IN THE MINIMUM-PHASE RESIDUAL-SMOOTHING METHOD WAS VARIED FROM 5 HZ TO 30 HZ AND COMPARED TO THE SYNTHETIC SEISMOGRAM FROM THE 4-16 WELL. 164

FIGURE 5.5: THE SYNTHETIC SEISMOGRAM IS ROTATED THROUGH CONSTANT PHASE ROTATIONS FROM 0 TO 180° WITH 45° INCREMENTS. 165

FIGURE 5.6: THE STAB FACTOR WAS VARIED FROM 10^{-1} TO 10^{-5} IN THE MINIMUM-PHASE RESIDUAL-SMOOTHING RESULT. 167

FIGURE 5.7: THE BLACKFOOT BROADBAND SURVEY AFTER PRE-STACK PROCESSING AND WITHOUT APPLICATION OF ANY DECONVOLUTION. 171

FIGURE 5.8: THE BLACKFOOT BROADBAND SURVEY WITH GAIN AND POST-STACK WIENER DECONVOLUTION AND THE COMPLETE POST-STACK PROCESSING DESCRIBED IN SECTION 5.4. 172

FIGURE 5.9: THE BLACKFOOT BROADBAND SURVEY WITH POST-STACK WIENER DECONVOLUTION AND POST-STACK INVERSE-Q FILTERING AND THE COMPLETE POST-STACK FLOW DESCRIBED IN SECTION 5.4... 173

FIGURE 5.10: THE BLACKFOOT BROADBAND SURVEY WITH POST-STACK PROFILE-MODE NSD AND THE COMPLETE POST-STACK PROCESSING AS DESCRIBED IN SECTION 5.4. 174

FIGURE 5.11: THE AVERAGE |TVS|, CALCULATED BY AVERAGING THE |TVS| OF TRACES 50 TO 100, OF THE STACKED SECTIONS FROM FIGURES 5.8 TO 5.10. 175

FIGURE 5.12: THE TARGET AREA OF EACH OF THE DECONVOLVED SECTIONS 176

FIGURE 5.13: THE 14-09 SYNTHETIC SEISMOGRAM COMPARED TO THE RESULT FROM GAIN AND POST-STACK WIENER DECONVOLUTION, POST-STACK WIENER DECONVOLUTION AND POST-STACK INVERSE-Q FILTERING AND POST-STACK PROFILE-MODE NSD. 177

FIGURE 5.14: THE 4-16 SYNTHETIC SEISMOGRAM COMPARED TO THE RESULT FROM GAIN AND POST-STACK WIENER DECONVOLUTION, POST-STACK WIENER DECONVOLUTION AND POST-STACK INVERSE-Q FILTERING AND POST-STACK PROFILE-MODE NSD.. 178

FIGURE 5.15: AVERAGE |TVS| OF TRACE-BY-TRACE NSD, PROFILE MODE NSD AND FX-NSD 180

FIGURE 5.16: A COMPARISON OF PROFILE-MODE NSD, TRACE-BY-TRACE NSD AND FX-NSD IN THE CHANNEL ZONE.. 181

FIGURE 5.17: THE 14-09 SYNTHETIC COMPARED TO TRACE-BY-TRACE NSD, PROFILE-MODE NSD AND FX-NSD.. 182

FIGURE 5.18: THE 4-16 SYNTHETIC COMPARED TO TRACE-BY-TRACE NSD, PROFILE-MODE NSD AND FX-NSD. 183

STRUCTURE OF THESIS

This thesis begins with a review of the fundamental concepts required to understand why a technique such as nonstationary deconvolution is needed and how it works. The concepts of attenuation, quality factor Q, nonstationarity, and digital minimum phase are reviewed. Two methods similar to nonstationary deconvolution, stationary deconvolution and inverse-Q filtering, are also introduced at this stage and their strengths and weaknesses are described. Next, two specific techniques that are employed in the NSD algorithm are described: nonstationary filtering and time-variant spectra. There are several alternatives to time-variant spectra, such as instantaneous frequency, the Wigner distribution and the wavelet transform, and these are discussed.

After this background has been provided nonstationary deconvolution can be introduced. The first stage in the development of nonstationary deconvolution is to present a nonstationary spectral model. From this spectral model the algorithm of NSD is developed and explained. The NSD algorithm has two extensions that have been designed to increase efficiency and improve the final result. These different extensions of NSD are described. Next, NSD is illustrated on synthetic examples and some of the parameters used in the algorithm are tested. Then NSD is tested on real data examples and compared to synthetic seismograms created from well log data. Lastly, conclusions are drawn and future work described.

CHAPTER 1: INTRODUCTION

1.1 Overview of the introduction

The purpose of this introduction is to provide a review of fundamental concepts associated with nonstationary deconvolution, also called NSD. The concepts of anelastic attenuation, Q, dispersion, additional forms of attenuation, nonstationarity, stationary convolutional model, multiples, spectral ratio method of Q estimation, surface consistent model, minimum-phase, digital minimum-phase estimation, stationary deconvolution and inverse-Q filtering will be presented and described in this chapter.

1.2 Anelastic attenuation

In this section, anelastic attenuation will be defined and a description of a wave travelling in an anelastic medium will be given. Two parameters, Q and α, describing anelastic attenuation will be defined and the relationship between them will be derived. In addition, there will be a discussion on how Q varies with frequency and how time and frequency losses are related. Finally, a discussion on minimum-phase dispersion is presented.

As a wave propagates through an anelastic medium, some of its energy becomes converted to heat by the internal friction of the medium and is irreversibly lost. This process of energy loss is called absorption and it is an intrinsic property of the medium in which the wave is travelling. Absorption, also called intrinsic attenuation or internal

friction, refers to a variety of physical processes. Two examples of these processes are shear heating at grain boundaries or movements along mineral dislocations (Waters, 1992). Absorption is commonly described by the coefficient of attenuation, α, or the quality factor, Q.

A plane wave propagating through a 1-D homogenous medium can be described as

$$A(x,t) = A_0 e^{2\pi i(kx-ft)}, \tag{1.1}$$

where k is wavenumber and f is frequency. Attenuation can be introduced into this model by allowing the frequency or wavenumber to be complex. Allowing the wavenumber to be complex results in

$$A(x,t) = A_0 e^{-\alpha x} e^{2\pi i(k_R x-ft)}, \tag{1.2}$$

where α is the attenuation coefficient and k_R is the real part of the complex wavenumber. The units of the attenuation are the same as that of the wavenumber, m^{-1}, when the wavenumber is allowed to be complex.

Alternately, attenuation can be described by the dimensionless value, Q. There are several different equations used to describe Q (see Johnston and Toksov, 1981, for a description) however the most common is that Q is the ratio of the peak stored energy in a cycle to the dissipated energy per cycle

$$Q = \frac{2\pi E}{-\Delta E}, \tag{1.3}$$

where E is the peak stored elastic energy and $-\Delta E$ is the energy loss per cycle of the wave.

The following derivation shows how Q is related to the attenuation coefficient. A point, P, has position (x_1, t_1) on a travelling wave,

$$P(x_1, t_1) = A_o e^{-\alpha x_1} e^{2\pi i(k_R x_1 - f t_1)}. \tag{1.4}$$

A point, $P(x_2, t_2)$, occurs at the same phase, one cycle later than $P(x_1,t_1)$. The period of the wave is given by T and $x_2=x_1+vT$ and $t_2=t_1+T$, where v is the phase velocity. The point $P(x_2, t_2)$ can be written as

$$P(x_2, t_2) = A_o e^{-\alpha(x_1+vT)} e^{2\pi i(k_R(x_1+vT)-f(t_1+T))}. \tag{1.5}$$

Since the phases of $P(x_1, t_1)$ and $P(x_2, t_2)$ are equal

$$k_R x_1 - ft = k_R(x_1 + vT) - f(t_1 + T). \tag{1.6}$$

Simplifying Equation (1.6) leads to

$$k_R vT - fT = 0, \tag{1.7}$$

so that

$$v = \frac{f}{k_R}. \tag{1.8}$$

$P(x_2, t_2)$ can be expressed in terms of $P(x_1, t_1)$:

$$P(x_2, t_2) = P(x_1, t_1)e^{-\alpha v T}, \tag{1.9}$$

Energy is proportional to the square of the physical amplitude of the wave:

$$E(x_1, t_1) \propto P(x_1, t_1)^2. \tag{1.10}$$

$$E(x_2, t_2) \propto P(x_2, t_2)^2. \tag{1.11}$$

Substituting Equations (1.10) and (1.11) into Equation (1.3) yields

$$Q = \frac{2\pi E(x_1, t_1)}{E(x_1, t_1) - E(x_2, t_2)} = \frac{2\pi P(x_1, t_1)^2}{P(x_1, t_1)^2 - P(x_1, t_1)^2 e^{-2\alpha v T}} = \frac{2\pi}{1 - e^{-2\alpha v T}}. \tag{1.12}$$

The exponential in Equation (1.12) can be expanded with a Taylor series $(e^x = 1 + x + \frac{x^2}{2!} + ...)$ approximation to give

$$Q \approx \frac{\pi}{\alpha v T}. \tag{1.13}$$

Replacing period, T, with inverse of frequency in Equation (1.13) and rearranging gives an approximate relationship between the coefficient of attenuation and Q:

$$\alpha \approx \frac{\pi f}{vQ}. \qquad (1.14)$$

It is uncertain how Q varies with frequency and this relationship cannot be determined from Equation (1.14) because the attenuation coefficient may also be dependent on frequency. Ricker (1977) postulates that Q is proportional to the inverse of frequency. The constant Q theory (Kjartansson, 1979) postulates that Q is independent of frequency. Futterman (1962) proposes that Q is constant over the range of seismic frequencies. This theory is often called the nearly constant Q theory because of the limited frequency range. Knopoff (1964) concluded that Q is approximately independent of frequency for homogenous solids. For the purposes of this work, a frequency independent Q model has been chosen. This seems reasonable if NSD is applied to data from solid media within the band of seismic frequencies.

The essence of constant Q theory is that anelastic losses are time and frequency dependent and therefore spectral attenuation and amplitude (time-domain) decay are two manifestations of the same problem. The joint time-frequency dependence of the attenuation is obvious when Equation (1.14) is substituted into Equation (1.2). The exponential describing attenuation in Equation (1.2) becomes $\exp(-\pi f v^{-1} Q^{-1} x)$. It can be seen from this exponential that attenuation depends on frequency, f, and traveltime (x/v). This joint dependence means that absorption causes a seismic pulse to broaden and decrease in amplitude in the time domain while losing spectral bandwidth in the

frequency domain. Some typical values of Q for P waves (intrinsic attenuation), taken from Waters (1992) are shown in Table 1.1.

Table 1.1: Typical Q values for P waves in different rock types

rock type	Q
basalt	561
diorite	179
granite	311
marble	547
quartzite	392
slate	219
dolomite	192
limestone	203
chalk	136
oolitic limestone	46
shelly limestone	68
Solenhofen sandstone	679
Amherst sandstone	24
Berea sandstone	130
Homewood sandstone	69
Old red sandstone	93
Pierre shale	17
Sylvan shale	72

Absorption is necessarily accompanied by minimum-phase dispersion in a linear, causal medium (Futterman, 1962). For a definition of minimum phase see Section 1.8.1. Dispersion is the property that different frequency components travel at different velocities, called phase velocities. This means that Equation (1.1) is actually incomplete. An additional term, $\phi(f)$, representing phase associated with absorption must be added to the phase of the wave to have a linear, causal physical theory. Solving Equation (1.8) for

wavenumber, substituting it into Equation (1.2), rearranging and adding a phase term, $\phi(f)$, associated with minimum-phase absorption gives the following equation

$$A(x,t) = A_o e^{-\alpha x} e^{-i2\pi f\left(t-\frac{x}{v}+\phi(f)\right)}, \tag{1.15}$$

where $\phi(f)$ is given by (Kjartansson, 1979)

$$\phi(f) = \frac{t}{\pi Q}\ln\left|\frac{f}{f_o}\right|. \tag{1.16}$$

Phase velocity can be inferred from the phase of the wave by equating a wave's phase to zero and solving for velocity (x/t)

$$t+\frac{x}{v}+\phi(f) = 0. \tag{1.17}$$

Substitute $\phi(f)$ from Equation (1.16) into Equation (1.17)

$$t-\frac{x}{v}+\frac{t}{\pi Q}\ln\left|\frac{f}{f_o}\right| = 0\ . \tag{1.18}$$

This yields the dispersion relation (Aki and Richards, 1980)

$$\frac{x}{t} = v(f) = v(f_o)\left(1+\frac{1}{\pi Q}\ln\left|\frac{f}{f_o}\right|\right). \tag{1.19}$$

where f_o is an arbitrary reference frequency and $v(f_o)$ is the phase velocity associated with the reference frequency.

1.3 Additional attenuative mechanisms

In practice it can be difficult to isolate the effects of anelastic attenuation from the effects of other attenuative mechanisms. Geometrical spreading (spherical divergence), transmission loss, mode conversions, intrabed multiples, refractions, and scattering of acoustic energy all contribute to the degradation of seismic reflections. Each of these attenuative mechanisms will be briefly explained and it will be stated if the mechanism is dependent on time or frequency or both. A relationship will be given between the Q of intrinsic attenuation and other time and frequency-dependent attenuative mechanisms.

Amplitude decay due to geometrical spreading results from the conservation of energy. In a homogenous medium the total amount of energy in an expanding spherical wavefront at any given time must be constant. Since the wavefront is growing continually and is spread over the surface area of $4\pi R^2$, the energy per unit area (a function of the square of the amplitude) must decrease and the wave amplitude decays as 1/R, where R is the radius of curvature of the wavefront (Sheriff and Geldart, 1995). Losses due to spherical divergence are dependent on traveltime and not on frequency.

Another attenuative mechanism, transmission loss, occurs because some of the energy from a downward-travelling wave is transmitted at a layer interface. Thus energy available to illuminate deeper targets decreases with each interface transmission. These losses can be large (Schoenberger and Levin, 1974). Transmission losses are dependent on time and not frequency.

Mode conversions cause attenuation. Seismic energy is continually being converted between P and S waves at impedance contrasts. For example, an incident P wave will be reflected at an interface as a P and S wave and transmitted as a P and S wave. If an S or P wave arrives at a geophone that records only the vertical component of ground motion, it will generally not be recorded fully (unless the P-wave is travelling vertically). Some of the information about the wave will be lost. In addition, S waves are more attenuated than P waves because anelastic attenuation results partly from shear movement along grain boundaries (Lay and Wallace, 1995). Therefore an S wave will have a lower frequency content than a P wave arriving at the same time. If the S wave energy leaks onto a P wave dataset, the low frequency content of the S wave will contribute to the low frequencies of the dataset. Attenuation due to mode conversions can be classified as time dependent attenuation, although the topic is well outside the scope of this thesis.

Intrabed multiples are a persistent form of attenuation. Multiples are events that have undergone more than one reflection (Sheriff and Geldart, 1995). Multiples often interfere destructively with primary energy and cause signal degradation through incoherent superposition of seismic events. Losses due to intrabed multiples are time and frequency dependent for two reasons. Since Q generally increases with depth, multiples are expected to experience more attenuation than primary reflections possessing the same traveltime (Trorey, 1962). Therefore if intrabed multiples interfere with primary reflections they boost the low frequencies of the primary reflections (Schoenberger and

Levin, 1974). In addition, ghosts are shallow multiples in the near surface. They follow the source waveform closely and have a reversed polarity. The frequency spectrum of a ghost multiple contains periodic notches (Hatton, Worthington, and Makin, 1986). In a superposition of many ghost multiples the notches degrade the spectrum of the primary reflectors.

Seismic waves reflected at 90 degrees from the normal to the interface are called refracted waves (Sheriff and Geldart, 1995). Refracted waves travel along an interface. Energy is not transmitted and therefore not available to provide deeper information about the subsurface. Losses due to refraction are dependent on the incident angle of the wave and the impedance of the medium on either side of the interface and not on time or frequency.

Scattering is another type of seismic attenuation. Seismic waves are scattered by small-scale heterogeneities into a sequence of arrivals that distorts the primary wavefield (Lay and Wallace, 1995). Scattering is frequency dependent and high frequencies are selectively attenuated through incoherent superposition.

Some of the aforementioned attenuative mechanisms can be collectively referred to as stratigraphic filtering (Schoenberger and Levin, 1974). Stratigraphic filtering is attenuation due to stratigraphic layering and includes transmission losses, intrabed multiples and mode conversions.

Interference effects such as intrabed multiples, scattering and mode conversions are dependent on both time and frequency as explained above. Although the physical mechanism of interference differs strongly from anelastic attenuation, their effects on seismic data can be difficult to distinguish. A measurement of Q cannot separate the effects of interference attenuation from the effects of absorption, and therefore the measurement of Q is often called the effective Q. The effective Q, Q_{eff}, is composed of both the anelastic absorption Q, Q_i, and the apparent attenuation Q, Q_{app}, (Tonn, 1991)

$$\frac{1}{Q_{eff}} = \frac{1}{Q_{app}} + \frac{1}{Q_i}. \qquad (1.20)$$

The intrinsic attenuation, Q_i, is minimum-phase as discussed in Section 1.2, however the apparent attenuation, $Q_{app,}$ is constrained in the same manner.

1.4 Nonstationarity

In this section, the terms nonstationary and nonstationary convolutional processes are defined. "Nonstationary" is a general term used to describe a property that is variant with time. In contrast, stationary refers to a property that is time invariant. In practical applications, the term nonstationary is meaningful only when used in reference to a time scale. For example a time series of reflection coefficients fluctuates randomly corresponding to geology. On a small scale, these fluctuations of the reflection coefficients could be described as nonstationary, however reflectivity may be described as stationary because the large scale averages do not systematically change. The term

nonstationary can be used to describe a property that is time-variant and in the context of this thesis, the two words are interchangeable.

Attenuation based on constant Q model is a nonstationary convolutional process (Margrave, 1998). Nonstationary convolutional processes are filtering processes that depend on both time and frequency. A constant Q filter superimposed with a source waveform can be applied through nonstationary convolution to a series of reflectivity coefficients. Nonstationary convolution is described more thoroughly in Chapter 2.

1.5 The stationary convolutional model and source signature

The convolutional model is a widely accepted model upon which many deconvolution algorithms are based. First, the stationary convolutional model is described in both the time and frequency domain. Then the goal of a deconvolution process is briefly discussed in the context of the stationary convolutional model. Next, the inadequacy of convolutional model in modeling nonstationary effects, such as nonstationary multiples is mentioned, with a discussion of how nonstationary multiples could arise.

The convolutional model, in its simplest terms, states that a seismic trace is a convolution of the source waveform and its multiple train with the earth's reflectivity. Each layer boundary is superimposed with a scaled version of the source waveform and its associated multiples. A 1-D seismic trace, s(t), is modeled as (Sheriff and Geldart, 1995)

$$s(t) = r(t) * m(t) * w(t), \tag{1.21}$$

where r(t) is the reflectivity of the earth, m(t) is multiples, w(t) is the embedded wavelet and * denotes convolution. The reflectivity is a function of depth in the earth; however it can be converted to time if the velocity of the wave is known, such as through a sonic log. In the frequency domain, convolution becomes multiplication (the convolution theorem (Karl, 1989)) and Equation (1.21) becomes

$$S(f)=R(f)M(f)W(f), \tag{1.22}$$

where R(f) is the spectrum of the earth's reflectivity, M(f) is the spectrum of the multiple content of the seismic trace and W(f) is the spectrum of the source signature. Figure 1.1 is a diagram showing how an impulse response is created by convolution of a reflectivity series with an impulse and its multiple train. In this example there is only one multiple, of reversed polarity, after the primary reflection. The impulse response is the response of a system when the input is a unit impulse (Sheriff and Geldart, 1995).

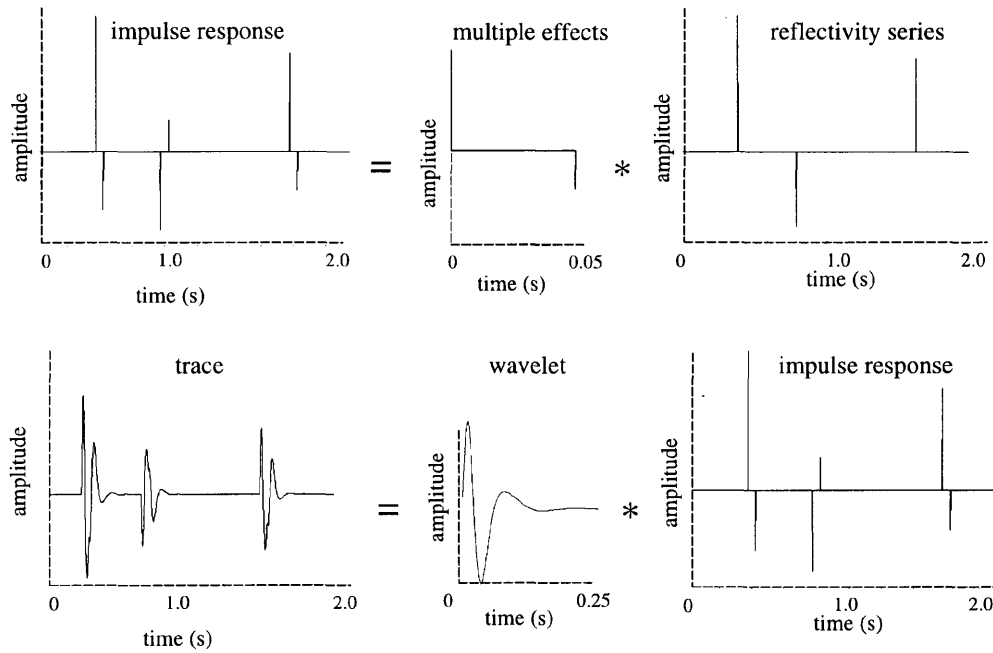

Figure 1.1: An illustration of the convolutional model. The impulse response (upper left) is a result of the convolution of the earth's reflectivity series with multiple effects. This impulse response is then convolved with a wavelet to produce a seismic trace.

From Equation (1.21) and Figure 1.1 it can be seen that the source signature (wavelet) obscures the reflection coefficients. It is desirable to collapse the source waveform and multiples so the layer boundaries can be seen more clearly and an estimate of the reflectivity can be recovered. Removal of the source signature increases the vertical resolution of the seismic data. This procedure is called deconvolution.

The convolutional model is inadequate to describe nonstationary effects in seismic data. This can be seen as Equations (1.21) and (1.22) are dependent on only time or frequency, and not both. One nonstationary effect often contained in seismic data is nonstationary multiples. Schoenberger and Houston (1998) define a multiple as stationary if all primaries generate multiples with fixed delay. A multiple associated with a deep primary reflector at moderate offsets will be nearly vertical and so will its primary. Multiples at large offsets and shallow reflectors have a travelpath more vertical than the travel path of the primary. Its separation time from the shallow primary will be less than the separation time of the deep primary reflector and it's multiple. If a multiple occurs above the zone of deconvolution operator design the convolutional model can still be used to model the seismic trace by modifying the input wavelet to include the multiple effects (Waters, 1992). However, if the multiples occur in the middle of the zone of operator design, the convolutional model is no longer applicable because the effective wavelet changes with time.

1.6 Spectral ratio method of Q estimation

NSD and inverse-Q filters both require an estimate of Q. The spectral ratio method is the most common method of Q estimation. In this method, Q is estimated from the ratio of the power spectra of a wave at two different times (White, 1992). This method is unable to distinguish apparent attenuation from intrinsic attenuation, as discussed in Section 1.3. First the spectral ratio method is described, followed by a description of how reliable estimates of Q based on this method can be.

The amplitude spectrum of a pulse experiencing Q attenuation is given by

$$|A(t,f)| = |A_o(f)|\, e^{-\pi f t/Q}, \tag{1.23}$$

where t is the traveltime of the pulse, $A_o(f)$ is the amplitude spectrum of the source signature of the pulse and $|A(t,f)|$ is the attenuated amplitude spectrum of the pulse at some time t. Using the convolutional model and ignoring multiple effects, the power spectrum of the seismic data, $|S(t,f)|^2$, is related to the power spectrum of the reflectivity, $|R(t,f)|^2$ by

$$|S(t,f)|^2 = |A(t,f)|^2 |R(t,f)|^2. \tag{1.24}$$

Equation (1.23) at some time, t_2, is divided by the same equation at an earlier time, t_1.

$$\frac{|A(t_2,f)|}{|A(t_1,f)|} = e^{-\pi f (t_2 - t_1)/Q} \tag{1.25}$$

Equation (1.24) at some time, t_2, is also divided by the same equation at an earlier time, t_1, and then the natural logarithm is taken. It is assumed that the spectral coloring of the reflectivity does not change or has been compensated for (White, 1992).

$$\ln\left[\frac{|S(t_2,f)|^2}{|S(t_1,f)|^2}\right] = 2\ln\left[\frac{A(t_2,f)}{A(t_1,f)}\right]. \tag{1.26}$$

Substituting Equation (1.25) into Equation (1.26) to obtain

$$\ln\left[\frac{|S(t_2,f)|^2}{|S(t_1,f)|^2}\right] = -2\pi f(t_2 - t_1)/Q \qquad (1.27)$$

Equation (1.27) is the equation of a straight line. Q is calculated from the slope of the least squares regression against frequency of the spectral ratio.

The spectral ratio method of estimating Q is well known and regarded as being optimal if true amplitudes are not available (Tonn, 1991). The estimates of Q determined from the spectral ratio method are regarded as reliable provided the data is noise-free, however these estimates may not be satisfactory in the presence of noise (Tonn, 1991). The estimates are improved if the time separation between samples is large, if a large bandwidth is used and if the value of Q is small (White, 1992). White (1992) suggests that it is unreasonable to expect a reliable estimate of Q over depth intervals as short as most reservoir intervals.

1.7 Surface consistent model

Often the earth's effects in a seismogram can be broken down into two categories: near surface effects and subsurface effects. First, near surface effects and subsurface effects are described. This is followed by a discussion of how Q attenuation is classified in this model.

The distinction between near surface and subsurface is not always clear, and is usually described as the base of the weathering layer. The near surface effects are those effects which depend only on source and receiver position. This includes source

signature, static corrections, surface waves, source ghosts, receiver arrays, etc. Subsurface effects depend on midpoint and offset and include Q attenuation, reflectivity, residual moveout, spherical divergence and most classes of multiples.

Q effects are usually considered midpoint consistent and not as near surface effects, even though the near surface is highly attenuative. This distinction occurs for two main reasons. The first reason is related to the relatively shallow depth of the near surface layer as compared to the depth of the target area. The near surface is not very thick, perhaps on the order of 10's of meters. Therefore, the near surface is only represented by a few samples on a seismic trace. It is difficult to measure and correct for attenuation based on these small numbers of samples.

The second reason Q effects are not considered for the near surface is because near surface absorption can be considered stationary. Near surface absorption changes the shape of the wavelet before the zone of interest, and so near surface Q effects can be considered effectively as part of the source signature.

The surface consistent approach can be very powerful. It is used in amplitude analysis, deconvolution and residual statics estimation. In addition it takes advantage of the redundancy of seismic data in common midpoint, source, and receiver gathers to reduce noise (Levin, 1989).

1.8 Minimum phase

Like many other deconvolution methods, it is assumed in NSD that the wavelet embedded in the seismogram is minimum phase. The minimum-phase wavelet is generated through physical means (Futterman, 1962) and during processing a digital operator is designed to remove it. This assumption of minimum phase and subsequent digital estimation of the phase limits the procedure, and the phase cannot be perfectly removed from the input data. This section begins with a definition of minimum phase and the minimum-phase assumption. Next, digital minimum phase estimation as computed from the Hilbert transform is described. Finally the problems associated with estimating a minimum-phase spectrum using a digital Hilbert transform are discussed.

1.8.1 Definition of minimum phase

A minimum-phase wavelet can be defined as a stable and causal wavelet with a stable, causal inverse (Eisner, 1984). In the time domain a minimum-phase pulse has energy arriving earlier than all other causal pulses, giving it a front-loaded appearance. This property of a minimum-phase pulse having the least energy delay is referred to as Robinson's energy delay theorem (Robinson, 1966). As a corollary, the minimum-phase spectrum can be uniquely determined for a given amplitude spectrum (Eisner, 1984).

1.8.2 The minimum-phase assumption

It is commonly assumed that the source signature and earth filter (earth effects, such as absorption and nonstationary multiples, can be regarded as a filter which acts on

seismic waves) are minimum phase. If these assumptions hold, then the convolutional model suggests that the wavelet recorded at the receivers is also minimum phase because convolution of minimum-phase components results in a minimum-phase output.

However, seismic data is digitized before recording and this presents complications in the minimum-phase assumption and estimation as explained more fully in Section 1.8.4. The sample rate chosen for digitization is very important because it determines the upper frequency limit of the digitized signal. The highest frequency that the digitized signal can properly describe is called the Nyquist frequency, f_{Nyq}, and it is related to the sample interval by

$$f_{Nyq} = \frac{1}{2\Delta t}, \tag{1.28}$$

where Δt is the time sample interval. If the data is sampled too coarsely, high frequencies are folded back onto the spectrum and are manifested as lower frequencies. This phenomenon is called aliasing (Karl, 1989). By definition, a minimum-phase signal must have an inverse, therefore it must be nonzero at all frequencies. This condition ensures that a digitized minimum-phase signal will always contain frequencies above the Nyquist frequency and aliasing will occur. Conversely, a bandlimited signal can never be minimum-phase.

The assumption that the wavelet in the recorded seismic section is minimum phase is controversial. Ziolkowski (1991) argues that most sources do not produce a

minimum-phase source wavelet, although he concedes that a dynamite source on land may produce such a wavelet. He argues that because the source waveform is not necessarily minimum-phase then creating a minimum-phase spectrum from the amplitude spectrum of a wavelet with a method such as the Hilbert transform (described in Section 1.8.3) is purely a mathematical convenience. Others dispute this opinion. Hargreaves (1992) states that an air-gun array signature is minimum-phase and its phase spectrum can be derived from the Hilbert transform and Robinson (1966) says that minimum-delay pulse trains can be expected in a layered earth.

1.8.3 Estimation of minimum-phase spectrum

The minimum-phase spectrum of a signal can be estimated with a Hilbert transform, H. The minimum-phase spectrum, $\phi(f)$, corresponding to a specific amplitude spectrum, A(f), is determined by (Karl, 1989)

$$\phi(f)=H[\ln(A(f))], \tag{1.29}$$

or more explicitly:

$$\phi(f) = \frac{1}{\pi}\int_{-\infty}^{\infty}\frac{\ln(A(f'))}{(f-f')}df'. \tag{1.30}$$

Equation (1.30) is equivalent to a convolution (represented by *) of the natural logarithm of the amplitude spectrum with the Hilbert kernel, $(\pi f)^{-1}$, shown in Figure 1.2

$$\phi(f) = \ln(A(f)) * \frac{1}{\pi f}. \qquad (1.31)$$

It can be seen from Equations (1.30) and (1.31) that the low values of the amplitude spectrum are very significant in the Hilbert integral (the logarithm goes to negative infinity as A(f) goes to zero). This means that the low amplitude frequencies, where noise is likely to dominate, are very important and will cause large phase problems.

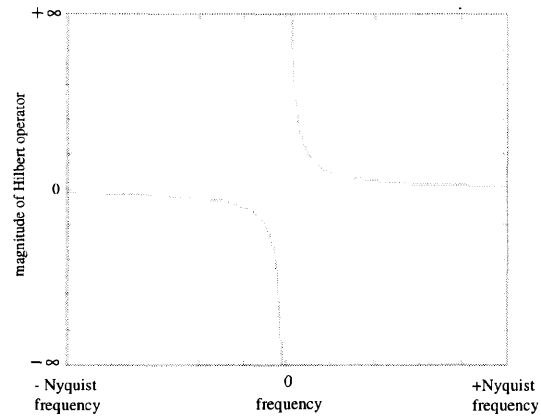

Figure 1.2: The Hilbert operator. The Hilbert operator, $(\pi f)^{-1}$, has a discontinuity at 0 Hz and a very steep gradient near 0 Hz.

1.8.4 Problems associated with digital minimum-phase estimation

There are several problems associated with estimating a minimum-phase spectrum from an amplitude spectrum using a digital Hilbert transform. These problems will be briefly listed in this paragraph and then discussed in more detail in this section. The first problem is that the integration to infinite limits in the analogue version

(Equation (1.29)) is replaced with summation to finite limits in the digital version. In addition, the amplitude spectrum of the trace and the Hilbert operator are sampled. Another complicating factor is that seismic trace may be windowed before estimating the amplitude spectrum. In addition, multiplying the amplitude spectrum by a constant will cause a phase rotation. The digital phase operator can only be an approximation of the analogue phase operator because of these factors. These problems with digital minimum-phase estimation are explained in this section and then an example of how sampling affects the estimated phase of a time-domain pulse is shown.

One of the main problems with the digital Hilbert transform is the replacement of the integration of the analogue equation with summation in the digital version. The infinite limits of integration are changed to the Nyquist interval in the digital procedure and the contribution of frequencies beyond the Nyquist interval is lost. In addition, the digital procedure is awkward because of the discontinuity of the Hilbert operator at zero.

In order to get a reasonable digital phase estimate with the Hilbert transform method, the digital amplitude spectrum must strongly resemble the analogue amplitude spectrum between 0 Hz and Nyquist frequency (f_N). This requires sufficient sampling of the amplitude spectrum in the frequency domain and dominance of reflected signal over noise. From digital processing theory, the frequency sample interval is inversely related to the length of the trace the spectrum is calculated from (Karl, 1989). Outside the bounds of 0 Hz to positive f_N, the digital amplitude spectrum will be a periodic function that folds back on itself at integer multiples of f_N, unlike the analogue amplitude spectrum.

The Hilbert transform must also be sufficiently sampled in the frequency domain. The Hilbert transform can be calculated by convolving the Hilbert operator ($(\pi f)^{-1}$) with the function, ln(A(f)), (Karl, 1989), as seen in Equation (1.31). The Hilbert operator has steep gradients close to the frequency origin that are hard to represent with sampled data (Kets, 1987) as shown in Figure 1.2. Therefore sampling the Hilbert transform in frequency also causes problems with the digital phase estimate.

Another complication occurs if the seismic trace is windowed to provide a localized amplitude spectrum. Application of a rectangular (boxcar) window in the time domain is a convolution with a sinc function in the frequency domain. Therefore taking a finite portion of a signal smoothes the frequency spectrum. The minimum-phase estimation from the smoothed amplitude spectrum will differ from the minimum-phase spectrum of the unsmoothed amplitude spectrum. (Hargreaves, 1992). Therefore smoothing introduces a systematic bias into the phase estimation.

The minimum-phase spectrum is sensitive to changes in the amplitude spectrum. If the amplitude spectrum has been multiplied by a constant, a phase rotation is introduced into the phase spectrum. This is because multiplication of the amplitude spectrum by a constant will become addition when the natural log of the amplitude spectrum is taken. This problem is significant in seismic data because the amplitudes of seismic data are scaled by an uncontrolled factor. This scaling factor could be in the recording stage, such as scaling due to geophone coupling.

Figure 1.4 illustrates how digital sample rates affect the estimated phase of an amplitude spectrum. Several digital constant Q impulse responses (Kjartansson, 1979) were created with varying values for the reference frequency, which determines the sample rate (Equation (1.28)). Since changing the phase spectrum of the pulse changes the position of the pulse in time (Karl, 1989), the phase differences between the resulting time-domain pulses can be analyzed by examining their relative positions.

Figure 1.3 shows a dispersion curve, described by Equation (1.19), for a constant-Q pulse. For digital approximations the reference frequency is taken to be the Nyquist frequency. Six different values for Nyquist frequency and the corresponding phase velocities were selected from the dispersion curve and a pulse in time was created for each. Pulse A was created with a Nyquist frequency of 1000 Hz. Essentially this is an analogue pulse relative to the other pulses. Pulse B has a Nyquist frequency of 800 Hz, Pulse C 600 Hz, Pulse D 400 Hz, Pulse E 250 Hz and Pulse F 200 Hz. Since Nyquist frequency is inversely related to the sample interval, a higher Nyquist frequency means the pulse is sampled more finely in time. The pulses are shown in Figure 1.4. The minimum-phase pulse that most closely resembles an analogue pulse (Pulse A) is more delayed in time than the other digital pulses. Therefore the Nyquist frequency and subsequent sample rate have a dramatic effects on the digital phase estimates which is manifested as an incorrect delay. The pulses corresponding to a higher Nyquist frequency (and therefore smaller sample interval) are delayed farther in time. The pulse shapes are

similar. Therefore, there will be a residual delay left in seismic data after minimum-phase deconvolution (Hargreaves and Calvert, 1991).

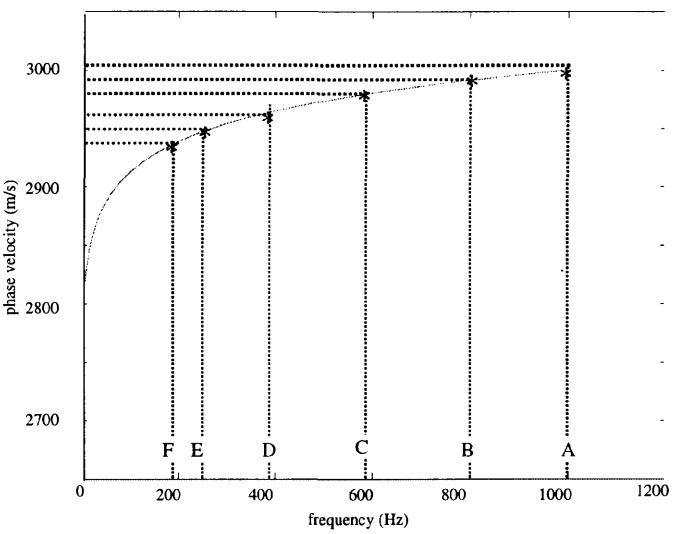

Figure 1.3: A dispersion curve for a constant Q pulse.

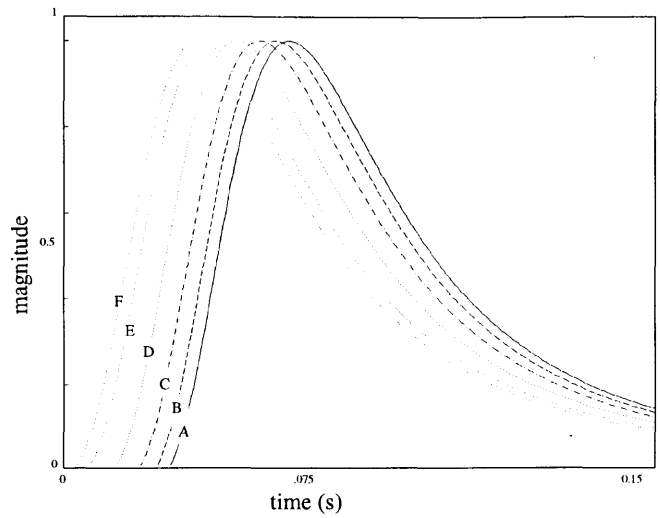

Figure 1.4: The minimum-phase pulses corresponding to different sample rates. The most finely sampled pulse (Pulse A) has been shifted in time the farthest. The most sparsely sampled pulse (Pulse F) has been shifted in time the least.

1.9 Deconvolution and inverse-Q filtering

The ultimate goal of seismic data processing is to recover the reflection coefficients of the subsurface. Part of the processing involved in achieving this end is the removal of source signature and correcting for anelastic attenuation. A method is desired that will restore the diminished amplitudes, correct for the phase rotation and compensate for the attenuated frequencies. Two methods commonly used to treat this problem are a combination of gain and stationary deconvolution, and inverse-Q filtering. A third method, nonstationary deconvolution (NSD), will be described in detail as the subject of this thesis.

1.9.1 Stationary deconvolution

Stationary deconvolution is a very common technique in seismic data processing. It is based on the convolutional model described in Section 1.5 (Equation (1.21)). The convolutional model has one known variable, the seismic trace, and two unknowns, the wavelet and the reflectivity series. This makes the deconvolution problem an ill-posed problem and assumptions must be made to solve it. There are several different algorithms for stationary deconvolution and one, Fourier-domain deconvolution, will be described in detail because of its similarity to NSD. The inadequacies of stationary deconvolution when applied to anelastically attenuated data will also be discussed.

Frequency-domain deconvolution (Yilmaz, 1987) is a type of stationary deconvolution. As the name suggests, the deconvolution operator is designed and applied in the frequency domain. It is assumed that the reflectivity is random and therefore its spectrum has constant power at all frequencies (a white spectrum). In reality, there is usually a low-frequency roll-off associated with reflectivity from sonic logs (Margrave, 1998), so this assumption is not strictly valid. The assumption of white reflectivity can be avoided if well control is available. Since the spectral color of the reflectivity is assumed to be white, all spectral 'character' of the seismic trace can be attributed to the wavelet. That is the general shape of spectrum of the input trace is thought to be similar to the unknown wavelet and the detail of the spectrum is due to the earth's reflectivity.). Figure 1.5 shows a random time series (which represents reflectivity), a wavelet, a trace (created by convolving the wavelet with the random time series) and their amplitude spectra. The

amplitude spectrum of the reflectivity has a flat shape. The amplitude spectrum of the trace seems to have the general shape of the wavelet with detail superimposed from the random time series.

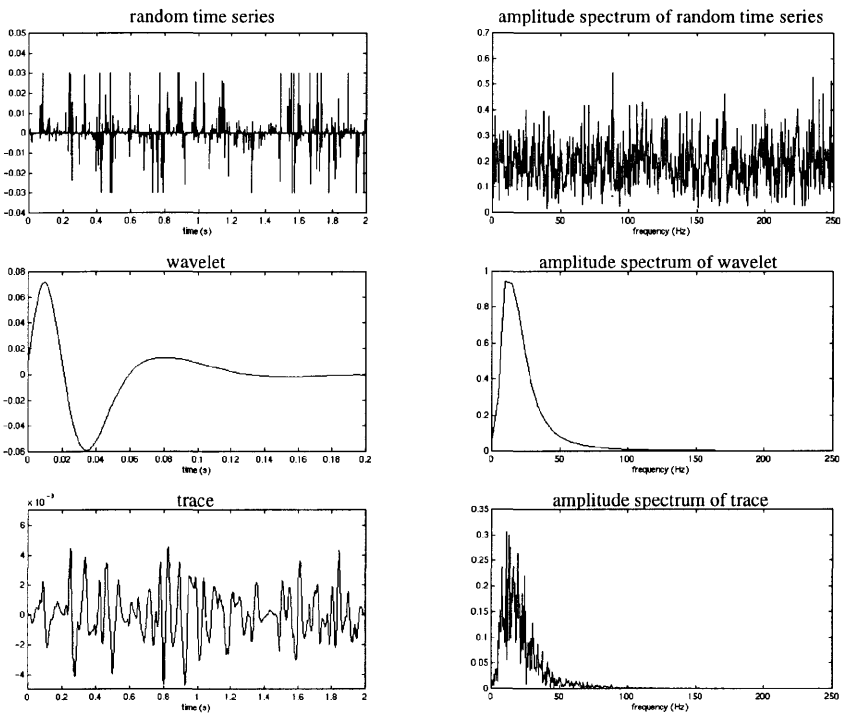

Figure 1.5: A random time series, wavelet, and trace (created by convolving the random time series and wavelet) and their spectra.

The first step in calculating the frequency-domain deconvolution operator is to calculate the power spectrum of a segment of the seismic trace. A segment of the trace that has a relatively high signal to noise ratio and includes the exploration target should be selected. The power spectrum of the segment, $|S(f)|^2$, is smoothed by convolution with

a smoother, a(f), in an attempt to remove the spectral content of the reflectivity from the spectrum:

$$\overline{|F(f)|^2} = |S(f)|^2 * a(f). \tag{1.32}$$

The square root of Equation (1.32) is the estimated amplitude spectrum of the source wavelet. It is called the amplitude spectrum of the forward operator

$$\overline{|F(f)|} \approx |W(f)| + n_w. \tag{1.33}$$

where n_w is a constant that has been added to stabilize the logarithm calculation of Equation (1.34) and the inversion of Equation (1.36). The constant is determined by multiplying the maximum of |W(f)| with a small number, typically between 10^{-1} and 10^{-6}. Conceptually, the constant is the Fourier transform of random noise.

At this point, a minimum-phase spectrum may be constructed for the forward operator using Equation (1.30):

$$\phi(f) = H\left[\ln(\overline{|F(f)|})\right], \tag{1.34}$$

The phase estimate from Equation (1.34) will not be a perfect estimation of the analogue minimum-phase spectrum of the forward operator. As mentioned in Section 1.8, the minimum-phase estimation from a smoothed amplitude spectrum will differ from the minimum-phase estimation of the unsmoothed amplitude spectrum.

The amplitude and phase spectra of the estimated source wavelet form the forward operator, F(f).

$$F(f) = |F(f)|\, e^{i\phi(f)}. \tag{1.35}$$

The forward operator, F(f) is then inverted and applied to the entire seismic trace. The spectrum of the input trace, S(f), modeled by Equation (1.22), is divided by the forward operator of Equation (1.35) to obtain an approximation of the reflectivity, R(f),

$$R(f) = \frac{S(f)}{F(f)}. \tag{1.36}$$

Wiener (spiking) deconvolution (Robinson, 1967) is the time-domain equivalent of frequency-domain deconvolution. A matrix equation involving the autocorrelation of the seismic trace is set up to determine the deconvolution operator in the time domain. The autocorrelation must be windowed to a pre-determined length and this windowing is equivalent to the smoothing process of frequency-domain deconvolution.

Predictive deconvolution (Peacock and Treitel, 1968) is a very important extension of Wiener deconvolution. A prediction operator is used to estimate a time-delayed prediction of the input trace. This time-delayed estimate is then subtracted from the input trace. The difference between the two time series is called the error series and it represents the unpredictable part of the trace, that is the reflectivity. The predictable part of the trace (which has been subtracted from the input trace) is the wavelet and multiple content.

Predictive deconvolution is a general type of deconvolution, of which spiking deconvolution is a special case. If the prediction operator is used to estimate a prediction of the input trace that is time-delayed by one sample, spiking deconvolution results. Predictive deconvolution is an effective tool in stationary multiple suppression. The prediction lag parameter, which determines how time-delayed the predicted estimate of the input trace will be, can be varied to compress the wavelet to varying degrees and bandlimit the signal.

Stationary deconvolution can approximately correct seismic data for source signature and frequency attenuation, however, it is not an ideal approach. It does not take the time-variant manner of attenuation into account. This means that it only treats the frequency domain problems associated with attenuation, such as broadening of the seismic pulse, and spectral decay. The time domain problems, such as amplitude decay, must be corrected for with a gain operator. The undesirable effects in the time and frequency domains were created through the same process and a method that compensates for them both simultaneously would be advantageous.

1.9.2 Inverse-Q filtering

Inverse-Q filters are deterministic nonstationary filters that attempt to remove the effects of anelastic attenuation. In general, inverse-Q filters explicitly model the anelastic attenuation and attempt to correct seismic data for the amplitude and phase effects. Unfortunately such methods generally have a high reliance on an estimate of Q, which is

notoriously difficult to estimate, as discussed in Section 1.6. In addition, a deconvolution must be applied separately to remove the effects of source signature. In this section, one method of inverse-Q filtering, will be explicitly described as an example of this type of technique and then several other methods will be described very briefly.

Hale (1981 and 1982) has developed several inverse-Q algorithms and one method, simply called an inverse-Q filter will be outlined here as an example of this type of technique. In this paper, Hale begins with a development of a forward Q filter. It is a method of modeling the spectrum of an anelastically attenuated waveform recorded at the surface. The Q matrix is a lower triangular time-variant matrix that describes the absorption. The matrix is lower triangular to represent the causality of the waveform. The Q matrix, $\overline{Q}$, is calculated by sampling the following function

$$q(t,\tau) = \mathrm{IFT}_{f\to t}\left\{\exp\left[\frac{-\pi |f|\tau}{Q_o} - i\phi(\tau,f)\right]\right\}, \qquad (1.37)$$

where IFT represents an inverse Fourier transform, f is the frequency, Q_o is an estimate of Q, τ is the two-way travel time and ϕ is the phase. The time coordinate, t, is mapped into the columns of $\overline{Q}$. The phase is computed as the Hilbert transform of the natural logarithm of the amplitude spectrum at constant τ, as in Equation (1.29).

Absorption can then be applied to the earth's reflection coefficients (the column vector R) via a matrix multiplication with a Q matrix, $\overline{Q}$. This matrix multiplication yields a column vector of the earth's impulse response, Y

$$Y = \overline{Q}R. \tag{1.38}$$

A seismic section can then be modeled as the vector containing the impulse response of the earth multiplied with a Toeplitz matrix containing the source waveform, $\overline{F}$

$$Z = \overline{F}Y = \overline{FQ}R, \tag{1.39}$$

where Z is the seismic trace.

To retrieve the reflection coefficients, R, from Equation (1.39), the section must be deconvolved to remove the source waveform and inverse-Q filtered to remove the effects of anelastic absorption. Examining Equations (1.38) and (1.39) it can be seen that, strictly speaking, the source waveform should be removed first and then the inverse-Q filter applied. However, it may be more practical to apply the inverse-Q filter first and then estimate the source waveform from the hopefully stationary seismic section. However, the deconvolution filter and the inverse-Q filter do not strictly commute and it would be desirable to apply them in the opposite order.

To obtain the inverse-Q filter, $\overline{Q}^{-1}$, a matrix $\overline{P}$ is first calculated by sampling the following function,

$$p(t,\tau) = IFT_{f\to t}\left\{\exp\left[\frac{+\pi |f|\tau}{Q_o} + i\phi(\tau,f)\right]\right\}. \qquad (1.40)$$

The time coordinate, t, is mapped into the rows of $\overline{P}$. Note that the matrix $\overline{P}$ is not the inverse of $\overline{Q}$. A matrix $\overline{S}$ is defined such that;

$$\overline{S} = [\overline{PQ}]^{-1} = \overline{Q}^{-1}\overline{P}^{-1}, \qquad (1.41)$$

and then the inverse of the Q matrix is calculated as

$$\overline{Q}^{-1} = \overline{S}\overline{P}. \qquad (1.42)$$

Once the inverse-Q matrix, $\overline{Q}^{-1}$, has been calculated it can be applied to Equation (1.39), before or after deconvolution. Inverse-Q filtering in conjunction with deconvolution yields a bandlimited approximation of the earth's reflection coefficients.

Several other inverse-Q filters have been proposed. Hale (1982) developed a routine called Q-adaptive deconvolution as an alternative to time-variant prediction error filtering. It is a combination of conventional prediction error filtering and inverse-Q filtering. Gelius (1987) essentially extended Hale's theoretical framework from Q-adaptive deconvolution into a frequency-domain inverse-Q filtering method where the filter is described by a Taylor series. Bickel and Natarajan (1985) propose reverse propagating superpositioned plane waves as a general inverse to the earth's attenuation filter. This filter is an outgoing propagating wavelet which increases with distance. The wave is propagated through reverse time with Q replaced by –Q. Hargreaves and Calvert

(1991) developed a Fourier-domain inverse-Q filter that is closely related to migration. Attenuation and dispersion are incorporated into the downward continuation operator. The wavefield is backward propagated to the surface to remove the effects of absorption.

Inverse-Q filters have several advantages and weaknesses. If the constant-Q model applies, inverse-Q filters remove absorption and increase the stationarity and resolution of a seismic section. In addition, some methods are more capable than others of correcting for dispersion. The weaknesses include a high reliance on the parameter, Q. The inverse-Q filters are, in general, deterministic and tend to apply a theoretical model to a seismic section. A deconvolution operator must be applied to a dataset in conjunction with the inverse-Q filter and the order of application is an issue.

1.9.3 NSD

This thesis proposes a data-driven nonstationary deconvolution method, NSD, that approximately corrects for anelastic attenuation, phase distortion and source signature. The purpose of NSD is to correct for time and frequency-domain effects simultaneously, in accordance with our understanding of how earth processes created these effects in the data. NSD has been developed from a model of a wavelet propagating through a 1-D earth which suffers frequency-dependent attenuation and dispersion along its travelpath. NSD estimates and removes the time and frequency domain effects of attenuation as well as the effects of source signature thereby increasing resolution and boosting the amplitude of events at later times. In a lossless medium (Q

approaches infinity) the propagating wavelet is time-invariant and the NSD process becomes stationary frequency-domain deconvolution and only removes the source signature. NSD can be considered as a type of data-driven inverse-Q filter with additional capability of being able to remove the source signature simultaneously.

NSD has two stages: operator design and operator application. The design phase must estimate the nonstationary amplitude spectrum of the attenuation and source signature and design an inverse operator. Once the inverse is known, it is applied as a nonstationary convolutional filter (Margrave, 1998). It will be shown that the operator design in NSD is less sensitive than inverse-Q filtering to variations in the estimate of Q.

CHAPTER 2: NONSTATIONARY FILTERS AND TIME-FREQUENCY ANALYSIS METHODS

2.1 Introduction

Nonstationary filtering and time-frequency analysis are techniques fundamental to NSD. Nonstationary filter theory (Margrave, 1998) is the method used to apply the NSD operator once it has been constructed. It will be explained, as it pertains to NSD, in this chapter. Time-frequency analysis of a seismic trace is required in the operator design stage of NSD. Several methods of time-frequency analysis of a seismic signal are available, such as time-variant spectra (TVS), instantaneous attributes, Wigner distribution and the wavelet transform. Each method will be described and their strengths and weaknesses will be discussed in relation to their suitability for NSD. For reasons explained in Section 2.3.1, the TVS approach has been chosen as the time-frequency analysis technique most appropriate for NSD.

2.2 Nonstationary filtering

Nonstationary filtering (Margrave, 1998) is a filtering technique that applies a time-variant filter continuously to seismic data. Nonstationary filtering is an extension of stationary convolution. The stationary convolution integral is given by

$$g(t) = \int a(t-\tau)h(\tau)d\tau, \qquad (2.1)$$

where g(t) is the filtered trace, $h(\tau)$ is the input trace, and $a(t-\tau)$ is the impulse response of the filter. The integration limits are from negative infinity to infinity. The time variable,

t, is the output time and the variable, τ, tracks the input time. Equation (2.1) can be modified for nonstationary applications by letting the impulse response of the filter, vary arbitrarily with time. If the filter is allowed to vary with the input time, τ, then nonstationary convolution results

$$g(t) = \int a(t-\tau,\tau)h(\tau)d\tau. \tag{2.2}$$

Equation (2.2) corresponds to the linear superposition of scaled impulse responses of a nonstationary filter. The other possible form of nonstationary filtering is called nonstationary combination and the impulse response of the filter is allowed to vary with output time.

$$\overline{g}(t) = \int a(t-\tau,t)h(\tau)d\tau. \tag{2.3}$$

It does not correspond to a linear superposition of scaled impulse responses, but it is advantageous in that the filter is allowed to change abruptly as a function of output time, t.

The operator in Equations (2.2) and (2.3) is designed and applied in the time domain. From stationary filtering it is known that the time domain is not always optimal for computational efficiency or filter design. Therefore, nonstationary convolution and nonstationary combination have been reformulated in the Fourier domain, as well as the mixed Fourier-time domain. Only the alternate forms of nonstationary convolution will

be shown here. For a more complete treatment of this subject see Margrave (1998). The full Fourier domain representation of nonstationary convolution becomes

$$G(f) = \int H(F)A(f, f - F)dF, \tag{2.4}$$

where H(F) and G(f) are Fourier transforms of g(t) and h(τ). A(f,F) is the frequency connection matrix and is the 2-D Fourier transform of a(t,τ)

$$A(f,F) = \iint a(t,\tau)e^{-2\pi ift}e^{-2\pi i\tau F}dtd\tau. \tag{2.5}$$

The mixed domain formulation of nonstationary convolution is

$$G(f) = \int \alpha(f,\tau)h(\tau)e^{-2\pi if\tau}d\tau, \tag{2.6}$$

where α(f,τ) is the nonstationary transfer function. The nonstationary transfer function is related to a(t,τ) by

$$\alpha(f,\tau) = \int a(t,\tau)e^{-2\pi ift}dt \tag{2.7}$$

It may be easier to build the operator in the mixed domain where it can be stated explicitly in both time and frequency and move it to the Fourier domain for application. This is the case in NSD where α(f,τ) is estimated directly from the seismic trace, as an operator designed to remove the effects of source signature and attenuation.

2.3 Time-frequency decomposition techniques

For NSD, a two-dimensional time-frequency operator, $\alpha(f,\tau)$, is desired for application to seismic data. The operator is a time-frequency matrix containing the inverse of the undesirable effects that should be removed, in particular the source signature and attenuation effects. The estimation of this operator directly from the data can be accomplished by decomposing a seismic trace onto a time-frequency grid and processing the decomposition. Therefore a means of decomposing seismic data onto a time-frequency grid is required for NSD. It is important that the time-frequency decomposition can be easily interpreted for physical meaning. There are several methods of joint time-frequency analysis and four will be examined: time-variant spectra, instantaneous frequency attributes, the Wigner distribution, and the wavelet transform. Each method has particular strengths and weaknesses related to its suitability for NSD.

2.3.1 Time-variant spectra

One method of building a time-frequency grid of an input trace is with a time-variant amplitude spectrum (|TVS|) or alternately with a time-variant power spectrum, called the spectrogram (Cohen, 1995). First, the method of calculating the |TVS| will be explained. Next, the effects of two parameters, window increment and window length, on the |TVS| will be described. Finally advantages and disadvantages of |TVS| will be discussed, along with its suitability for NSD.

A TVS is basically a decomposition of a time series onto a time-frequency matrix. Each spectrum, localized at a particular time, TVS(τ,f), is calculated by taking the *short-time Fourier transform* (Cohen, 1995),

$$TVS(\tau, f) = \int x(t)h(t-\tau)e^{-i2\pi ft}dt, \qquad (2.8)$$

where x(t) is the trace and h(t-τ) is a time-shifted window. A window is a function whose magnitude is localized near the origin and decays rapidly elsewhere. It is designed to suppress the signal at distant times and leave it unaltered around the time, t=τ. When multiplied with a signal a window serves to localize the properties of that signal in time.

The time-variant amplitude spectrum, |TVS|(τ,f), can be calculated by taking the magnitude of Equation (2.8). The amplitude spectrum, |TVS|(τ,f), becomes a row in the time-frequency grid at time, τ, and it measures the frequency distribution localized around that time. The window is incremented along the trace, with an overlap of typically 70-90% between windows, and the |TVS|(τ,f)is calculated for each window increment. Each amplitude spectrum will form a row in the resulting grid. Figure 2.1 depicts how the |TVS| is calculated. In the grey level |TVS| display, black represents large positive numbers and white is zero.

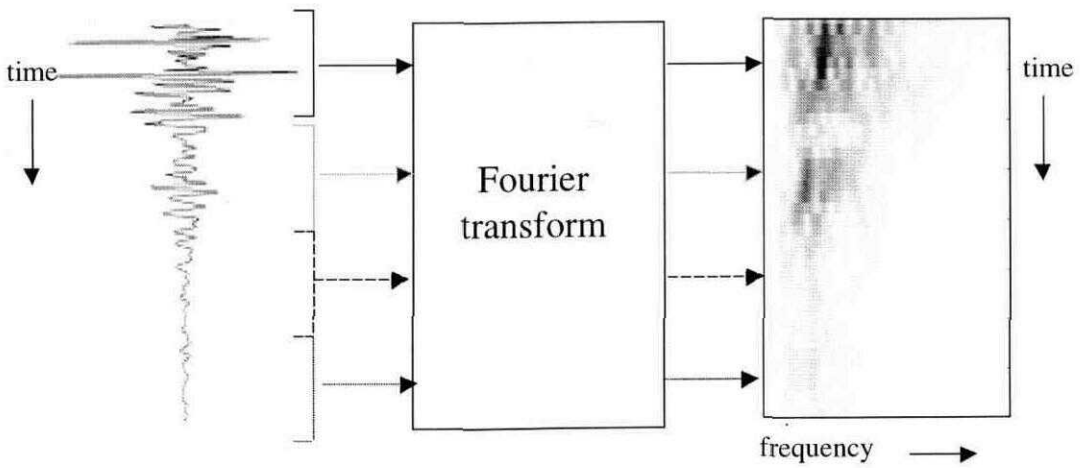

Figure 2.1: Calculation of a |TVS| from an input trace. The trace is windowed and the Fourier transform of each windowed segment is calculated. The resulting amplitude spectrum forms a row in the resulting |TVS| grid. In the grey level |TVS| display, black represents large positive numbers and white is zero.

The trace in Figure 2.1 is a synthetic trace created by applying a Q filter (Q=25) superimposed with a minimum-phase wavelet, to a reflectivity series. The |TVS| is therefore composed of the time-variant spectra of the source signature, reflectivity and attenuation. The source waveform is stationary and bandlimited. It is the broad spectrum at early times and is marked by the absence of very low frequencies as can be seen from Figure 2.1. From Figure 2.1 it can also be seen that this initial spectrum decays rapidly in both time and frequency. This exponential attenuation dominates the |TVS| and the effects of reflectivity provide detail in the |TVS|.

The window increment is an important parameter in the |TVS| computation because it is essentially the time sample interval of the |TVS|. In addition, the window increment is inversely proportional to the computation time of the |TVS|. Therefore this parameter must be chosen carefully so that the computation time of the |TVS| is reasonable and the time-variant effects which are to be examined are faithfully recorded in the |TVS|. This is a concern for NSD as the steep exponential attenuation inherent in an anelastically attenuated input trace may be distorted or aliased if the trace is sampled too coarsely.

Another important parameter in the calculation of the |TVS| is the window length. The resolution of the |TVS| in time and frequency is determined by window length as governed by the uncertainty principle (Cohen, 1995). The uncertainty principle is given by

$$TB \geq \text{constant} \tag{2.9}$$

where T is the duration of a signal and B is the bandwidth of its spectrum. The duration of the signal is determined from the length of the window that has been applied to the seismic trace. A detailed proof of the uncertainty principle can be found in Cohen (1995). In a few words, the uncertainty principle is the property that a narrow time-domain signal will have a broad bandwidth and a broad time-domain signal will have a narrow bandwidth. The bandwidth and duration of a signal cannot both be made arbitrarily narrow simultaneously.

The choice of window length has important implications regarding the time and frequency resolution of the |TVS|. A |TVS| created with a long window will have excellent resolution in frequency but poor temporal resolution, and a |TVS| created with a short window will have greater time resolution at the expense of frequency resolution. Figure 2.2 demonstrates how window length affects the time and frequency resolution of the |TVS|, according to the uncertainty principle. Two |TVS| were created from the same seismic trace, one with a small window (|TVS| a) and the other with a larger window (|TVS| b). |TVS| a looks smeared parallel to the frequency axis, but shows fine variation parallel to the time axis. This indicates that this |TVS| has poor resolution in frequency, and good resolution in time. In contrast, |TVS| b looks smeared parallel to the time axis and shows variation parallel to the frequency axis. From this it can be inferred that this |TVS| has poor resolution in time and good resolution in frequency. The |TVS| cannot have ideal time and frequency localization simultaneously therefore a decision must be made about the purpose of the |TVS| and whether time or frequency resolution has priority, when choosing a window length.

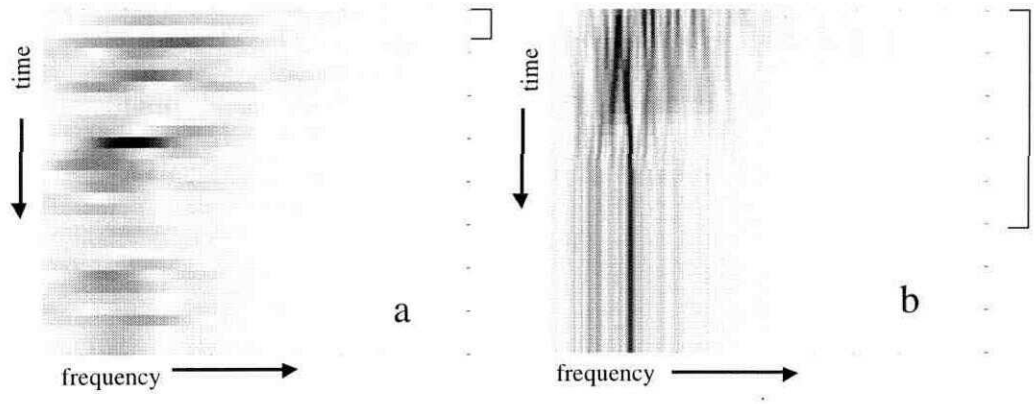

Figure 2.2: Example of how window length affects the time and frequency resolution of the |TVS|. The uncertainty principle dictates that as the resolution in time increases the resolution in frequency decreases. Two |TVS| were calculated from a seismic trace using differing window lengths. The windows are shown to the right of each |TVS|. |TVS| a has a small window length and therefore a high resolution in time at the expense of a frequency resolution. |TVS| b was created with a larger window and has a greater localization in frequency and poor localization in time.

There are several disadvantages associated with the |TVS| approach. As can be seen from Equation (2.8) a spectrogram mixes energy and information from both the window and the signal. The instantaneous energy cannot be calculated by summing the energy distribution for all frequencies at a particular time because of the entangled window function (Cohen, 1995). In addition, when constructing a spectrogram from a finite signal, care must be taken to compensate for windowing off the ends of the signal.

The |TVS| has been chosen as the most suitable method of time-frequency decomposition for the NSD algorithm. TVS provides a grid in both time and frequency, and the familiarity of the Fourier transform and the ease of interpretation are the main advantages. As described, the entanglement of the window function and signal is the biggest drawback to this method, as applied to NSD.

2.3.2 Instantaneous frequency

Nonstationary spectral information can also be calculated with the instantaneous frequency attribute. Instantaneous frequency provides a localized estimate of the mean frequency of a spectrum as a function of time. It can be calculated from a complex representation of a real seismic trace and is associated with a specific point in time.

To calculate instantaneous frequency a complex trace must be synthesized from a real trace. Two methods of calculating the complex trace are discussed below. Next, the calculation of instantaneous frequency from the complex trace is shown. Finally, the advantages and disadvantages with instantaneous frequency are discussed and its appropriateness to NSD.

There are two motivations for constructing a complex trace from a real seismic trace. The primary goal is to calculate the instantaneous frequency. It will be shown later, in Equation (2.21), that the instantaneous frequency is the first time derivative of the instantaneous phase of the complex trace. Therefore a method must be devised for

estimating a temporal phase related to the seismic data. One method of doing this is with complex trace analysis.

The second motivation to construct a complex trace is related to the symmetry of the Fourier spectrum of a real trace. The spectrum of a real trace, $S_r(f)$, has Hermitian symmetry, that is, it is conjugate anti-symmetric about the zero frequency

$$S_r(-f)=S_r^{*}(f), \tag{2.10}$$

where * denotes complex conjugate. Thus

$$|S_r(-f)| = |S_r(f)|. \tag{2.11}$$

This property makes it difficult to calculate meaningful frequency averages for real-valued traces, as they will equal zero (Cohen, 1995). A trace that has zero amplitude for the negative frequencies would therefore be advantageous. This can be done by allowing the real trace to be the real part of a suitable complex trace.

The complex seismic trace, z(t), is written as

$$z(t)=s_r(t)+is_i(t) = A_c(t)e^{i\phi(t)} \tag{2.12}$$

where $s_r(t)$ is the real seismic trace and $s_i(t)$ is the imaginary part of the trace, which must be determined. Requiring the negative frequencies to be zero leads to a unique form for the complex trace (Cohen, 1995). The imaginary part of the complex trace is related to the real component by the Hilbert transform, H:

$$s_i(t) = H[s_r(t)] = \int_{-\infty}^{\infty} S_r(\tau)\frac{1}{t-\tau}d\tau. \qquad (2.13)$$

The amplitude of the complex trace, $A_c(t)$, and the phase of the complex trace, $\phi(t)$, are given by

$$A_c(t) = \sqrt{s_r^{\,2}(t) + s_i^{\,2}(t)} \qquad (2.14)$$

$$\phi(t) = \tan^{-1}\left(\frac{s_i(t)}{s_r(t)}\right), \qquad (2.15)$$

Given a real trace, its complex equivalent can also be calculated in terms of Fourier integrals (Taner et al., 1979). The process is mathematically equivalent to using the Hilbert transform (Cohen, 1995), however, the method using Fourier integrals clearly demonstrates some of the concepts associated with the complex trace. The first step in this method is to calculate the Fourier transform of the real trace. Next, the amplitudes of the negative frequencies are set equal to zero and the amplitudes of the positive frequencies are doubled, so that the real part of the complex signal will be equal to the original seismic trace. The inverse-Fourier transform of the modified spectrum is calculated to realize the complex trace, z(t):

$$z(t) = \frac{2}{\sqrt{2\pi}} \int_0^\infty S_r(f) e^{2\pi i f t} df \quad . \tag{2.16}$$

where $S_r(f)$ is the Fourier spectrum of the real trace. For comparison, the inverse Fourier transform of the real trace is

$$s_r(t) = \frac{1}{\sqrt{2\pi}} \int_{-\infty}^\infty S_r(f) e^{2\pi i f t} df \quad . \tag{2.17}$$

Equations (2.16) and (2.17) differ by the limits of integration and the coefficient of 2 in front of the integral of Equation (2.16). In this manner, a complex trace that has zero amplitude for negative frequencies can be calculated.

To derive the formula for instantaneous frequency, a definition of average Fourier frequency, $\langle f \rangle$, is required

$$\langle f \rangle = 2\pi \int f \, |S_r(f)|^2 \, df \quad , \tag{2.18}$$

where f is the stationary Fourier frequency, and $|S_r(f)|^2$ is the normalized power spectral density. To avoid the slow and unnecessary calculation of the spectrum, $S_r(f)$ Equation (2.18) can be written in terms of the normalized energy per unit time, $|s_r(t)|^2$, using the frequency operator, $\Omega = \frac{1}{i} \frac{d}{dt}$ (Cohen, 1995):

$$\langle f \rangle = \frac{1}{2\pi}\int s_r^{*}(t)\frac{1}{i}\frac{d}{dt}s_r(t)dt = \frac{1}{2\pi}\int (\phi'(t) - i\frac{A_r'(t)}{A_r(t)})A_r^{2}(t)dt \quad , \qquad (2.19)$$

where * denotes complex conjugate, $A_r(t)$ is the amplitude of the real trace, $\phi(t)$ is the phase, and the prime symbol $(')$ denotes a derivative with respect to time. The imaginary term, $\int -i\frac{A_r'(t)}{A_r(t)}A_r^{2}(t)dt$, is zero because average frequency is purely a real function. Therefore, Equation (2.19) becomes

$$\langle f \rangle = \frac{1}{2\pi}\int \phi'(t)\,|s_r(t)|^2\,dt \quad . \qquad (2.20)$$

Comparing Equation (2.20) to Equation (2.18) it can be seen that in Equation (2.20) some function, $\phi'(t)$ is being averaged to obtain the average frequency. This function is appropriately named the instantaneous frequency and is related to the instantaneous phase by

$$f_i(t) = \frac{\phi'(t)}{2\pi}, \qquad (2.21)$$

where $f_i(t)$ is the instantaneous frequency and the phase, $\phi(t)$, is given by Equation (2.15). Taking the derivative of the arctangent of Equation (2.15), Equation (2.21) can be rewritten as

$$f_i(t) = \frac{s'_i(t)s_r(t) - s'_r(t)s_i(t)}{2\pi A_c^{\,2}(t)}. \qquad (2.22)$$

The results from the calculation of instantaneous frequency must be examined closely and judged whether they are physically meaningful. Cohen (1995) explains several paradoxes related to the instantaneous frequency that causes distrust in this spectral measurement. In general, the instantaneous frequencies may be vastly different from the frequencies contained in the Fourier spectrum. For instance, the instantaneous frequency may contain frequencies outside of the Fourier spectrum. Also, the instantaneous frequency may be negative although the spectrum of the complex signal is zero for negative frequencies, or the instantaneous frequency may be outside the bandwidth of a bandlimited signal. Another paradox is that the instantaneous frequencies may be continuous and range over infinite values for a discrete line spectrum.

Instantaneous frequency is a tool to examine the nonstationary spectral character of seismic data, however it is not appropriate for use in designing the NSD operator. The temporal resolution of instantaneous frequency is infinite, and therefore by the uncertainty principle the frequency resolution must therefore be zero. NSD requires a time-frequency analysis technique that has adequate resolution in both time and frequency. Instantaneous frequency does not provide a time-frequency grid. In addition, instantaneous frequency can be noisy and the paradoxes associated with it make interpretation difficult.

2.3.3 Wigner distribution

The Wigner distribution is another form of time-frequency analysis. It is a time-frequency characterization achieved through a bilinear transform. The Wigner distribution (WD) can be applied to continuous signals with the continuous Wigner distribution (CWD), or to sampled signals with the discrete Wigner distribution (DWD) (Claasen and Mecklenbrauker, Part II, 1980). First, the CWD will be described and then some properties of the CWD will be discussed. Finally the advantages and disadvantages of the CWD and its suitability for NSD is discussed.

The CWD, W(t,f), is given by

$$W(t,f) = \frac{1}{\sqrt{2\pi}} \int s_1^*(t - \frac{1}{2}\tau) s_2(t + \frac{1}{2}\tau) e^{-2\pi i f \tau} d\tau \quad , \tag{2.23}$$

or

$$W(t,f) = \frac{1}{\sqrt{2\pi}} \int S_1^*(f + \frac{1}{2}\theta) S_2(f - \frac{1}{2}\theta) e^{-it\theta} d\theta \quad , \tag{2.24}$$

where s(t) is a signal, S(f) is its Fourier transform and * represents the complex conjugate. If s_1 and s_2 are the same signal, and S_1 and S_2 are its Fourier spectrum, the above equations are said to be the auto-Wigner distribution (Claasen and Mecklenbrauker, Part I, 1980). If s_1 and s_2 are not the same signal, then the equations are called the cross-Wigner distribution. The WD calculated from the time-domain signal as in Equation (2.23), and

the WD from the spectrum of the signal (Equation (2.24)) are equivalent and this reflects the symmetry between the time and frequency domains.

The process of calculating the auto-Wigner distribution is like folding the signal, at some time, t, onto itself. The properties in the overlapped section will be present in the transform at the time corresponding to the fold. This explains why the WD is a noisy distribution. Noise that is present for a short duration in the time signal will be present at many times in the resulting WD because it will occur in many of the overlaps of the signal. Figures (2.3) and (2.4), both taken from Cohen (1995), illustrate how this works.

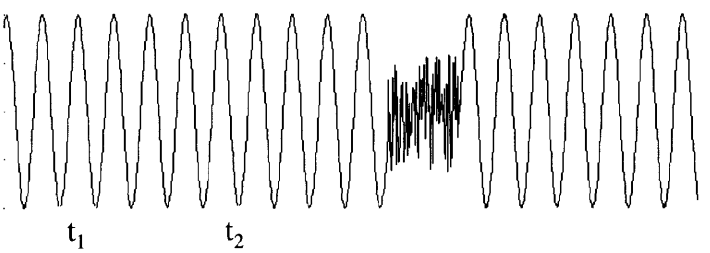

Figure 2.3: Cosine signal containing noise of a short duration. If the signal is folded about time t_1, there will be no noise contained in the overlap and therefore no noise will be contained in the WD at time t_1. However if the signal is folded over at time t_2, the noise will be present in the overlapped signal and present in the WD at time t_2.

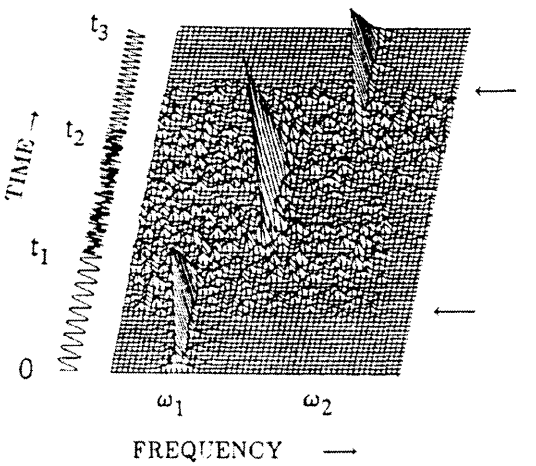

Figure 2.4: A Wigner distribution showing noise. The WD is noisy even where no noise existed in the original signal. The original signal is shown on the left.

Unlike some other forms of time-frequency analysis, the WD only exists for the same time as the signal exists. It is zero before the signal starts and after it ends. Similarly for a bandlimited signal, the WD only exists for the bandwidth of the signal. The WD is said to have finite support because of this property. However, for a signal that is turned off for a finite amount of time and turned back on, the WD will not necessarily be zero in the time interval where there is no signal.

One of the greatest advantages of the WD is that meaningful measurements can be calculated from the WD itself. For instance the energy density and the energy density spectrum can be calculated from the WD through the following equations

$$2\pi \int W(t,f)df = |s(t)|^2 \quad , \tag{2.25}$$

$$2\pi \int W(t,f)dt = |S(f)|^2 \quad . \tag{2.26}$$

The average time, $\langle t \rangle_f$, and average frequency, $\langle f \rangle_t$, can be calculated from the WD using

$$\langle f \rangle_t = \frac{2\pi}{|s(t)|^2} \int fW(t,f)df \quad , \tag{2.27}$$

$$\langle t \rangle_f = \frac{1}{|S(f)|^2} \int tW(t,f)dt \quad . \tag{2.28}$$

The energy of the signal and spectrum can be computed by integrating over the WD, however it is important to remember that the WD itself only roughly reflects the energy in the signal or spectrum. For this reason, the WD must be interpreted carefully.

The interpretation of the Wigner distribution can be difficult, in part due to a phenomenon known as cross terms in the distribution. The cross terms can be seen by taking the WD of a signal, s(t), expressed as the sum of two other signals

$$s(t) = s_1(t) + s_2(t) \quad . \tag{2.29}$$

The WD of s(t) becomes

$$W(t,f)=W_{11}(t,f)+W_{22}(t,f)+W_{12}(t,f)+W_{21}(t,f). \quad (2.30)$$

Since $W_{21}=W_{12}^*$, Equation (2.30) can be re-written as

$$W(t,f)=W_{11}(t,f)+W_{22}(t,f)+2\mathrm{Re}\{W_{12}(t,f)\}. \quad (2.31)$$

It can be seen from Equation (2.31) that the sum of two signals is not simply the sum of their WD. The additional term $2\mathrm{Re}\{W_{12}(t,f)\}$is called the cross term or interference term. The cross terms can produce disturbing effects. They can show up in the time-frequency plane where they are not expected and often do not conform to the physical model.

The Wigner distribution has properties that make it appealing to use in the NSD algorithm, however the disadvantages associated with it outweigh the advantages. The Wigner distribution provides a time-frequency matrix from which energy measurements can be calculated. In addition, the WD is computed to have the same time interval as the input signal or the same frequency interval as the input Fourier spectrum and so end effects are avoided. The WD has good joint time-frequency resolution, avoids the use of windows and, unlike the spectrogram, meaningful estimates of energy density can be measured from the WD. However, the WD is unsuitable for NSD because it is only a rough characterization of the energy in the signal or spectrum. In addition, the bilinear nature of the WD causes surprising values, called cross terms, in the representation. The

WD is also noisy because it distributes the noise at a particular time in the signal throughout the WD.

2.3.4 Wavelet transforms

The wavelet transform is a time-scale analysis technique that has been designed to provide greater joint resolution than methods based on the Fourier transform. A wavelet transform, WT, decomposes a signal into time-scale space by using a set of basis functions, called wavelets. All of the wavelets in the basis are scaled and translated versions of a prototype wavelet called the mother wavelet. The decomposition from the wavelet transform can be displayed as a time-scale grid or converted to a time-frequency grid. The wavelet transform is reversible and the original signal can be regenerated from the transform coefficients.

A basic introduction to the continuous wavelet transform will be provided. First, some background information, relating to basis functions, compact support, wavelets, mother wavelets, scaling and translation, is explained. Then, methodology of the forward transform is presented, followed by a discussion of how scale relates to Fourier frequency. Next, how TVS achieves better resolution through scale analysis than methods based on the Fourier transform is explained. Finally the advantages, disadvantages and aptness of WT for NSD are discussed.

Any vector in a complete vector space can be decomposed by a linear combination of linearly-independent basis vectors of that space. For instance, any vector

in Euclidean two-space can be built from a linear combination of the vectors [0 1] and [1 0]. The idea of a basis can be expanded to functions by representing any function as a linear combination of basis functions. For example, sine and cosine functions (the complex exponential) are the basis functions of a Fourier transform. The basis functions for a wavelet transform are wavelets.

A wavelet is an oscillatory signal that is simultaneously localized in both the time and frequency (Fourier) domains. A wavelet with compact support, meaning that it must be zero outside a certain radius, is desirable for the WT. The wavelets in the basis of a WT have a special relationship to each other; each wavelet is derived through a translation and scaling of a prototype wavelet called the mother wavelet. This type of basis is called a scale-varying basis (Graps, 1995). There are infinite possibilities of mother wavelets to choose from and it is best to find a wavelet that "fits" your data. The selection of the mother wavelet strongly affects the output from the WT and is therefore very important.

Scale and translation are important concepts associated with the WT. Scale is inversely related to frequency and describes the duration or width of a wavelet. Changing the scale of the mother wavelet is analogous to either compressing or dilating it in time. The wavelet transform, as will be shown later, analyzes the signal repeatedly with wavelets of varying scale. The scale is varied to extract different information from the data. Large scales correspond to a global view of the signal's structure and small scales

show detail. Translation of a wavelet is a shift along the time axis in the wavelet's position relative to its original position.

The continuous wavelet transform maps a time series with equal time sampling, x(t), into translation-scale space, $\xi(\tau,s)$ using the following integral (Polikar, 1994)

$$\xi(\tau,s) = \frac{1}{\sqrt{s}} \int x(t) \Psi^*(\frac{t-\tau}{s}) dt \quad , \tag{2.32}$$

where s is the scale, τ is the translation, t is the running time of the time series, and $\Psi(t)$ is the mother wavelet. The asterisk (*) indicates the complex conjugate. The wavelet is also referred to as the window, because it isolates a section of the time series. The output from Equation (2.32), $\xi(\tau,s)$, is called the wavelet coefficient.

The equation governing the forward WT states that the wavelet (at varying scales) is compared to the signal at each time. Starting at the beginning of the time series, $t=\tau=0$, and at a single low scale, the wavelet is multiplied with the signal and integrated over all time. This result is the wavelet coefficient for a scale, s, and a translation, τ. The wavelet is then translated repeatedly and the integral computed at each new position of the wavelet, until the end of the time series is reached. These calculated wavelet coefficients fill a row in the WT grid (also called a wavelet map). The scale is incrementally increased and the process repeated until the entire grid has been filled.

The wavelet coefficients represent the similarity of the signal to the wavelet. If the signal has a spectral component that corresponds to the current value of the scale at a particular translation, then the wavelet coefficient will be high at this translation and scale. If the spectral component that corresponds to a particular scale is absent at a particular translation, then the coefficient will be low or zero. The narrowest wavelet of the WT should have a width similar to the highest frequency component of the signal. Thus, the WT can be thought of as shrinking and stretching a wavelet along the time axis and comparing the shape of the signal to that of the wavelet at each time (Lewalle, 1995). Figure 2.5 shows the process of comparing a wavelet of a certain scale to a signal.

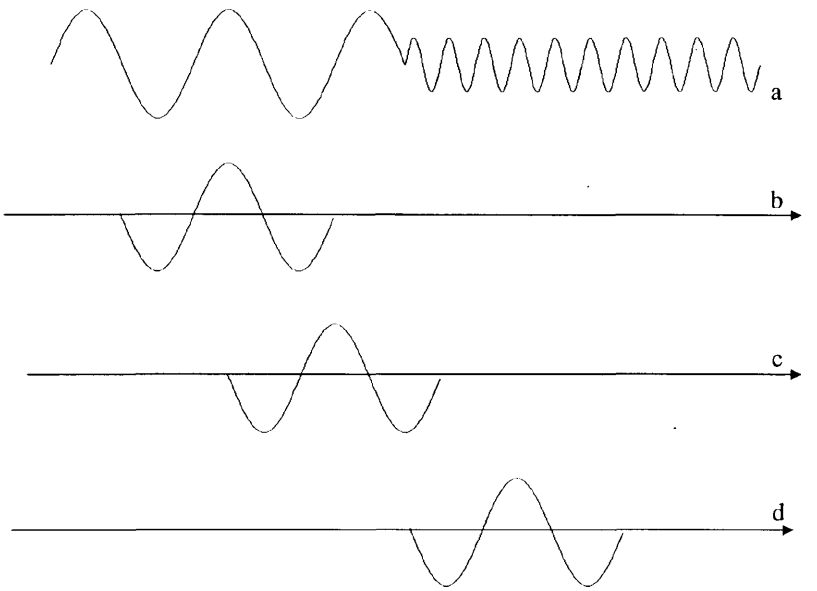

Figure 2.5: The wavelet of scale, s, is compared to the signal (2.5a) at various translations. The coefficient will be large when the wavelet is at the position shown in 2.5b because the wavelet at this position and scale are similar. In 2.5c, the wavelet and signal are at a similar scale but the translation of the wavelet lines up the wavelet's peak to the zero crossing of the signal and therefore a lower coefficient is calculated. The scale of the wavelet does not match the signal in case 2.5d and the wavelet coefficient would be very small.

For use in NSD, the scale of Equation (2.32) must be converted to Fourier frequency. A quick and rough way of achieving this is by interpolating the time-scale grid of the WT and mapping it into a grid of time and inverse-scale. The wavelet chosen for the WT will directly determine the success of this effort. Scale approximates Fourier

period more closely for some wavelets than others. Wavelets similar to sine or cosine functions, such as the wavelet shown in Figure 2.5, have scale similar to Fourier frequency (Torrence and Compo, 1998).

A more precise way of relating scale of a WT to equivalent Fourier period for a particular wavelet function is by inputting a cosine wave of known frequency into Equation (2.32). The relationship between wavelet scale and Fourier period can be determined by computing the scale at which the wavelet power spectrum (the squared magnitude of the wavelet transform) reaches a maximum (Torrence and Compo, 1998).

The WT has increased time-frequency resolution relative to the TVS because of the special nature of its basis functions. The most suitable wavelets are compactly supported and bandlimited. These characteristics, in addition to varying the wavelets with scale in the WT allow for excellent joint localization in time and frequency (Graps, 1995).

Scale variation is advantageous for analyzing different spectral components. High frequencies usually occur in short periods of time and therefore good time localization is desirable when studying these frequencies. This localization is achieved through employment of a narrow window or increased scale. Increased time localization is at the expense of frequency localization as governed by the uncertainty principle, and therefore high frequencies will be analyzed at a lower frequency resolution. This is a compromise of frequency resolution, however it allows good time localization.

Good time localization is not necessary for low frequencies because they usually last for the duration of the signal. Therefore there is no advantage to increasing the time resolution and limiting the frequency resolution by applying a narrow wavelet. The scale can be decreased to widen the wavelet and the low frequencies can be analyzed at an appropriate time and frequency resolution. In short, a broad examination of the structure of a signal is undertaken when the wavelet is large and when the analysis window, wavelet, becomes narrow, the detailed properties of the signal can be seen (Chakraborty and Okaya, 1995). The strength of a WT is a compromise of temporal and spectral localization due to the varying window widths.

An important difference between a WT and a |TVS| is that the wavelets of a WT vary with scale and the windows of |TVS| are equally sized, as can be seen by comparing Equations (2.8) and (2.31). Since window length determines resolution, the resolution of the WT and the |TVS| will be different. The grid of a spectrogram is comprised of square tiles of equal time frequency resolution and the grid of a WT is comprised of rectangles of changing dimensions and therefore changing resolution. The rectangles must have equal area because of the fixed relationship between time and frequency. Figure 2.6 shows the square tiles of the spectrogram and the rectangles of the WT.

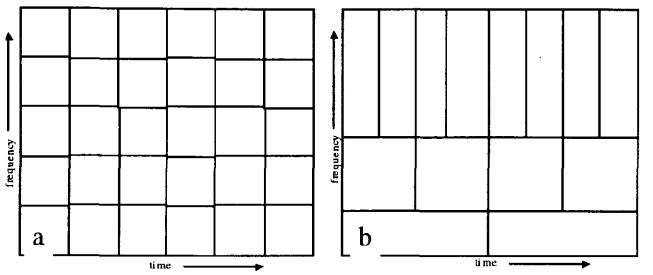

Figure 2.6: A comparison of the resolution of the ITVSI and wavelet transform. The ITVSI is comprised of square tiles (2.16a) and the resolution is constant everywhere. The wavelet map of the WT is comprised of rectangles (2.6b) and has changing resolution with frequency.

The WT is a good candidate for use in NSD. It provides a time-scale grid that can be converted to a time-frequency grid and interpreted physically. The choice of mother wavelet and scale offer a flexible approach, and the high resolution in time and frequency is also advantageous. The most significant advantage of the WT is increased resolution in time and frequency. Wavelet transforms are also better for analyzing discontinuous data because of the increased time localization. Using a WT in the operator design stage of NSD merits further investigation.

2.3.5 Section summary

TVS is the most suitable time-frequency decomposition method for NSD. It provides a grid in time and frequency that can be easily interpreted. In addition its close relationship to the familiar Fourier transform is an advantage.

Instantaneous frequency is unsuitable for the purposes of NSD because it does not provide a time-frequency grid and spectral measurements have zero frequency resolution. In addition, the results may be difficult to interpret and the frequency resolution is zero. The WD is also unsuitable for NSD. It provides a time-frequency grid with good joint resolution. However, the main drawback to the WD is that physical interpretation can be difficult.

The WT is an alternative time-frequency distribution for NSD. It offers a time-frequency grid with excellent joint resolution. It can be interpreted physically and the choice of wavelet and scale allow for flexibility. Further investigation of designing the NSD operator using a WT would be interesting.

CHAPTER 3: NSD

3.1 Introduction

The NSD (nonstationary deconvolution) algorithm is developed in this chapter. The chapter begins with a discussion of the spectral model on which NSD is based and some of the assumptions associated with it. Next, the NSD algorithm is developed from the spectral model and finally, three different extensions of NSD are described. The extensions of NSD are designed to increase flexibility and efficiency.

3.2 Nonstationary spectral model and assumptions

3.2.1 Nonstationary spectral model

The purpose of NSD is to recover the reflectivity from a seismic trace by removing the source signature and nonstationary propagation effects. To achieve this a model that relates the ITVSI of the input trace to those effects which should be removed is required. In this section, the nonstationary convolutional model of the input trace will be developed from the stationary convolutional model.

As mentioned, an extension of the stationary convolutional model, Equation (1.22), into the nonstationary realm is postulated. The nonstationary (dependent on time and frequency) spectrum, S(t,f), of a raw 1-D seismic trace can be modeled as

$$S(t,f) = R(t,f)M(t,f)W(f)e^{-\pi a(t,f)ft + i\phi(t,f)}, \qquad (3.1)$$

where R(t,f) is the TVS of the earth's reflectivity function, M(t,f) is the nonstationary spectrum describing multiple reflections, W(f) is the stationary spectrum of the source signature including stationary near surface effects, a(t,f) is a generalized attenuation function, and $\phi(t,f)$ is the minimum-phase spectrum associated with attenuation (Futterman, 1962). If a=1/Q(t), the exponential attenuation becomes the constant Q model of attenuation (Kjartannson, 1979). The magnitude of Equation (3.1) can be taken to obtain a relationship between the amplitudes of each component:

$$|S(t,f)| = |R(t,f)||M(t,f)||W(f)|e^{-\pi a(t,f)ft}. \qquad (3.2)$$

Note that if the time dependence of Equation (3.2) vanishes, then the stationary convolutional model, Equation (1.22), results. Thus the nonstationary convolutional model can be considered 'locally' stationary.

The |TVS| of the physical forward operator can be inferred from Equation (3.2). The physical forward operator is called the propagating wavelet and it acts on the reflectivity. Its nonstationary amplitude spectrum, $|W_p(t,f)|$, can be modeled as

$$|W_p(t,f)| = |M(t,f)||W(f)|e^{-\pi\alpha(t,f)ft}. \qquad (3.3)$$

$|W_p(t,f)|$ gives the Fourier amplitude spectrum of the propagating wavelet for a fixed time, t. The propagating wavelet contains the attenuation and source effects and it physically

represents a wavelet propagating through a 1-D earth, attenuating with time, and accumulating a multiple train.

3.2.2 Assumptions associated with NSD

The assumptions that have been made to develop the nonstationary spectral model limit the NSD procedure. Assumptions regarding anelastic attenuation, minimum-phase attenuation and estimation, multiple effects and others will be discussed. These assumptions arise from the ill-posed nature of the deconvolution problem and are common in other deconvolution methods.

In practice any method will have difficulty isolating the effects of anelastic attenuation from the effects of other attenuative mechanisms, as discussed in Section 1.3. NSD, as presented in this thesis, is also unable to distinguish the effects of anelastic attenuation from other nonstationary attenuation effects.

The assumption that attenuation is minimum-phase is only valid for anelastic attenuation. Attenuation other than anelastic attenuation is not constrained to be minimum-phase. Therefore, if attenuation other than anelastic attenuation is present in the data, then the assumption of minimum phase is not necessarily valid. In addition, the minimum-phase computations in the NSD algorithm are handled with a digital Hilbert transform. Since minimum-phase attenuation is created in the earth through physical means, removal of this phase through digital means is incomplete (Ellender, 1986), as described in Section 1.8.

As with stationary deconvolution, NSD cannot correct for all multiple effects, although it can potentially handle a wider class of multiples. Stationary deconvolution is incapable of handling multiples that cause nonstationary attenuation effects, as discussed in Section 1.5. NSD may be able to remove these sorts of multiples more effectively because it has been designed to correct for nonstationary attenuation effects. As described in Sections 1.3 and 1.5, one method whereby multiples cause nonstationary attenuation is intrabed multiples that originate within the deconvolution design zone. However, the issue of NSD's effectiveness in multiple removal is not investigated in this thesis. All data presented in this thesis is assumed to be multiple-free.

There are also several other assumptions. One-dimensional wave propagation is assumed and therefore spherical divergence corrections must be applied prior to NSD. It has been assumed that the attenuation depends only on traveltime and not raypath geometry. It is also assumed that the reflectivity, R(t,f) is random and therefore white in f. This assumption can be circumvented if well control is available.

3.3 Operator design and application

3.3.1 Overview

A nonstationary operator, designed directly from the input data, containing the source signature as well as undesirable characteristics related to anelastic attenuation is desired. This operator will be called the forward operator. The nonstationary forward operator will be estimated in a manner similar to the estimation of a stationary

deconvolution operator in stationary Fourier domain deconvolution (described in Section 1.9.1). It is assumed in both methods that the reflectivity effects can be removed from the power spectrum of the input trace through smoothing and that the smoothed power spectrum will be an estimate of the forward operator. In NSD, the nonstationary power spectrum, ($|TVS|^2$) will be smoothed instead of the stationary power spectrum.

Two methods of smoothing have been investigated for NSD. The first method, called the simple-smoothing method, smoothes the $|TVS|^2$ of the gained input trace directly. The second method, the residual-smoothing method, removes an approximate attenuation/gain surface from the $|TVS|$ of the gained input trace, squares the result and smoothes the resulting residual power spectrum. The approximate attenuation/gain surface is restored to the square root of the residual power spectrum (the amplitude spectrum) after smoothing. As with stationary deconvolution techniques, both smoothing methods will imperfectly remove reflectivity effects and bias the amplitude spectrum of the embedded wavelet, although the bias should be lessened in the residual-smoothing method. It is unclear what the smoothing does to $|M(t,f)|$.

After smoothing, the forward operator can be left as zero phase or coupled with a minimum-phase spectrum, which seems reasonable as the earth is expected to have minimum-phase attenuative processes. The forward operator is then inverted and applied to the data using nonstationary filter theory (as described in Section 2.2).

Examples will be shown where applicable, of the different stages in the operator design. The examples were created from a synthetic input trace. The synthetic trace was calculated by applying a Q filter (Q=50) combined with a minimum-phase 'source' wavelet to a reflectivity series. In the grey-level plots of the |TVS|, grey represents small positive numbers and black represents large positive numbers.

3.3.2 Gain of input trace

The first step of the NSD algorithm is to apply an approximate and deterministic exponential gain to the input trace. This is done to reduce aliasing of the steep decay surface of the input trace when it is windowed during the calculation of the |TVS|. As described in Section 2.3, the |TVS| window increment determines the time sample rate. A single row of the |TVS| represents a sample in time. |TVS| 3.1a was created from the synthetic trace with a large window increment and is therefore coarsely sampled in time. |TVS| 3.1a is composed of fewer rows and cannot adapt well to the exponential decay in time. |TVS| 3.1b has been created with a small window increment and is sampled more finely in time. |TVS| 3.1b has many rows and the exponential time decay is more clearly represented in the time-frequency matrix.

If an exponential decay surface is sampled too coarsely in time via the window increment, it will be aliased and not accurately represented in the resulting |TVS|. Sampling finely in time (with a small window increment) reduces the amount of aliasing,

however it increases the run time of the |TVS| calculation because each row in the |TVS| matrix requires an integration of Equation (2.8).

Figure 3.2 shows an exponential decay curve in time (3.2a) and its Fourier spectrum (3.2b). The Nyquist frequency as given by Equation (1.28) must be larger than all frequencies contributing significantly to the exponential surface or severe aliasing occurs and the |TVS| does not properly represent the signal. If the Nyquist frequency is chosen to be 100 Hz, then a sample rate, of 5ms is required in the |TVS| calculation. A trace with 2002 samples, will require 400 integrations of Equation (2.8) and the resulting |TVS| will have 400 rows. However, if the decay curve is gained (as in Figure 3.2c), the Nyquist frequency chosen from its spectrum (3.2d), can be smaller. In this example, the Nyquist frequency could be chosen to be considerably less than 25 Hz and the sample rate of the |TVS| will be equal to or greater than 0.2s. The |TVS| calculation time for the gained signal (3.2c) will be much faster and the matrix of the |TVS| will be smaller.

Therefore, by gaining the input trace to NSD (and reducing the exponential decay) the sample rate can be coarser and the aliasing of the |TVS| will be less severe. In the case of NSD, the input trace has exponential decay in both time and frequency. Therefore exponential gain will only produce a flat gained curve like 3.2c at one frequency. Other frequencies are under-corrected or over-corrected. Exponential gain of the input trace is a computational convenience and allows the |TVS| to be sparsely sampled in time.

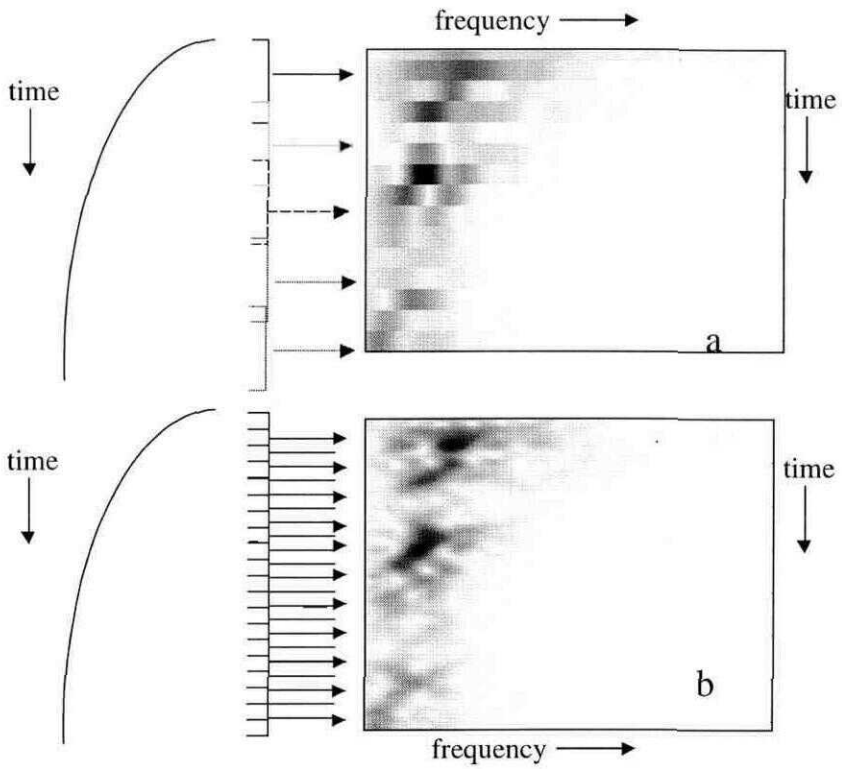

Figure 3.1: The window increment of the |TVS| calculation determines the time sample rate of the |TVS|. |TVS| 3.1a was created with a large window increment from a synthetic trace. As a result, |TVS| 3.1a is very coarsely sampled in time. In contrast, |TVS| 3.1b has been calculated with a small window increment is sampled more finely in time.

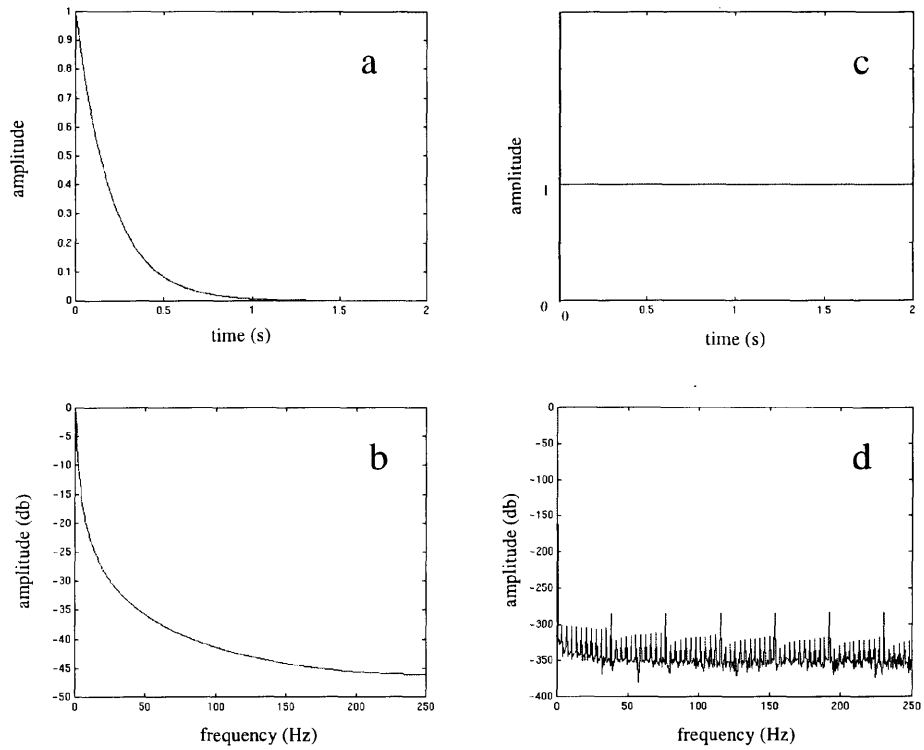

Figure 3.2: A steep exponential decay curve (3.2a) is shown with its Fourier spectrum (3.2b). The curve has been gained (3.2c) and the spectrum of the gained curve is shown in (3.2d).

3.3.3 Calculation of |TVS|

After gain has been applied to the input trace, its |TVS| is calculated. This |TVS| will be processed to form the NSD operator. Values for the window length and window increment must be chosen for the |TVS| calculation. Window length is related to the resolution of the |TVS| as described in Section 2.3.1 and window increment is related to

the time sample rate of the |TVS| as described in Section 3.3.2. These parameters are important because they influence the shape of the |TVS| and the resulting NSD operator. The effects of variations in these parameters, will be discussed in Chapter 4.

A model for the |TVS| of the gained input trace, |S(t,f)|, follows from Equation (3.2) (assuming constant-Q attenuation) as

$$| S(t,f) | = | R(t,f) || M(t,f) || W(f) | e^{-\pi ft/Q+\lambda t}, \qquad (3.4)$$

where λ is an exponential gain constant. The nonstationary power spectrum of the gained input trace, $|S(t,f)|^2$, is calculated by squaring Equation (3.4)

$$| S(t,f) |^2 = | R(t,f) |^2 | M(t,f) |^2 | W(f) |^2 \; e^{-2\pi ft/Q+2\lambda t}. \qquad (3.5)$$

Figure 3.3 shows the |TVS| of a synthetic input trace, (3.3a) created by applying a Q filter of Q=50, together with a minimum-phase wavelet, to a reflectivity time series. Also shown are the spectra of the other elements of Equation (3.4) that make up the input trace (ignoring multiple effects). The exponential Q decay in both time and frequency (3.3b) is prominent in the |TVS| of the ungained input trace (3.3a). The source waveform (3.3c) contributes the original bandwidth in the |TVS| of the input trace (at time 0) and the reflectivity (3.3d) adds the detailed character. The |TVS| of the gained trace (3.3e) is created by applying an exponential gain to the input trace and recomputing its |TVS|.

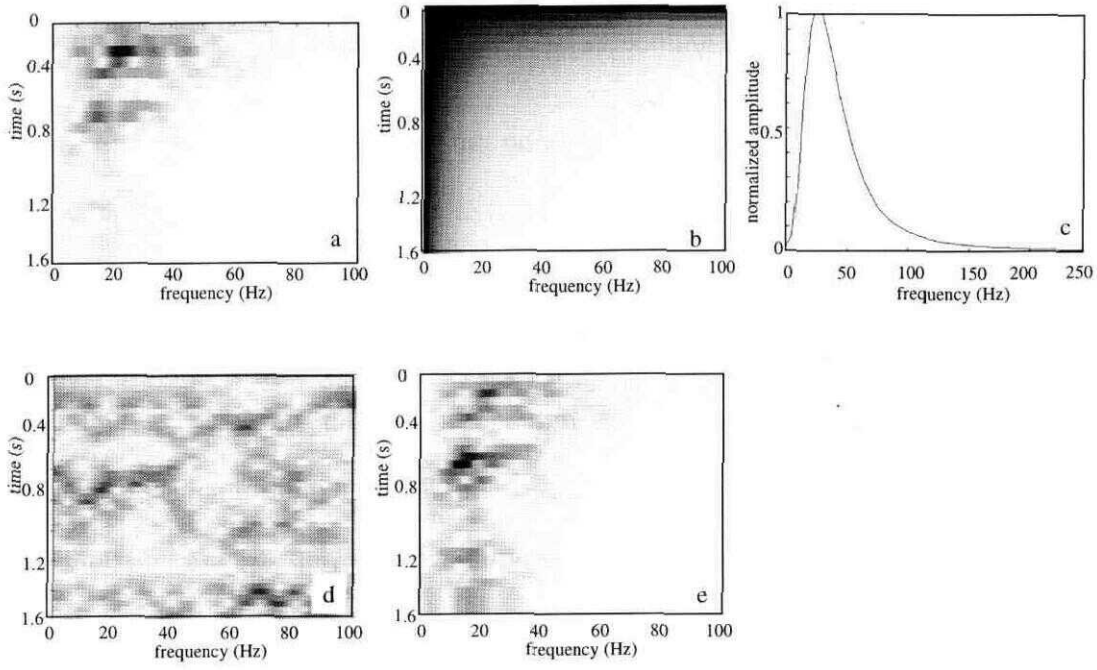

Figure 3.3: The |TVS| of an ungained synthetic input trace to NSD (3.3a), Q surface (Q=50) (3.3b), stationary source spectrum (3.3c) and bandlimited reflectivity (3.3d). The |TVS| of the gained trace is shown as 3.3e.

3.3.4 Smoothing

The next step in the NSD process is to attempt to separate the reflectivity from the source waveform and attenuation. The nonstationary power spectrum of the gained input trace ($|S(t,f)|^2$) is smoothed two-dimensionally (in time and frequency). This is consistent with Fourier domain deconvolution, where it is assumed that the general trend of the power spectrum is due to the source signature and the detail in the power spectrum is from the reflectivity, as described in Section 1.9.1. In stationary deconvolution the power

spectrum is smoothed one-dimensionally (in frequency) in an attempt to remove the reflectivity, however in NSD two-dimensional smoothing is required.

Two options of smoothing the nonstationary power spectrum in an attempt to eliminate the reflectivity have been examined. These are the simple-smoothing method and the residual-smoothing method. In the simple-smoothing method, $|S(t,f)|^2$, as described by Equation (3.5) (multiple effects set to unity), is smoothed directly. The smoothing is achieved through a one-dimensional convolution of $|S(t,f)|^2$ with a normalized, suitable smoother in time and then again in frequency. The order of smoothing does not matter, as convolution is commutative. The smoothed nonstationary power spectrum of the gained input trace, $\overline{|S(t,f)|^2}$, can be represented by

$$\overline{|S(t,f)|^2} = \left[|R(t,f)|^2 |W(f)|^2 \, e^{-2\pi ft/Q + 2\lambda t} \right] * a(f) * b(t), \qquad (3.6)$$

where * represents convolution, a(f) is a frequency smoother and b(t) is a time smoother. The lengths of the time and frequency smoothers can be specified individually. A comparison of different smoother geometries and discussion regarding optimal smoother lengths is contained in Chapter 4.

The smoothers in the simple-smoothing method of Equation (3.6) act on the reflectivity, multiples (if present), source signature and exponential attenuation and gain surface. Smoothing these other components as well as the reflectivity biases the estimate of the forward operator. A bias is a systematic error. For instance, in NSD the spectrum of the input trace is smoothed in an attempt to estimate the spectrum of the source

wavelet. If the spectrum of the source wavelet is the input to a reflectivity suppression process an unbiased process would not change it. A smoothing process, however, changes the spectrum even though it is the desired output and therefore the process and output are referred to as biased.

The smoothing process of Equation (3.6) approximately removes the reflectivity and it follows by assumption that

$$\overline{|S(t,f)|^2} \approx |W(f)|^2 \, e^{-2\pi ft/Q+2\lambda t}. \tag{3.7}$$

Next, the square root of Equation (3.7) is calculated and a constant, n_w, is added for stability during the operator inversion. This constant is calculated by multiplying the maximum of $|W(f)|e^{-\pi ft/Q+\lambda t}$ by a small number, called the stability factor. The resulting amplitude spectrum, $\overline{|F(t,f)|}$, is estimate of the multiple-free forward operator with gain applied (compare to Equation (3.3))

$$\overline{|F(t,f)|} \approx |W(f)|e^{-\pi ft/Q+\lambda t} + n_w. \tag{3.8}$$

The propagating wavelet is the physical forward operator. It contains the source waveform and attenuation effects, essentially Equation (3.8) with the exponential gain removed:

$$\overline{|W_p(t,f)|} \approx |W(f)|\, e^{-\pi f t/Q} \tag{3.9}$$

Figure 3.4 shows a propagating wavelet from the simple-smoothing method at two different color scales. In 3.4a, white represents zero and black is large positive numbers. In 3.4b, grey is zero and black is large positive numbers. In this example, the features of the propagating wavelet are easier to see in Figure 3.4b, and Figure 3.4a has been included because it uses the same color scale as the other figures of |TVS| in this thesis. The propagating wavelet decays in both time and frequency and the decay appears to have a generally exponential shape. The |TVS| of the propagating wavelet is not completely smooth and still contains some of the reflectivity character.

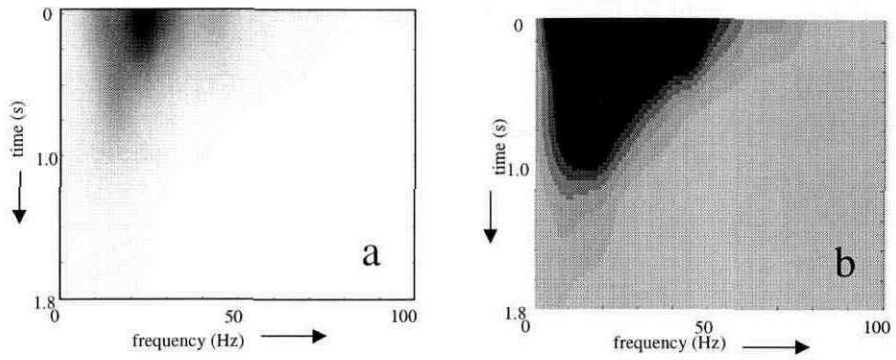

Figure 3.4: Both |TVS| are the propagating wavelet from the simple-smoothing method. In Figure 3.4a, white is zero and black is large positive numbers, and 3.4b, grey is zero and black is large positive numbers. Figure 3.4a has been included for comparison to other |TVS| in this thesis and 3.4b is included because it shows the detail in the propagating wavelet more clearly. The propagating wavelet approximates the source waveform and attenuation effects but is also biased by the smoothing of the attenuation surface.

The second method of smoothing is called the residual-smoothing method. In this method, the steep Q/gain surface is removed from the |TVS| of the gained input trace before smoothing to reduce the bias of the operator. An estimate of Q is required for this type of smoothing.

Constant-Q attenuation can be modeled as an exponential surface in frequency and time whose shape is determined by the quality factor, Q (assumed to be constant in frequency and slowly time-variant). Figure 3.3b shows a Q surface for Q=50. Assuming

that an estimate of Q, $\hat{Q}$, is available, and setting |M(t,f)| to unity (to ignore multiple effects), the attenuation/gain surface can be removed approximately from |S(t,f)| of Equation (3.4) to produce a residual amplitude spectrum, $|\rho(t,f)|$,

$$|\rho(t,f)| = \frac{|R(t,f)||W(f)|e^{-\pi ft/Q+\lambda t}}{e^{-\pi ft/\hat{Q}+\lambda t}+n_Q}, \tag{3.10}$$

where n_Q is the maximum of the exponential decay/gain surface multiplied by a small constant. The constant, n_Q, is added to increase stability in the division caused by lack of numerical precision. The constant is typically small, between $1x10^{-4}$ and $1x10^{-6}$.

Equation (3.10) can be written approximately as

$$|\rho(t,f)| \approx |R(t,f)||W(f)|. \tag{3.11}$$

The residual amplitude spectrum, |ρ(t,f)|, is mostly free from attenuation effects and is dominated by the amplitude spectra of the source signature and reflectivity. This residual amplitude spectrum is squared to form a power spectrum and then smoothed two-dimensionally with time and frequency smoothers to remove the reflectivity and estimate |W(f)|.

$$\overline{|\rho(t,f)|}^2 \approx |R(t,f)|^2|W(f)|^2 * a(f) * b(t), \tag{3.12}$$

where $\overline{|\rho(t,f)|}^2$ is the residual power spectrum after smoothing, * denotes convolution, a(f) is the frequency smoother and b(t) is the time smoother. The smoothers may be

different from the smoothers in the simple-smoothing method. The determination of optimal smoother lengths requires parameter testing and judgement and will be discussed in Chapter 4.

By removing the Q/gain surface, the reflectivity effects can be suppressed in the |TVS| while reducing the bias from smoothing. Therefore, by assumption, the amplitude spectrum of the smoothed residual can be written as

$$\overline{|\rho(t,f)|} \approx |W(f)|. \qquad (3.13)$$

From Equation (3.13) it can be seen that $\overline{|\rho(t,f)|}$ is an estimate of the stationary source amplitude spectrum and it is shown in Figure 3.5. Figure 3.6 shows the amplitude spectrum of the known source signature of the synthetic input trace (3.6a) superimposed with two rows of $\overline{|\rho(t,f)|}$, one at 0.4s (3.6b) and the other at 1.6s (3.6c). These rows are shown as black lines on Figure 3.5.

Figures 3.5 and 3.6 show that the smoothing process is imperfect. Some reflectivity effects remain and $\overline{|\rho(t,f)|}$ is not stationary. Figure 3.5 can be compared to the |TVS| of the bandlimited reflectivity of Figure 3.3d. The high amplitude area at early times is from the reflectivity that has not been completely suppressed. The smoothing process in both the residual and simple-smoothing methods is limited by the use of finite length smoothers. Smoothers of infinite length would perfectly remove reflectivity.

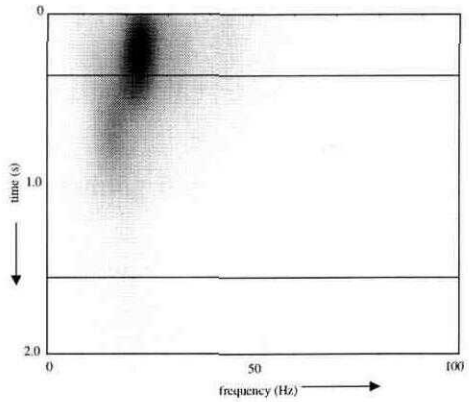

Figure 3.5: The residual amplitude spectrum after smoothing in time and frequency from the residual-smoothing method. Each row in the |TVS| is an approximation of the amplitude spectrum of the stationary source waveform. The black lines show the rows have been used for comparison in Figure 3.6.

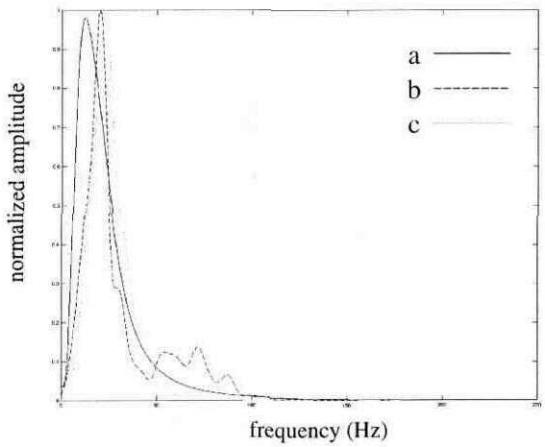

Figure 3.6: A comparison of the amplitude spectrum of the source waveform (a) and its estimation from the residual-smoothing method. The estimated amplitude spectrum of

the source waveform is a row of the |TVS| of the residual amplitude spectrum after smoothing (Figure 3.5) at 1.6s (b) and 0.4s (c).

After the residual-smoothing process, the attenuation/gain surface is restored to $\overline{|\rho(t,f)|}$. This yields an estimate of the amplitude spectrum of the gained forward operator, |F(t,f)|:

$$|F(t,f)| \approx |\overline{\rho(t,f)}|\, e^{-\pi f t/Q+\lambda t} + n_w, \qquad (3.14)$$

where n_w is a constant added for stability in the inversion of Equation (3.18). The constant, n_w, is determined by multiplying the maximum of $|\rho(t,f)|\, e^{-\pi f t/Q+\lambda t}$ by a small number, typically between 10^{-1} and 10^{-6}. The quantity, $|\rho(t,f)|\, e^{-\pi f t/Q+\lambda t}$, will contain noise if it has been calculated from real data. The constant is added to prevent noise in areas of low signal strength from dominating |F(t,f)| after the inversion and influencing the phase as discussed in Section 1.8.

As in the simple-smoothing method, the physical forward operator is called the propagating wavelet and it contains the source waveform and attenuation effects,

$$|W_p(t,f)| \approx |\overline{\rho(t,f)}|\, e^{-\pi f t/Q} \qquad (3.15)$$

The propagating wavelet differs from the forward operator in that it does not have exponential gain.

In Figure 3.7 the propagating wavelet from the residual-smoothing method (3.7a and 3.7c) is compared to the theoretical propagating wavelet (3.7b and 3.7d) computed from the source waveform and the exponential decay surface. The two |TVS| are shown at two different grey scales. In 3.7a and 3.7b, white corresponds to zero and black is large positive numbers. These two plots can be compared to other |TVS| in the thesis. Figures 3.7c and 3.7d show more detail. In these figures, grey corresponds to zero and black is large positive numbers. The propagating wavelet from residual-smoothing is generally smooth, although it still contains some features associated with reflectivity. In addition, the propagating wavelet has the characteristic exponential decay in both time and frequency of Q attenuation.

The propagating wavelet from residual-smoothing can also be compared to the propagating wavelet from simple-smoothing, Figure 3.4. The result from residual-smoothing (3.7a and 3.7c) is visually more similar to the theoretical result (3.7b and 3.7d) than the result from simple-smoothing (in Figure 3.4a and 3.4b). The propagating wavelet from residual-smoothing shows stronger exponential decay at early times (approximately 0 to 0.5s). In addition, the high amplitude (black) areas on both propagating wavelets seem shifted to a higher frequency relative to the theoretical result. This may be a result of the smoothing. This indicates that the residual-smoothing method may provide a more appropriate forward operator than the simple-smoothing method.

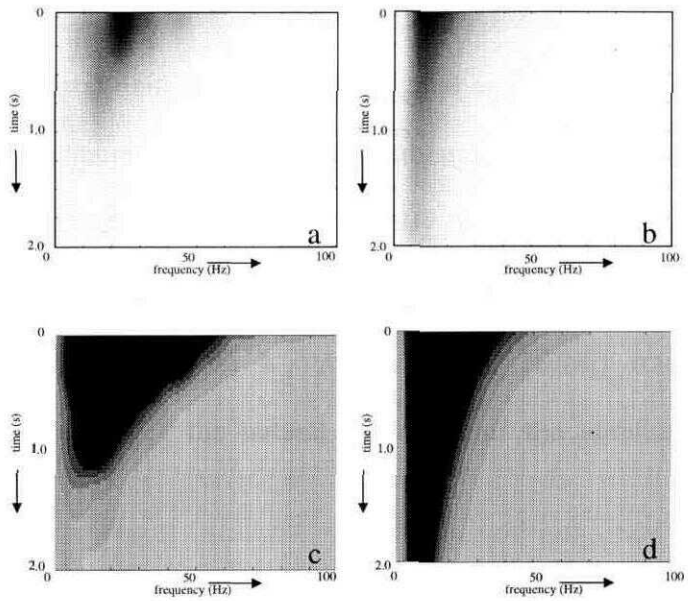

Figure 3.7: The propagating wavelet (3.7a and 3.7c) from the residual-smoothing method and the theoretical propagating wavelet (3.7b and 3.7d) calculated from the source signature and decay/gain exponential. Both propagating wavelets are shown at two different greyscales. In Figures 3.7a and 3.7b, white is zero and black is large positive numbers. In Figures 3.7c and 3.7d, grey is zero and black is large positive numbers. Figures 3.7c and 3.7d have been added because they show more detail. The |TVS| of the propagating wavelet approximates the source waveform and the anelastic attenuation. This figure can be compared to Figure 3.4, the propagating wavelet from the simple-smoothing method.

3.3.5 Phase computation, inversion, and application of the operator

The operator from either smoothing method may be left as zero phase or combined with a minimum-phase spectrum. Although each row of the 'zero-phase' operator is zero phase, such operators will generally change both the amplitude and the phase of a trace when applied through Equation (2.6) (Margrave, 1998). The minimum-phase spectrum is calculated with a one-dimensional Hilbert transform, H, over frequency at constant time of the natural logarithm of the amplitude spectrum, as described in Section 1.8:

$$\phi(t,f) = H[\ln |F(t,f)|], \tag{3.16}$$

From Equations (3.14) and (3.8), it can be seen that the forward operator contains a small constant to prevent the logarithm in Equation (3.16) from becoming unstable. The operation of Equation (3.16) is performed on each row of the time-variant amplitude spectrum to create a time-variant minimum-phase spectrum. The amplitude spectrum, $|F(t,f)|$ of Equations (3.14) and (3.8), and the phase spectrum, $\phi(t,f)$, of Equation (3.15) can be combined to produce the complex-valued forward operator, F(t,f)

$$F(t,f) = |F(t,f)| e^{i\phi(t,f)}. \tag{3.17}$$

To complete the process, the forward operator, F(t,f), is inverted and applied to the trace using nonstationary filter theory (Margrave, 1998) as described in Equation (2.6). In this manner, the time-variant operator is applied continuously to the input trace

and windowing is avoided in the operator application. The spectrum of the reflectivity estimate, R(f), is given by

$$R(f) = \int s(t)F^{-1}(t,f)e^{-2\pi itf}\,dt \quad , \tag{3.18}$$

where s(t) is the input trace and $F^{-1}(t,f)$ is the inverse operator that is the simple algebraic inverse of F(t,f). The forward and inverse operators are related for all t and f by

$$F(t,f)F^{-1}(t,f)=1 \tag{3.19}$$

An inverse Fourier transform is applied to R(f) to obtain the reflectivity estimate in the time domain.

The success of the inversion in NSD is partly limited by numerical precision. Lack of numerical precision causes amplitude distortion of the most severely attenuated frequencies. These amplitude distortions are magnified by inversion and are manifested as noise in the final result from NSD. The bandwidth of R(f) must be limited by applying a bandpass filter after NSD to suppress frequencies affected by this lack of numerical precision. The bandpass filter should be chosen to encompass frequencies that may be contained in the spectrum of the source waveform and suppress all frequencies greater than Nyquist frequency.

In real data, noise may dominate the signal where it is severely attenuated, such as at high frequencies. This noise may be magnified during the phase computation or operator inversion, if insufficient amounts of white noise, n_w, have been added.

3.4 Further extensions of NSD

3.4.1 Introduction

Modifications have been made to the original trace-by-trace version of NSD in an effort to improve efficiency and allow more flexibility. Two different extensions of NSD are explored, profile-mode NSD and profile-mode NSD with random windows (fx-NSD). Profile-mode NSD allows a single operator to be applied to an ensemble of traces. Profile-mode NSD with random windows (fx-NSD) also allows a single operator to be applied to an ensemble of traces. However, it allows the window length to fluctuate randomly when creating the |TVS| of the input ensemble. Examples of the extensions of NSD will be shown in Chapter 5.

As described in Section 3.3, NSD designs and applies an operator separately for each trace. This trace-by-trace version of NSD is slow. Approximately 80% of the run-time is spent designing the operator and 20% is spent applying it. The following chart breaks down the run-time of minimum-phase residual-smoothing NSD approximately.

Table 3.1: Breakdown of trace-by-trace minimum-phase residual-smoothing NSD run-time

Operator design:		**80%**
	build initial |TVS|	10%
	residual smoothing	45%
	inversion of operator and phase computation	20%
	miscellaneous	5%
Operator application		**20%**
Total		**100%**

3.4.2 Profile-mode NSD

The first extension of NSD, profile-mode NSD, designs a single operator and applies it to an entire ensemble of traces. This option is designed to increase the efficiency of the algorithm and minimize trace to trace changes induced by the operator. In addition, a physical model of the data may indicate that a single operator is more appropriate for an entire ensemble. For example, a surface-consistent approach may require that a single operator be applied to an entire CMP gather.

The operator in profile-mode NSD is created by calculating a |TVS| for each trace in the ensemble and averaging them to produce a single |TVS|. This resulting |TVS| is processed as the |TVS| of any input trace is processed in trace-by-trace NSD. Specifically, the average |TVS| is smoothed (with either simple-smoothing or residual-smoothing), coupled with a minimum-phase spectrum if desired, and inverted to form the NSD operator. However in the profile-mode approach, the single NSD operator (created from the average |TVS|) is applied to each trace in the ensemble. Profile-mode

deconvolution is a great advantage in that approximately 65% of the computation time of trace-by-trace NSD would only be performed once for an ensemble of traces.

3.4.3 Profile-mode NSD with random windows (fx-NSD)

The second extension of NSD is also a profile-mode approach. However, it has an option which allows the length of the window, used to calculate the |TVS|, to fluctuate randomly with each trace while remaining centered on a particular time. In this extension of NSD, one row of the average |TVS| is calculated at time. A temporal window of randomly fluctuating length is applied to each trace in the ensemble. Then the TVS of each windowed segment of the ensemble is calculated. This process of windowing and calculating the TVS is represented by

$$\Phi(x,t,f) = \int_{t\,min}^{t\,max} \Psi(x,t')w(x,t-t')e^{-2\pi ift'}dt', \qquad (3.17)$$

where $\Psi(x,t')$ is the ensemble of traces, $w(x,t-t')$ is the ensemble of randomly varying windows and tmin and tmax are the start and end times of the temporal windows. The complex-valued matrix, $\Phi(x,t,f)$, is called the f-x spectra (Margrave, in press). Random windows are used because a summation over x is expected to reduce window artifacts as they will be incoherent.

Next, the magnitude of the f-x spectra is calculated to produce the amplitude spectra. The amplitude spectra are averaged to produce a row, at time t, in the average |TVSA(t,f)|:

$$|\,TVSA(t,f)\,| = \frac{1}{N}\int |\Phi(x,t,f)|dx\,, \tag{3.18}$$

where N is the number of traces in the ensemble. This procedure of calculating the f-x spectra and averaging is repeated for each row until |TVSA(t,f)| is filled.

CHAPTER 4: PARAMETER TESTING

4.1 Introduction

There are many parameters in NSD and testing must be performed to determine the relationship between parameter choice and the result from NSD. The parameters may be related to |TVS|, such as the window length, window increment, and trace padding for the Fourier transform. Other parameters are more general, such as the exponential gain constant applied to the input trace and the stabilization factor. Some parameters, such as the length and geometry of the time and frequency smoothers, method of smoothing, and the estimate of Q are directly related to operator design. Finally, the phase of the operator and the filter specifications for filtering the output trace must be chosen.

In this chapter, all tests will be performed on a multiple-free, synthetic input trace. The synthetic trace is noise-free unless specified otherwise. It was created by applying a Q filter (Q=50) combined with a minimum-phase wavelet, of dominant frequency 15 Hz, to a reflectivity series. The synthetic has analog (theoretical) minimum-phase so results from NSD are generally expected to have residual delay. As explained in Section 1.8, digital minimum-phase estimates calculated with a digital Hilbert transform are imperfect. Therefore a phase correction based on these estimates will not completely remove time shifts due to velocity dispersion.

As explained in Section 3.3, the result from NSD must be bandpass filtered to reduce noise that arises from the lack of numerical precision. A bandpass filter of 10-60

Hz has been applied to all output traces from NSD in the examples of this chapter. The Nyquist frequency, 250 Hz in these examples, is greater than the high frequency cutoff of the bandpass filter so aliased frequencies are removed by the filter.

There are many different parameters to test in the NSD algorithm. Not all permutations can be included in this thesis. Successive testing has favored the minimum-phase residual-smoothing version of NSD and therefore all testing, unless otherwise specified, will be performed on this version of NSD. Each parameter test suggests an optimal parameter. The testing process is iterative, and the best parameters from previous tests will be used in subsequent tests. These optimal parameters have been used in all of the tests. The parameter tests include testing the sensitivity of NSD to:

1. time and frequency smoother lengths (minimum-phase simple-smoothing)

2. time and frequency smoother lengths (minimum-phase residual-smoothing)

3. smoother geometry (minimum-phase simple and residual-smoothing)

4. errors in the estimate of Q

5. window length in the calculation of the |TVS| of the input trace

6. window increment in the calculation of the |TVS| of the input trace

7. exponential gain constant applied to the input trace

In addition, the following comparisons and tests will be made:

8. comparison of combination of Wiener deconvolution and gain, and time-variant spectral whitening to minimum-phase simple and residual-smoothing NSD, and zero-phase simple and residual-smoothing NSD

9. comparison of bandlimited reflectivity with constant phase rotations to the result from minimum-phase residual-smoothing

10. effects of finite numerical precision on NSD

The results from each parameter test are compared to the bandlimited, input trace, and their |TVS|. The reflectivity has been bandlimited to 10-60 Hz to provide a comparison to the results from NSD. To judge the performance of the parameters, compare the features in the trace and |TVS| of the bandlimited reflectivity to the other traces. In the time domain, such features as the peak at 0.25s and the trough at 0.8s can be used for comparison, as can be seen from Figure 4.2. It is best to compare the earlier times of the output traces with the bandlimited reflectivity. In the |TVS| there are several features, some of which are pointed out with arrows on Figure 4.3. There is a dark zone at 0.7s, a light zone at 1.0s, and a dark band starting at 1.2s. In the grey-level plots of the |TVS| black is a large positive number and white is zero. Therefore a white spectrum (high amplitudes at all frequencies) would appear black in a grey-level plot. The |TVS| grey level plots are normalized with respect to each other for easier comparison.

4.2 Length of time and frequency smoothers

The length of time and frequency smoothers affects the results significantly and there are several factors to consider before choosing a smoother length. The uncertainty principle, duration of reflectivity packages, method of smoothing and physical model must be considered as the smoothers are chosen. First, theoretical constraints regarding time and frequency smoothers will be outlined and then examples of how changing the smoother lengths affects a synthetic trace will be shown.

The relationship of the smoother lengths in the time and frequency domain must considered. The length of a smoother in one domain is inversely proportional to its length in the other domain, as stated by the uncertainty principle (Equation (2.9)). In addition, smoothing in the time domain becomes windowing in the frequency domain and vice versa. Therefore smoothing in the frequency domain with a long frequency smoother causes windowing in the time domain with a short window.

Smoothing the power spectrum is equivalent to windowing the autocorrelation function. A window is needed in the time domain that will encompass the majority of the embedded wavelet in the spectrogram. Since a typical wavelet is approximately 0.2s duration, the frequency-domain smoother would need to be at least 5 Hz to encompass it.

Smoothing is intended to suppress the reflectivity in the NSD operator. The earth's reflectivity manifests itself as banding in time on the |TVS|. Time smoothers must equalize the power of the |TVS| in time and therefore must be long enough to encompass

the bands of similar reflectivity character in order to remove the reflectivity from the |TVS|.

The two methods of smoothing, simple and residual, are different and may require different lengths of smoothers. The simple-smoothing method directly smoothes the nonstationary power spectrum of the gained input trace. Therefore long temporal smoothers are not desirable because they will distort the exponential decay surface. The residual-smoothing method smoothes the residual power spectrum. (which does not contain exponential decay), therefore long time smoothers will be less problematic. Theoretically, temporal smoothers of infinite length are needed to remove the reflectivity.

While testing one smoother the other must be held constant. The values of the smoother held constant have been chosen based on the considerations outlined above, as well as through an iterative testing process. The time smoother must be long enough to encompass the reflectivity packages in both smoothing methods. In the examples shown in this chapter, the reflectivity bands are approximately 0.2-0.4s in length, so the time smoother should fall somewhere beyond this range. From the above considerations, it can be seen that the frequency smoother is best kept fairly short in both the residual-smoothing and simple-smoothing methods, perhaps 5 to 10 Hz.

4.2.1 Frequency smoother lengths for simple-smoothing NSD

One way to evaluate frequency smoother lengths is to examine their effects in the time domain. The frequency-domain smoothing process is equivalent to windowing the

autocorrelation of the seismic trace. As mentioned previously, the length of the frequency smoother is inversely related to the duration of the window in the time domain. The autocorrelation of the wavelet and seismic trace are thought to be similar in shape at early lags and differing at later lags because the autocorrelation of the seismic trace will have reflectivity at later lags. Therefore the autocorrelation of the seismic trace must be windowed to approximate the autocorrelation of the wavelet. The window must be long enough to include the portion of the autocorrelation of the seismic trace that is similar to the autocorrelation of the wavelet but short enough to exclude the reflectivity. The autocorrelation of the input trace, and window lengths corresponding to several frequency smoothers of different lengths are shown in Figure 4.1. It can be seen from this figure that the window corresponding to $\Delta f=30$ (corresponding to line 4.1b) windows the autocorrelation prematurely. In this example, a window length corresponding to 4.1d or 4.1e may be more appropriate.

From Figures 4.2 and 4.3 it can be seen that the simple-smoothing method of NSD seems to perform slightly better when used with small frequency smoothers, such as 5 or 10 Hz. As explained previously, long frequency smoothers bias the exponential attenuation surface and distort the operator. There are subtle differences in the traces of Figure 4.2 and the |TVS| of Figure 4.3. An arrow on Figure 4.2 points out a zone, between 1.0 and 1.3s, in the output traces that is resolved better with the short frequency smoothers than the long frequency smoothers. The |TVS| corresponding to the long frequency smoothers (20 and 30 Hz) are lacking power at high frequencies and later

times. An arrow in Figure 4.3 points out a zone in the |TVS| corresponding to Δf=30 Hz, that is relatively unwhitened. Small frequency smoothers are favored for the minimum-phase simple-smoothing method based on reflectivity character of the output traces, whiteness of their |TVS| and theoretical reasons.

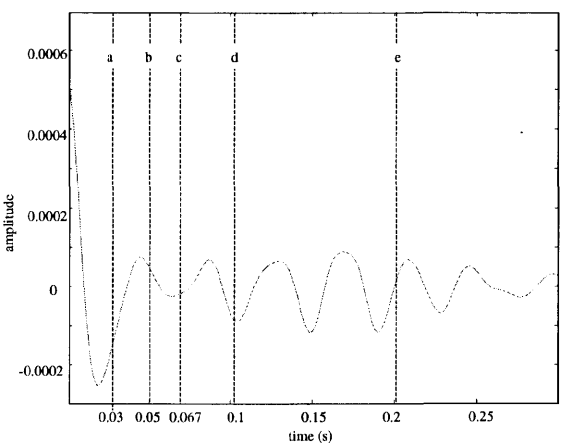

Figure 4.1: The autocorrelation of the input trace. The dashed lines indicate where the autocorrelation would be windowed for frequency smoothers of different lengths. The dashed line labeled 4.1a corresponds to 30 Hz, 4.1b corresponds to 20 Hz, 4.1c corresponds to 15 Hz, 4.1d to 10 Hz and 4.1e to 5 Hz.

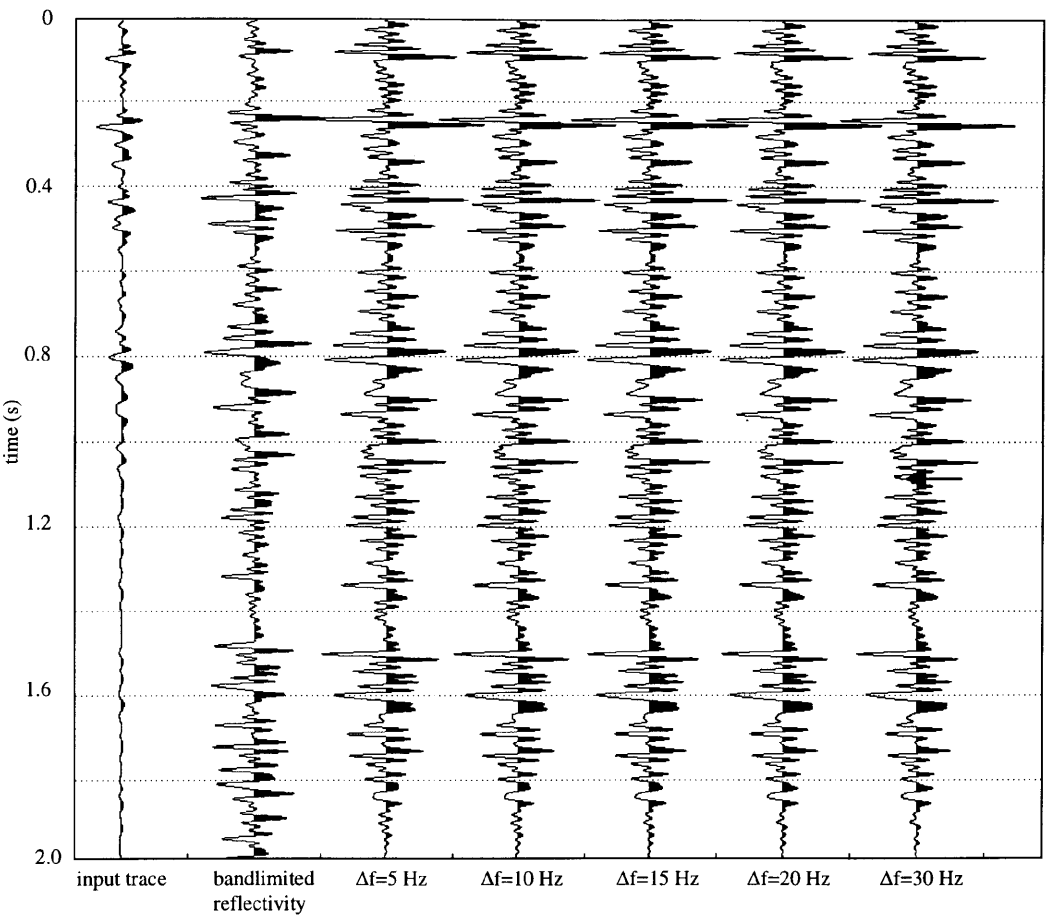

Figure 4.2: Test of the sensitivity of minimum-phase simple-smoothing version of NSD to frequency smoother length. The length of the time-smoother was held constant at 1.0s while the length of the frequency smoother, Δf, was changed from 5 to 30 Hz.

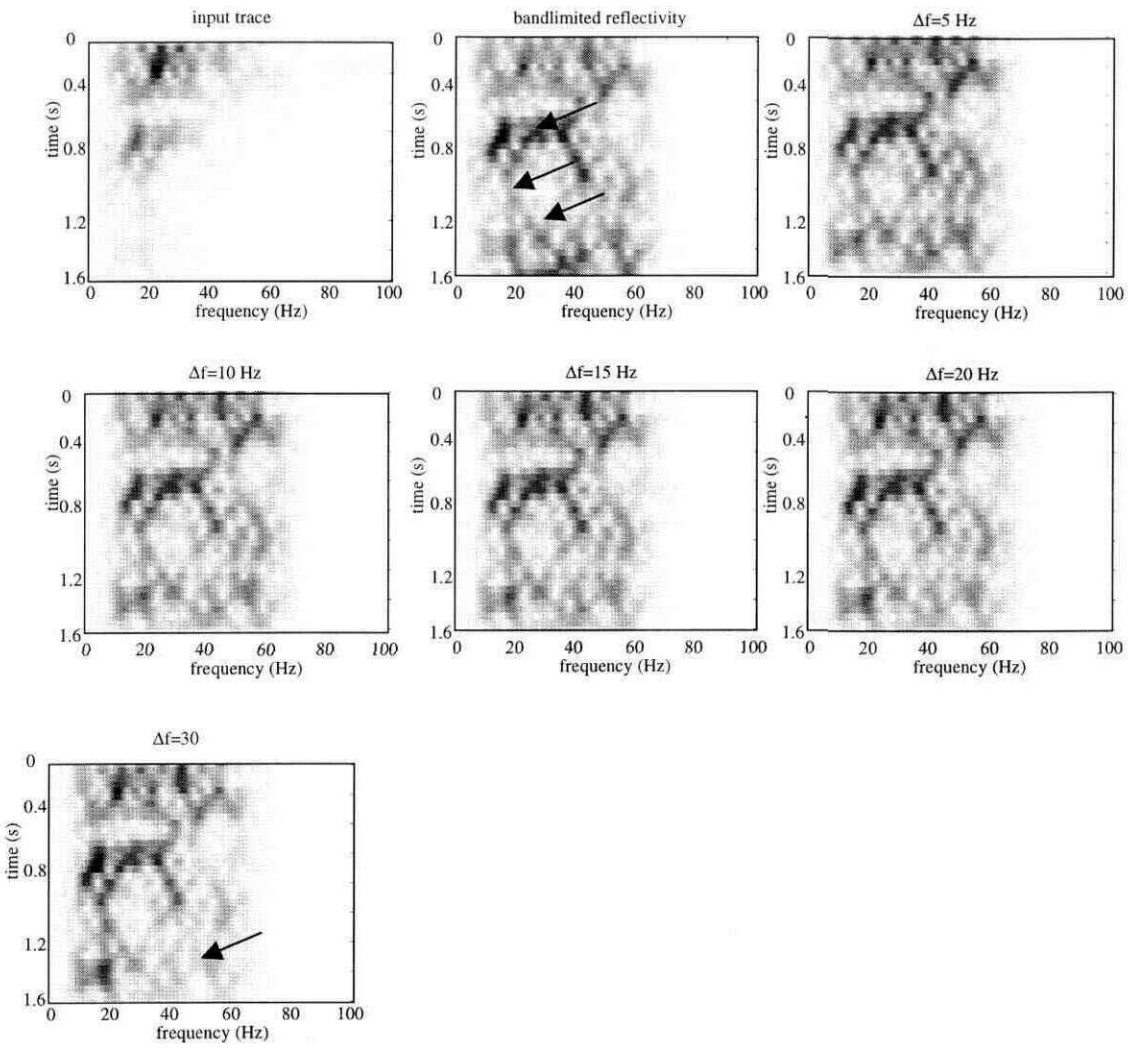

Figure 4.3: |TVS| of traces in Figure 4.2. The |TVS| of the resultant traces from the frequency-smoother tests of the minimum-phase simple-smoothing version of NSD. The time smoother was held at 1.0s while the frequency smoother was varied.

4.2.2 Time smoother lengths for simple-smoothing NSD

Figures 4.4 and 4.5 show the results of the time smoother tests for minimum-phase simple-smoothing NSD. Small time smoothers, such as 0.05 and 0.1s, seem to provide poor results. For example, the doublet trough just below 0.8s on the bandlimited reflectivity, pointed out by an arrow in Figure 4.4, is poorly represented on the traces corresponding to small time smoothers. These time smoothers are too small to span the reflectivity packages and remove them from the forward operator. Therefore reflectivity is removed from the output trace during the inversion. A reflectivity package is a time zone of similar reflectivity character, such as the zone of 1.2 to 1.5s on the bandlimited reflectivity.The |TVS| of the shortest time smoother is distorted, as can be seen in Figure 4.5. An arrow points to an area on this |TVS| that has more energy at early times and less energy at later times as compared to the |TVS| of the bandlimited reflectivity.

The reflectivity character between 0.7s and 1.1s, pointed out with arrows on Figure 4.4, is best reproduced by time smoothers of intermediate length, such as 0.5 to 1.0s. The |TVS| corrresponding to the longest time smoother, 1.5s, looks less whitened, as pointed out by arrows in Figure 4.5. The |TVS| corresponding to the 0.5s or 1.0s time smoother best resembles the |TVS| of the bandlimited reflectivity. Intermediate length time smoothers work best in the simple-smoothing method. The time smoothers must be long enough to remove the reflectivity, but not so long that they distort the |TVS|. In conclusion, intermediate length time smoother (of approximately 0.5s) is preferred for

minimum-phase simple-smoothing based on theoretical considerations, reflectivity character and the whiteness of the |TVS|.

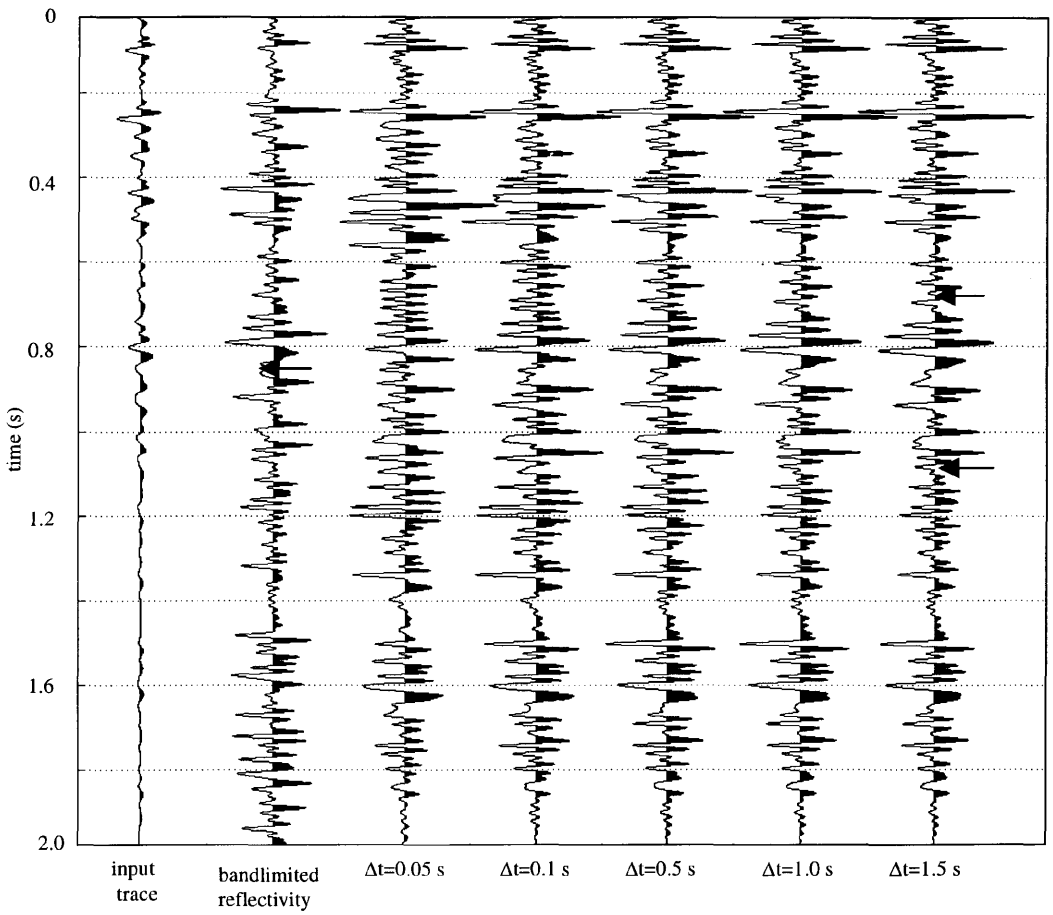

Figure 4.4: Test of the sensitivity of minimum-phase simple-smoothing version of NSD to the time smoother length. The length of the frequency-smoother was held constant at 10 Hz while the length of the time smoother, Δt, was changed from 0.05 to 1.5s.

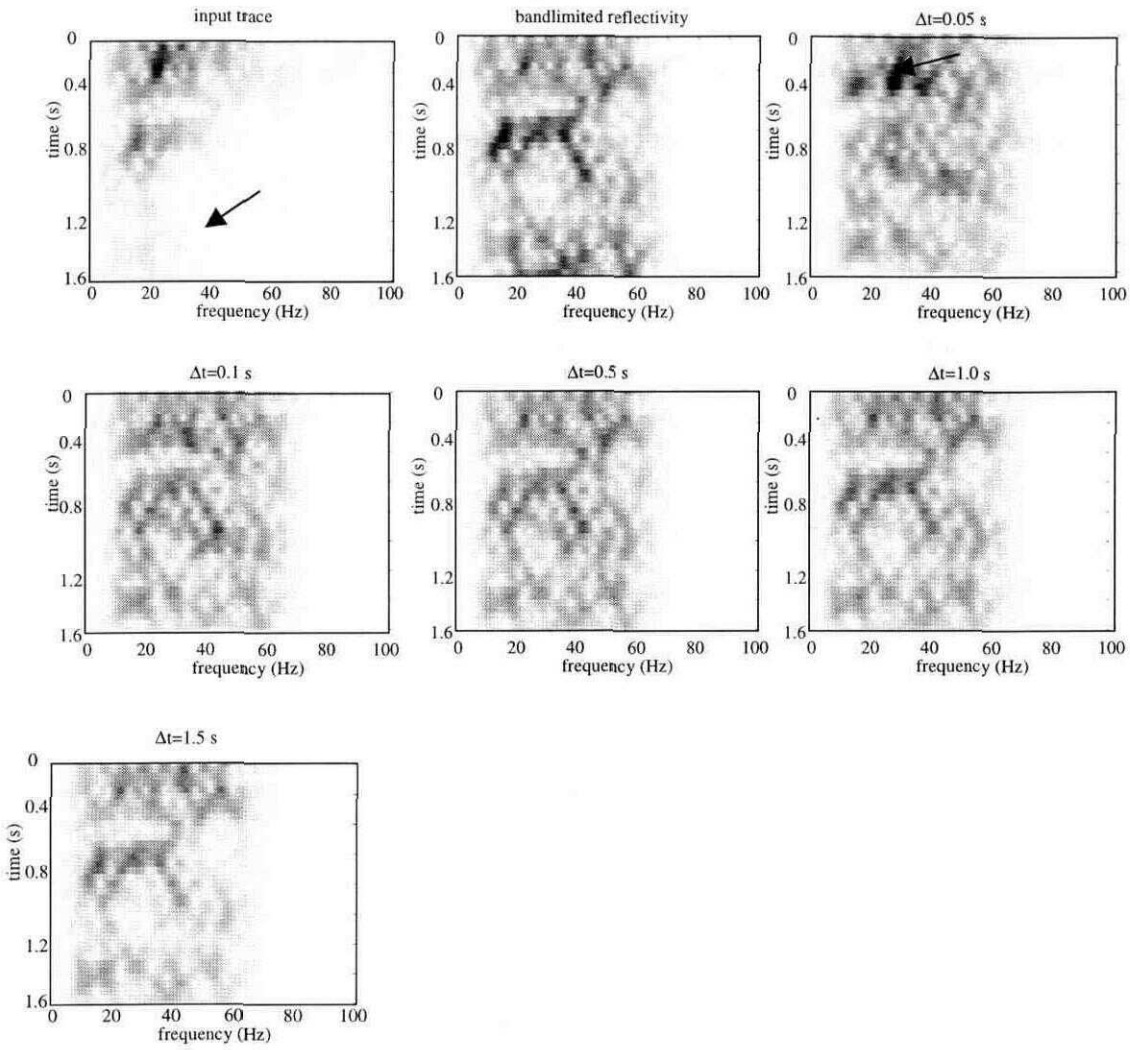

Figure 4.5: |TVS| of traces in Figure 4.4. The |TVS| of the resultant traces from the time-smoother tests of the minimum-phase simple-smoothing version of NSD. The length of the frequency smoother was held at 10 Hz while the length of the time smoother was varied.

4.2.3 Frequency smoother lengths for residual-smoothing NSD

The traces in Figure 4.6 and the |TVS| of Figure 4.7 show the results of the frequency smoother test from minimum-phase residual-smoothing NSD. The reflectivity of the traces corresponding to the small frequency smoothers seems to match the bandlimited reflectivity better. There seems to be little difference in the output traces using smoothers of different lengths. The 10 Hz frequency smoother is favored in this example of the residual smoothing method based on theoretical considerations.

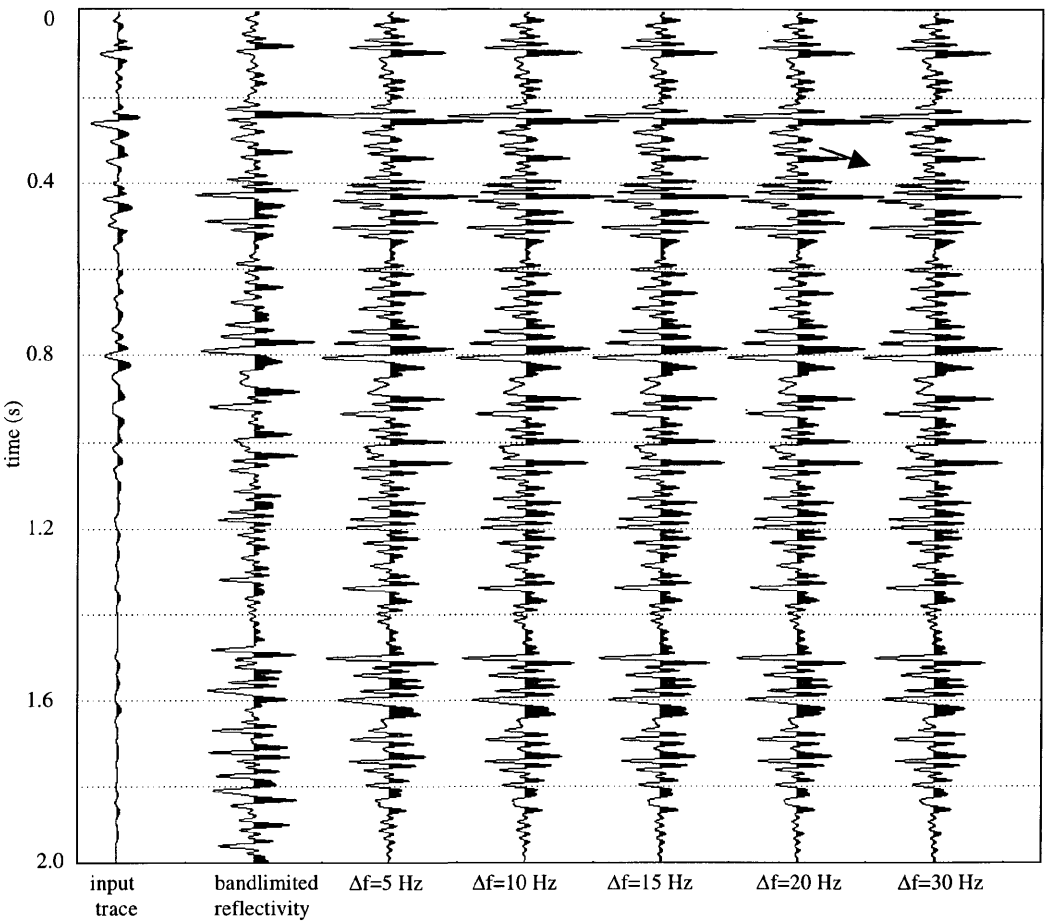

Figure 4.6: Test of the sensitivity of minimum-phase residual-smoothing version of NSD to frequency smoother length. The length of the time-smoother was held constant at 1.0s while the length of the frequency smoother, Δf, was changed from 5 to 30 Hz.

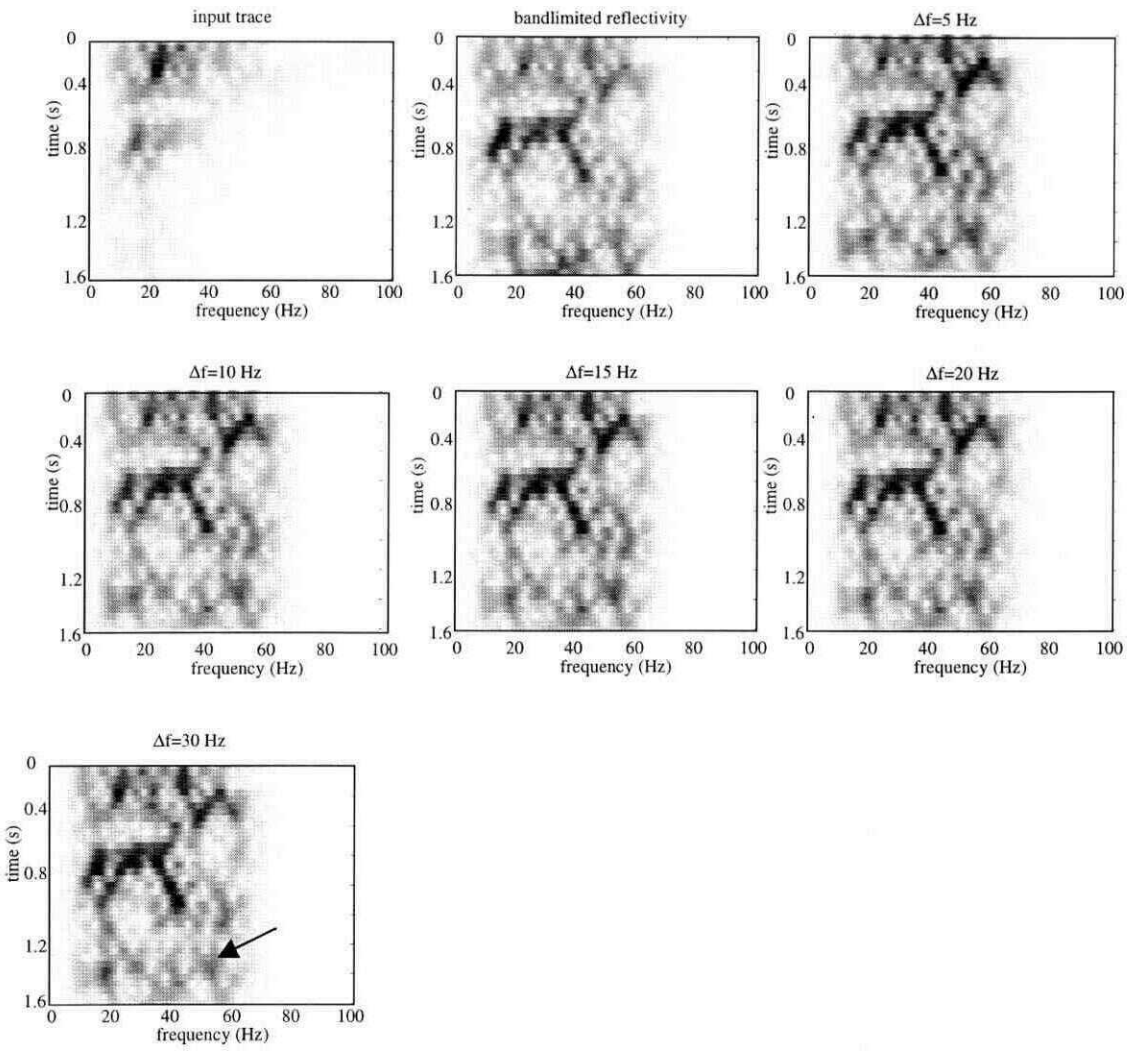

Figure 4.7: |TVS| of traces in Figure 4.6. The |TVS| of the resultant traces from the frequency-smoother tests of the minimum-phase residual-smoothing version of NSD. The time smoother was held constant at 1.0s while the frequency smoother varied.

4.2.4 Time smoother lengths for residual-smoothing NSD

The preferred time smoother for the minimum-phase residual-smoothing method is 1.0s or greater based on Figures 4.8 and 4.9. The reflectivity character of the traces corresponding to the long time smoothers matches the bandlimited reflectivity more closely. For example the trough below 1.0s, pointed out by an arrow on Figure 4.8, is most faithfully reproduced in the traces corresponding to smoothers of 1.0 or 1.5s. The quiet zone at 0.5s, also pointed out by an arrow, is also reproduced most accurately with long time smoothers. In addition, the |TVS| corresponding to the short smoothers are dissimilar to the |TVS| of the bandlimited reflectivity. For example, the |TVS| of the trace smoothed with 0.05s time smoother has greater energy at early times than the |TVS| of the bandlimited reflectivity, as pointed out by arrows on Figure 4.9. This may be because the short time smoothers are smaller than the reflectivity packages, which in this example are approximately 0.4s. The reflectivity package was not adequately smoothed out by the short time smoother and was removed when the operator was applied. The time smoother of 1.0s is preferred because is the trace shows better reflectivity character, its |TVS| compares more favorably to the |TVS| of the bandlimited reflectivity, and because of theoretical expectations (as described previously).

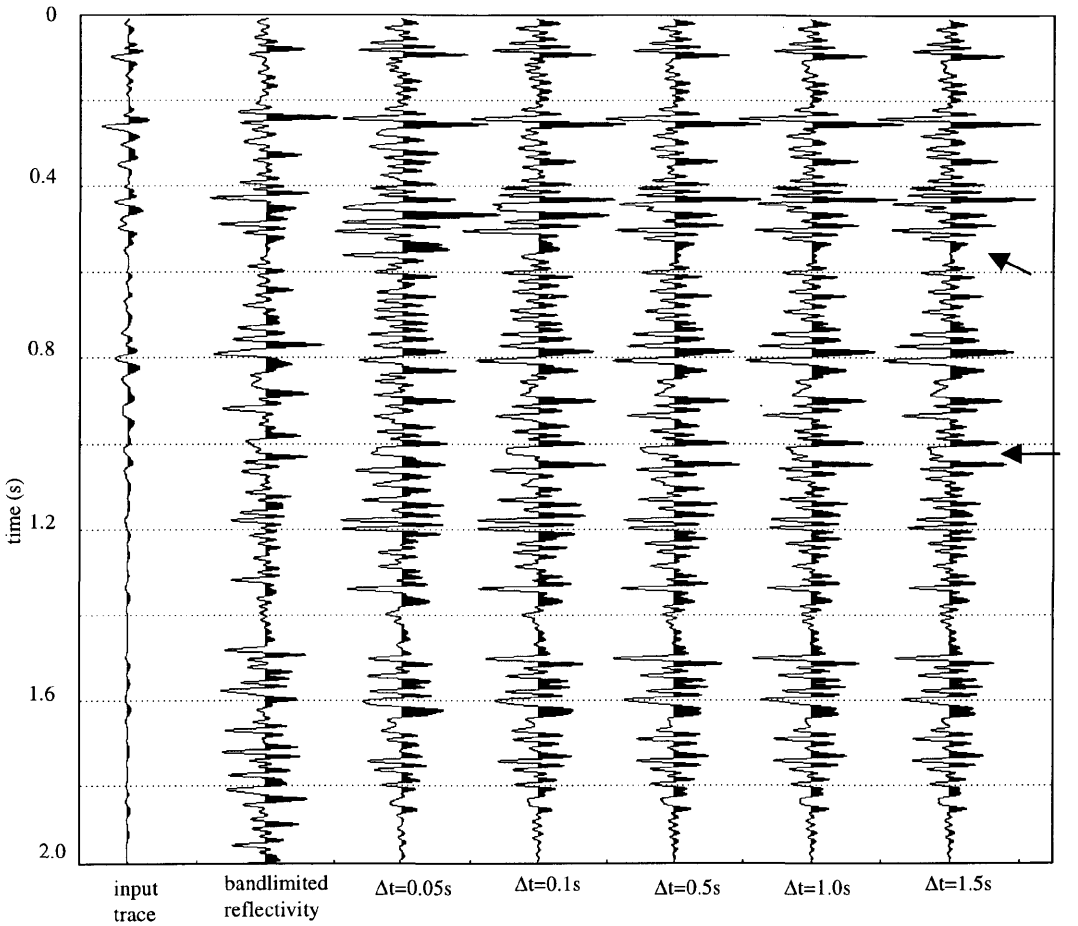

Figure 4.8: Test of the sensitivity of minimum-phase residual-smoothing version of NSD to the time smoother length. The length of the frequency-smoother was held constant at 10 Hz while the length of the time smoother, Δt, was changed from 0.05 to 1.5s.

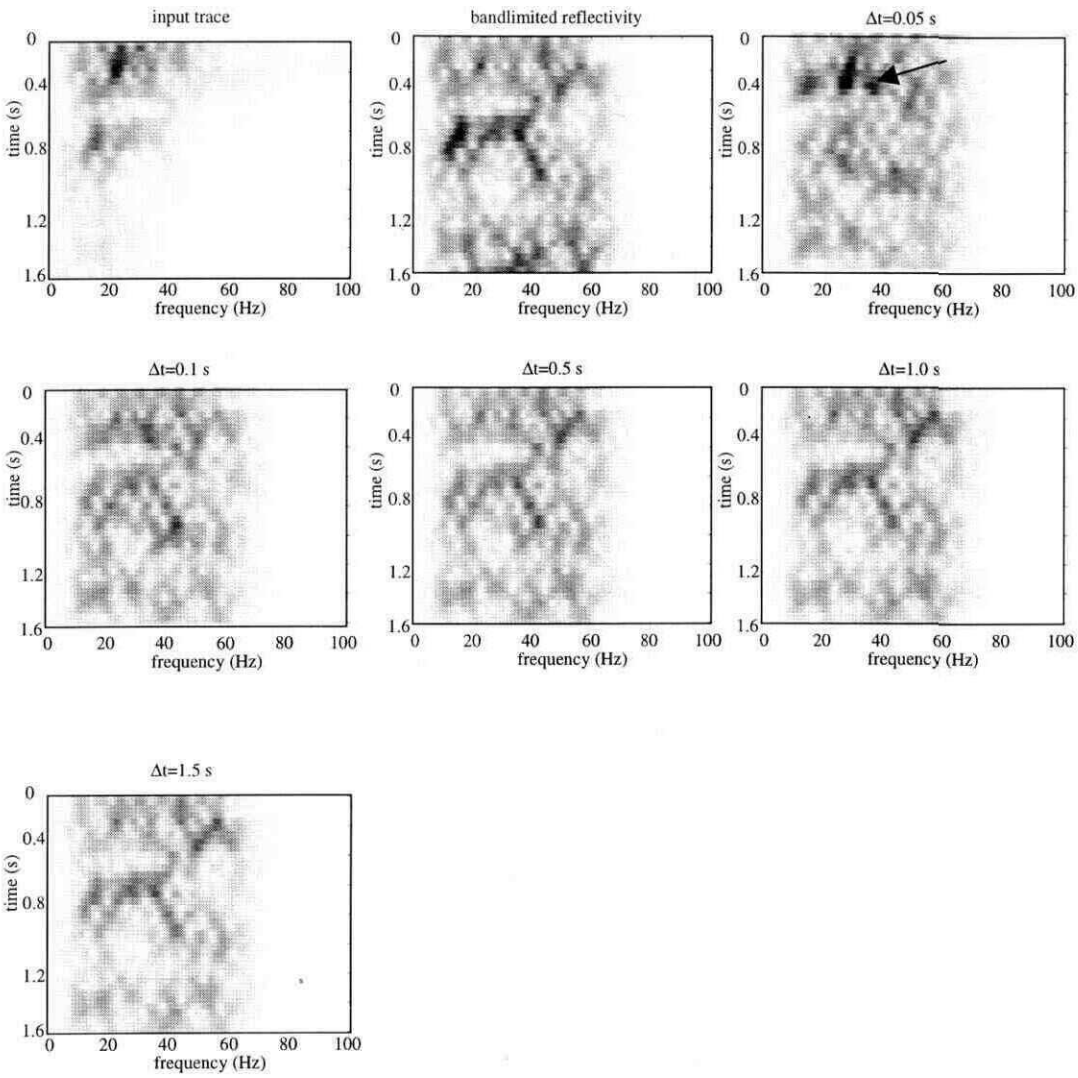

Figure 4.9: |TVS| of traces in Figure 4.8. The |TVS| of the resultant traces from the time-smoother tests of the minimum-phase residual-smoothing version of NSD. The length of the frequency smoother was held constant at 10 Hz while the time smoother was varied.

4.3 Smoother geometry

In this section, a comparison is made of using different smoother geometries in the smoothing process of NSD. Two different smoother geometries were tested, the Hanning smoother (shown in Figure 4.10c) and the boxcar smoother (4.10a) in both the residual-smoothing method and simple-smoothing method. The Fourier transform of a boxcar is a sinc function (4.10b), which has significant sidelobes, slow decay and poor dynamic range. The Fourier transform of the Hanning smoother (4.10d) decays much more sharply , has smaller sidelobes, and more dynamic range.

Convolution can be thought of as a replacement process. The smoother is scaled by a sample of the |TVS| and replicated at the location of the sample. Each output sample receives multiple contributions that are summed. A signal with greater dynamic range, such as the Hanning smoother, can adapt to sharp changes better in the convolution process. Therefore the results from smoothing with the Hanning smoother are expected to be superior to the results from the boxcar smoother.

The results from simple-smoothing NSD are expected to be more sensitive to the change in smoother geometry than the results from residual-smoothing NSD. The |TVS| to be smoothed in the simple-smoothing method is more steep than the |TVS| smoothed in the residual-smoothing method. Therefore a smoother is needed that can approximate sharp changes in the simple-smoothing method. As described above, the Hanning smoother is better suited to this than the boxcar smoother. Since the residual spectrum is

not as steep, the smoother geometry may not make as much of a difference in the residual-smoothing method.

The smoother lengths used in the residual and simple-smoothing methods are 10Hz for both the Hanning and boxcar smoothers based on the tests of Section 4.2. This length may not be optimal for the boxcar smoother because, as can be seen from Figure 4.10, the boxcar smoother does not have tapered ends and is effectively longer than a Hanning smoother of the same specified length. All of the smoothers have been normalized.

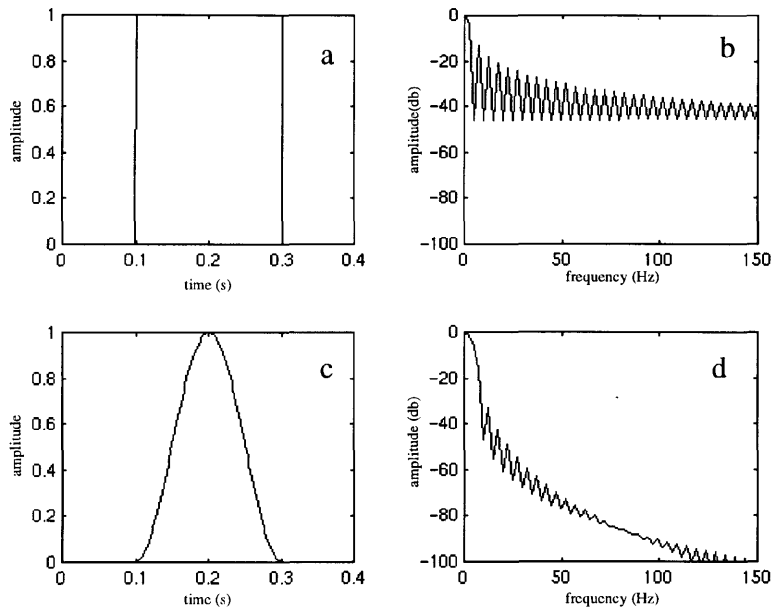

Figure 4.10: The boxcar smoother (4.10a) and its Fourier transform (4.10b) have very little dynamic range. In contrast the Hanning smoother (4.10c) has a spectrum (4.10d) with a greater dynamic range.

4.3.1 Smoothing geometry in simple-smoothing NSD

The traces of Figure 4.11 and the |TVS| of Figure 4.12 were created with simple-smoothing NSD using either the Hanning or the boxcar smoother. The result from the boxcar smoother seems to be 180° rotated in phase, as compared to the output trace from the Hanning smoother and bandlimited reflectivity. The |TVS| of the output trace corresponding to the boxcar smoother appears less whitened at higher frequencies and later times, as pointed out by an arrow in Figure 4.12. As previously described, the

boxcar smoother cannot approximate the steep slopes of the |TVS| and the |TVS| becomes flattened in the smoothing process. Then, when the operator is inverted, not enough of the attenuation surface is removed.

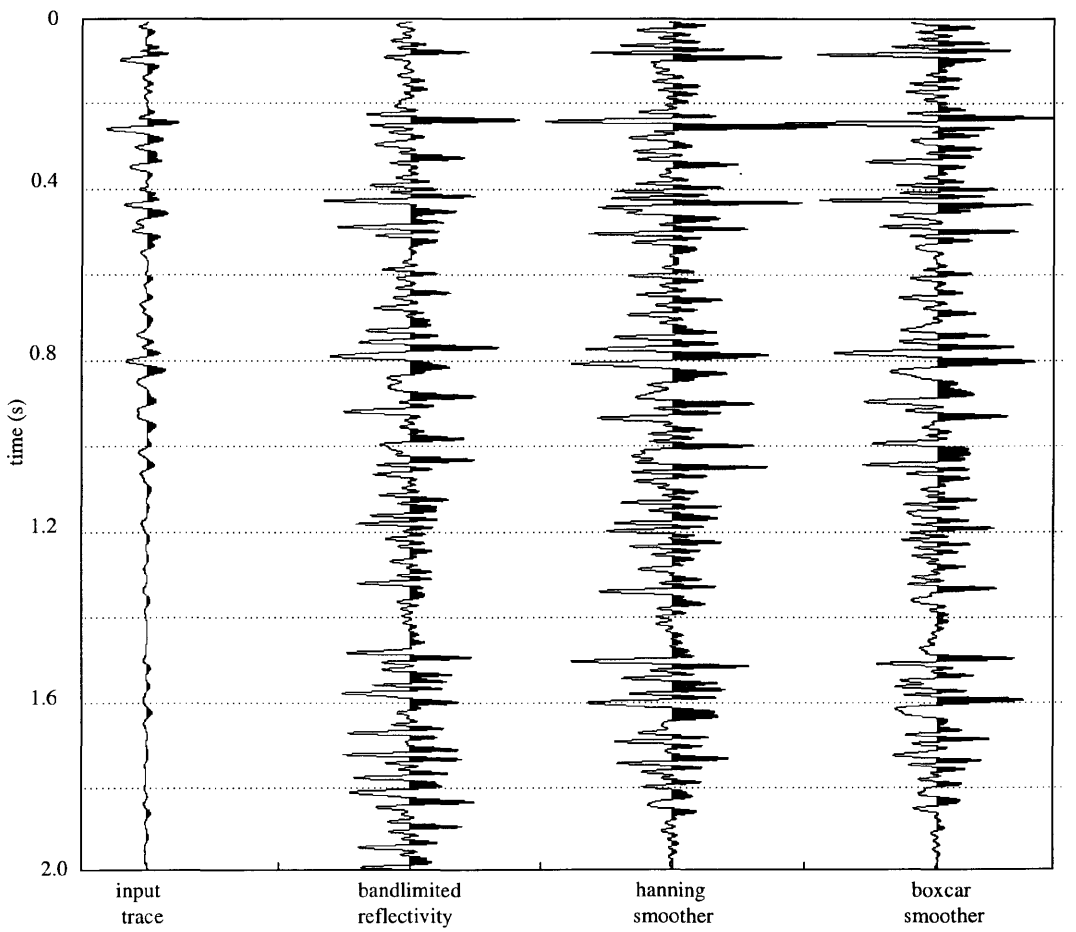

Figure 4.11: Comparison of minimum-phase simple-smoothing results created with different smoother geometries (Hanning smoother or boxcar smoother) in the simple-smoothing method.

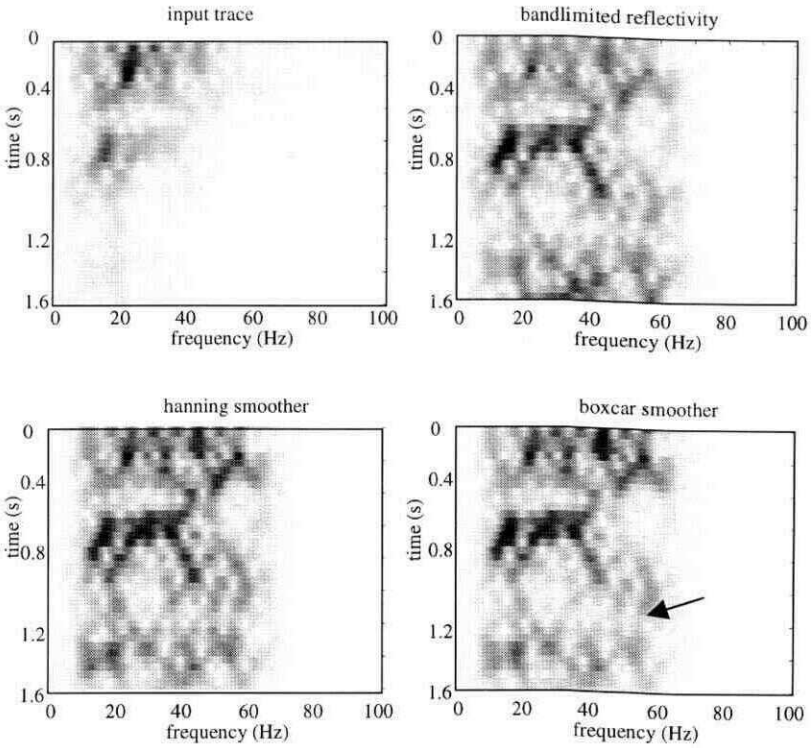

Figure 4.12: The |TVS| of the traces in Figure 4.11.

4.3.2 Residual-smoothing and smoother geometry

The traces in Figure 4.13 and the |TVS| in Figure 4.14 both support the conclusion that the Hanning smoother provides better results than the boxcar smoother in the residual-smoothing method. For example, the doublet trough on the bandlimited reflectivity at approximately 0.8s (shown by the arrow in Figure 4.13) is best approximated by the results from the Hanning smoother and is a spike, not a doublet, on the result from the boxcar smoother. The peak just below 0.8s on this trace may be

rotated in phase and correspond to the doublet trough of the bandlimited reflectivity. The |TVS| of the results from NSD smoothed with the boxcar and Hanning smoothers look similar although, the |TVS| of the trace associated with the boxcar smoother has less energy at later times. As predicted, the residual-smoothing method, especially in regard to phase, seems less affected by the difference in smoother geometry.

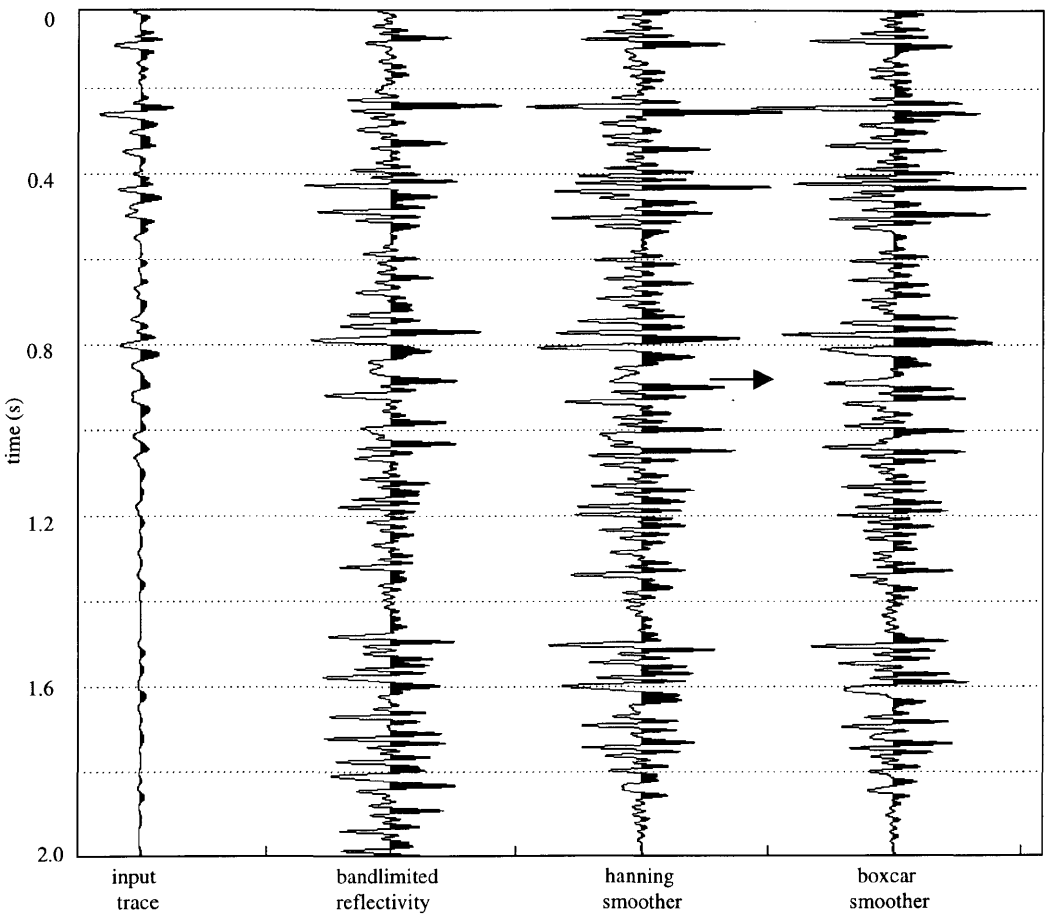

Figure 4.13: Comparison of minimum-phase residual-smoothing results created with different smoother geometry (Hanning smoother or boxcar smoother) in the residual-smoothing method.

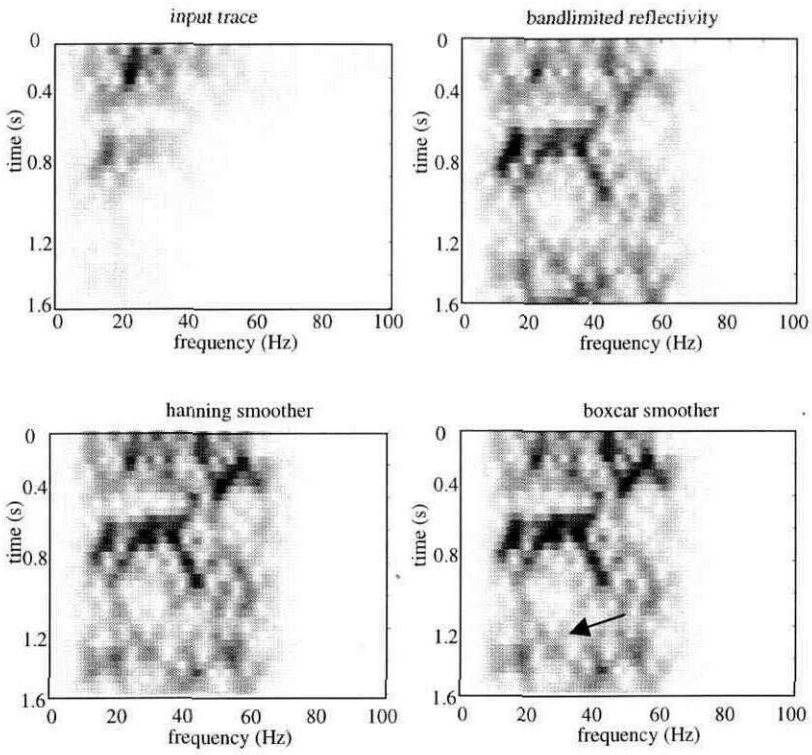

Figure 4.14: The |TVS| of the traces in Figure 4.13.

4.4 Sensitivity of NSD to $\hat{Q}$

The NSD operator is determined statistically from the data and not designed explicitly on a value of Q. The Q estimate, $\hat{Q}$, in NSD is only used to remove an approximate attenuation/gain surface from the |TVS| of the gained input trace. This residual spectrum is squared to form the residual power spectrum. The attenuation/gain surface is replaced after the residual power spectrum has been smoothed. This suggests that residual-smoothing NSD may be relatively insensitive to errors in $\hat{Q}$. Q is difficult

to estimate in practice, and being able to remove attenuation without an exact value of $\hat{Q}$ would be advantageous.

If $\hat{Q}$ is estimated to be too large, then not enough exponential attenuation is removed in the formation of the residual spectrum, and it will have residual decay. If $\hat{Q}$ is estimated to be too small, then too much exponential attenuation will be removed and the |TVS| of the residual spectrum will have an exponential growth in time and frequency. In either case, the residual spectrum will not be flat and smoothing will cause distortion. It is better, however, to estimate $\hat{Q}$ too large, than too small. This can be seen by expanding the exponential remaining after the estimated Q surface has been removed

$$e^{-\pi ft\left(\frac{1}{Q}-\frac{1}{\hat{Q}}\right)} \approx 1-\pi ft\left(\frac{\hat{Q}-Q}{Q\hat{Q}}\right)+\ldots \tag{4.1}$$

$$\approx 1-\pi ft\frac{\delta Q}{Q\hat{Q}}. \tag{4.2}$$

The estimate of Q should be chosen to minimize the second term of Equation (4.2), $\pi ft\frac{\delta Q}{Q\hat{Q}}$. A $\hat{Q}$ estimated too large will make the second term of Equation (4.2) smaller than a $\hat{Q}$ estimated too small by the same amount. The graph in Figure 4.15 shows how the value of the second term of Equation (4.2) varies with $\hat{Q}$ for Q=50. From the graph it

can be seen that the magnitude of the second term of Equation (4.2) increases more rapidly with $\hat{Q}$ too low than $\hat{Q}$ too high.

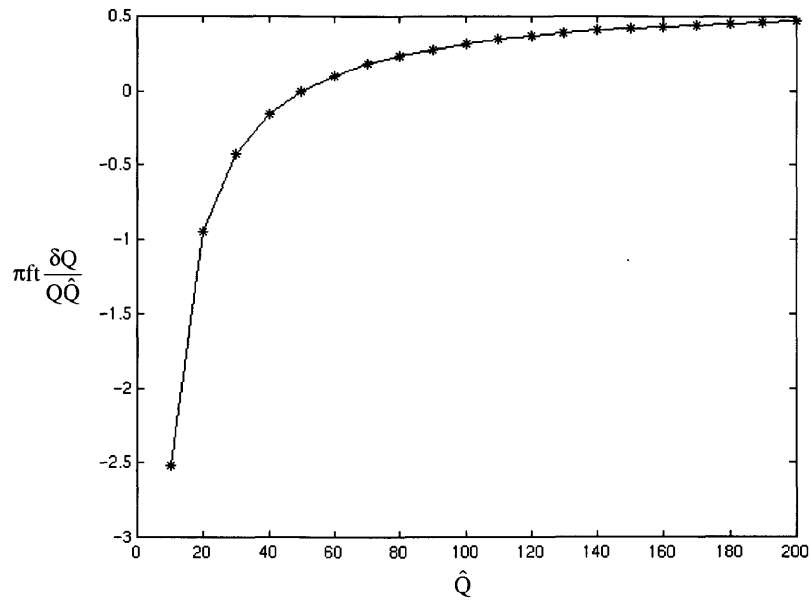

Figure 4.15: Sensitivity of the decay exponent to estimates of Q. For perfect removal of the exponential surface, the decay exponent (the term on the y-axis of the graph) must be zero. It can be seen that an estimate of Q too large is better than an estimate of Q too small by the same amount.

Figure 4.16 shows a synthetic trace, created with Q=50, that has been deconvolved several times with $\hat{Q}$ ranging from 12.5 to 200. The |TVS| of each of the traces is shown in Figure 4.17. The output traces are progressively worse as the error in $\hat{Q}$ increases. For example, the doublet troughs at 0.8s and at 1.0s (pointed out by arrows)

match the reflectivity poorly when $\hat{Q}$ is very low (such as 12.5) or very high (200). As predicted, the trace corresponding to $\hat{Q}$=12.5 seems to match the bandlimited reflectivity worse than the trace corresponding to $\hat{Q}$=100 or 200. This is obvious at early times, such as 0.4s to 0.6s as pointed out with arrows on Figure 4.16.

The |TVS| of the trace deconvolved with $\hat{Q}$=12.5 appears distorted compared to the |TVS| of the bandlimited reflectivity. Its energy seems concentrated in two areas as pointed out by arrows in Figure 4.17. The |TVS| of the trace deconvolved with the largest estimate of Q (200) looks lacking in energy at later times. However, the |TVS| corresponding to $\hat{Q}$=12.5 compares less favorably to the |TVS| of the bandlimited reflectivity than the |TVS| corresponding to $\hat{Q}$=200, even though the error in the estimate of Q is greater in the latter case. This effect has been predicted by theory and confirmed by the examples of the traces and |TVS|.

The results from NSD are best if $\hat{Q}$ is correct, although the differences in the output traces between using the correct $\hat{Q}$ and an erroneous $\hat{Q}$ are relatively small. The output from NSD is worse if $\hat{Q}$ is estimated to be too small than if it is estimated to be too large by the same amount.

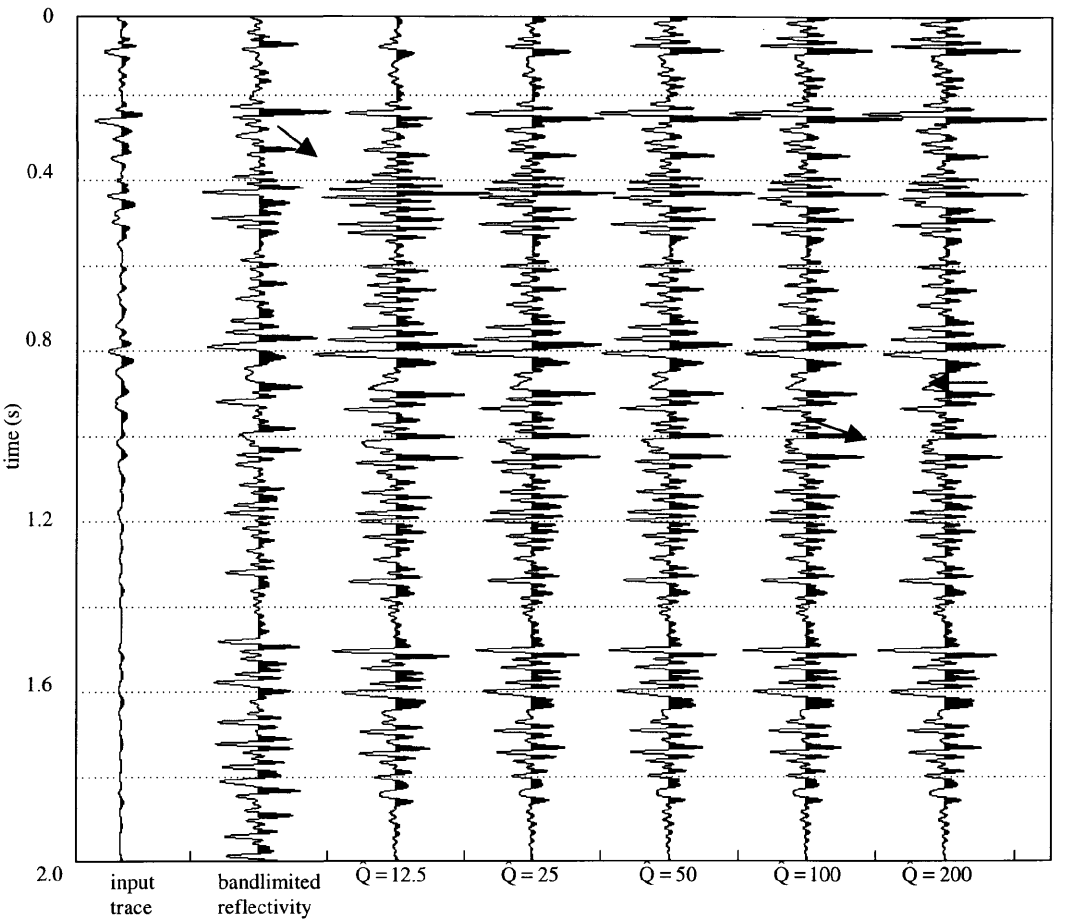

Figure 4.16: Test of the sensitivity of NSD to errors in the estimate of Q, $\hat{Q}$. The input trace has been created with attenuation corresponding to a Q value of 50 and then deconvolved with minimum-phase residual-smoothing NSD with different values of $\hat{Q}$.

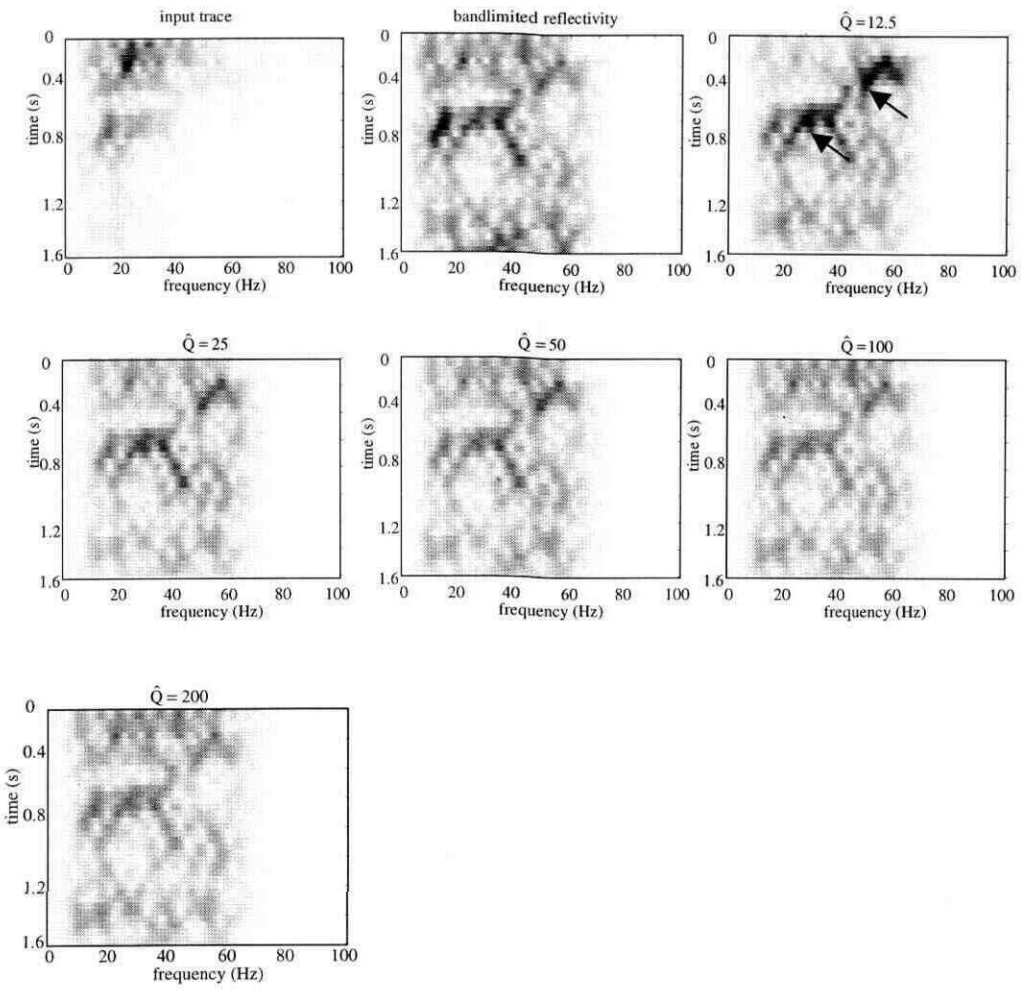

Figure 4.17: The |TVS| of the output traces from Figure 4.16.

4.5 Window length in the |TVS| calculation

The window length in the |TVS| calculation is an important parameter and is related to the time and frequency resolution of the |TVS|, as described in Section 2.3.1. A short window length provides detailed time information in the |TVS| at the expense of

frequency resolution and a long window provides the opposite. When choosing a window length, the size of the embedded wavelet must be considered in addition to resolution issues. The window must be long enough to encompass the seismic wavelet which is typically approximately 0.2 s in length. The window length was varied in the calculation of the |TVS| of the input trace in the minimum-phase residual-smoothing version of NSD to see how this parameter affected the results.

The |TVS| of the gained input trace calculated with different window lengths are shown in Figure 4.18. At small window lengths, the |TVS| looks poorly resolved in frequency and well-resolved in time and at large window lengths, it looks poorly resolved in time and well-resolved in frequency. It is obvious from these plots that the window length has a significant role in the shape of the |TVS|.

The output traces from window length tests are shown in Figure 4.19 and the |TVS| are shown in Figure 4.20. The NSD results from the examples with very small window lengths (0.05 to 0.1s) are quite poor. The traces in Figure 4.19 look as if they were lacking high frequencies, especially at later times, such as 1.4s and greater (pointed out by an arrow). The |TVS| in Figure 4.20 do not look whitened at later times. A zone on these |TVS| that is particularly lacking in frequency content is pointed out by arrows. The reason the traces and the |TVS| corresponding to small window lengths look lacking high frequencies is because frequency information has been lost due to the low resolution in frequency of the |TVS| of the input trace.

The traces corresponding to the large window lengths, 0.5s and 1.0s, have a nonstationary appearance and the |TVS| do not look whitened at later times. The reason for this nonstationarity is related to the poor resolution in time of the |TVS| of the input trace. The |TVS| of the input trace corresponding to a window length of 1.0s (from Figure 4.18) shows that time information past 0.8s has been lost. Therefore its corresponding output trace (from Figure 4.19) and its |TVS| (from Figure 4.20) look highly nonstationary after 0.8s.

A moderate window length of 0.2s was chosen as the default for NSD in the calculation of the |TVS| of the input trace. It provides a compromise between time and frequency resolution and encompasses the embedded wavelet.

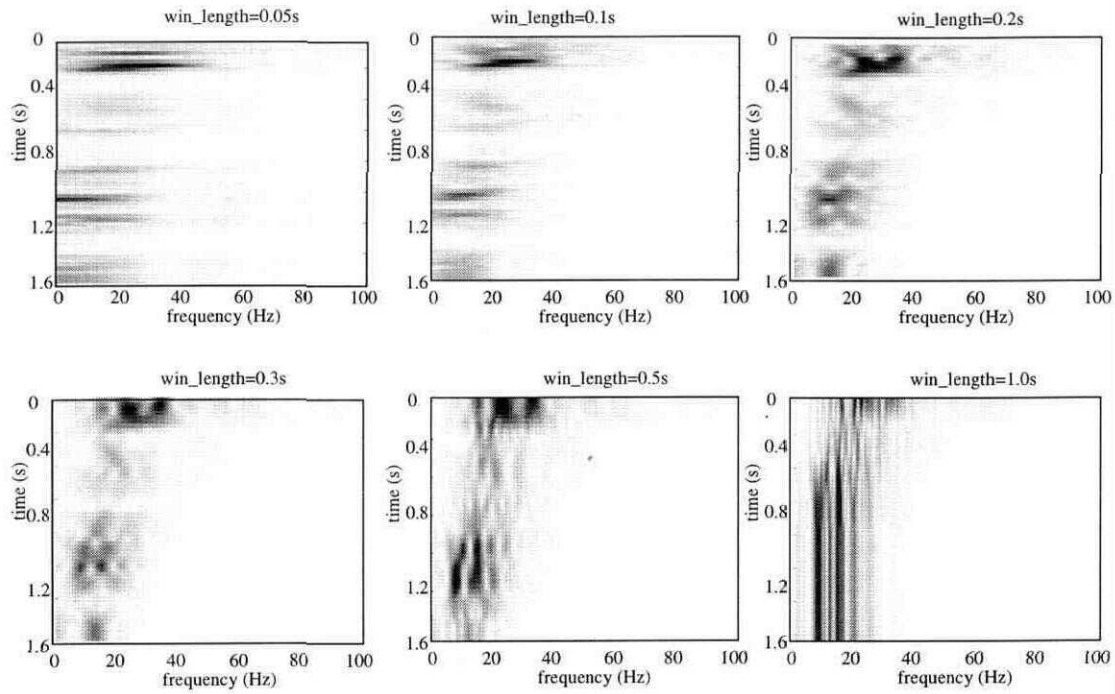

Figure 4.18: Comparison of the |TVS| of the gained input trace for varying window lengths.

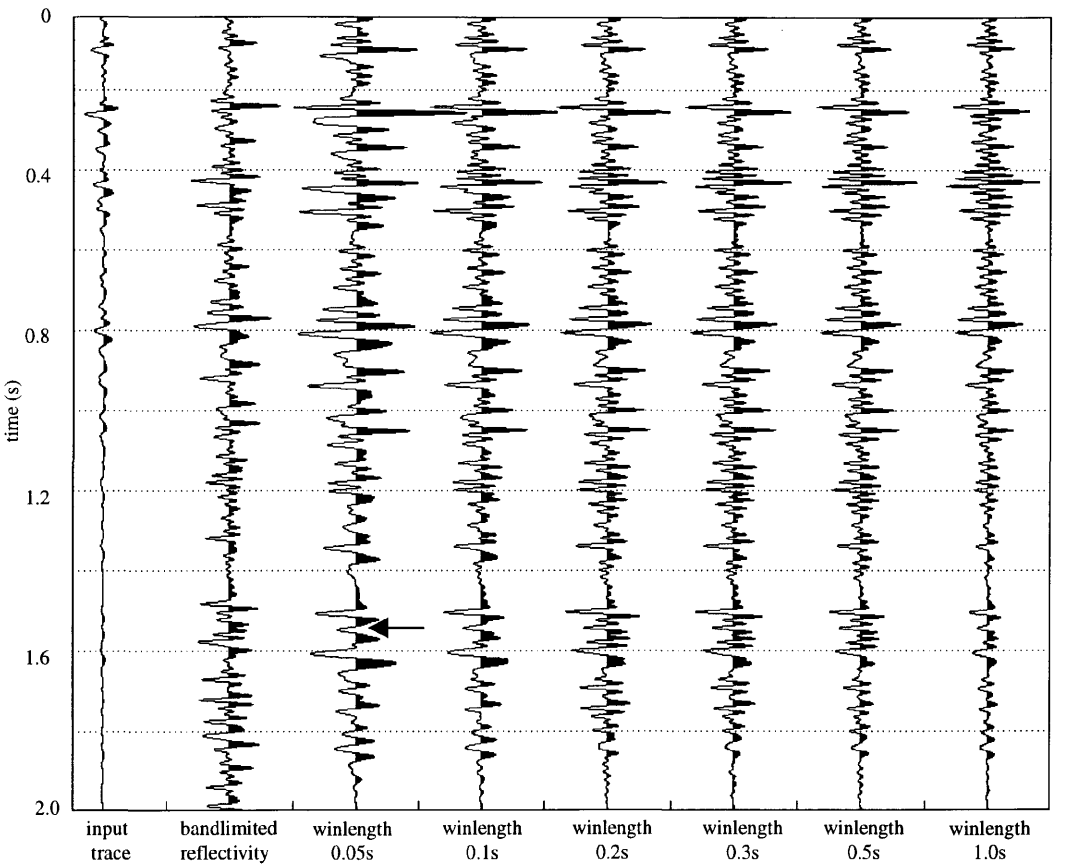

Figure 4.19: Output traces from NSD that have where the |TVS| of the ungained input trace has been calculated with different values for the window length.

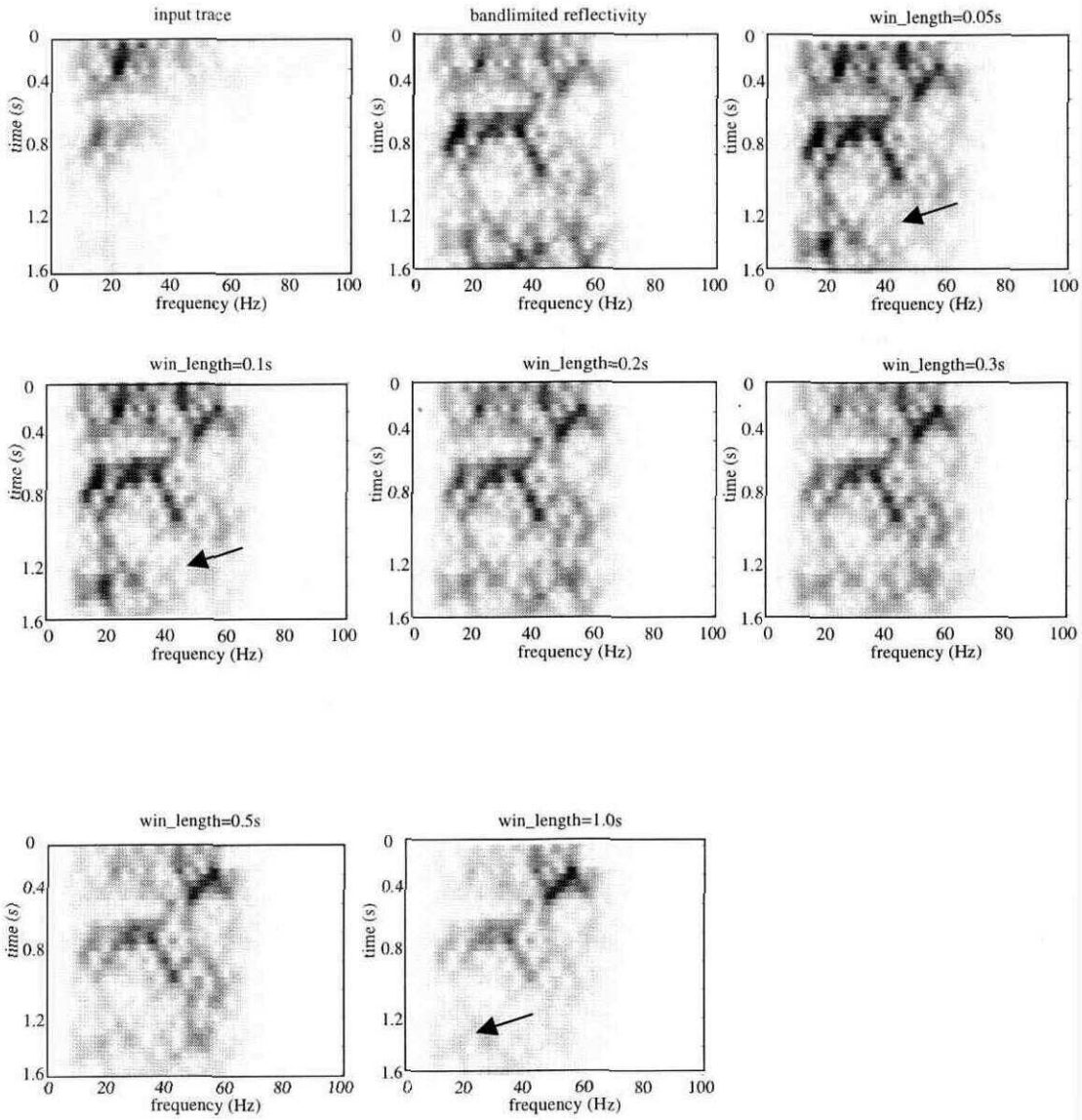

Figure 4.20: The |TVS| of the traces from Figure 4.19.

4.6 Window increment in the |TVS| calculation

The window increment dictates the time sampling rate for the |TVS|, as described in Section 3.3.2. A small sample rate will most accurately reproduce the time-frequency characteristics of the trace in the |TVS|, but will also increase the run-time of the program. A large sample rate aliases steep time-frequency effects. As discussed in Section 3.3.2, the input trace has been gained to help prevent aliassing, however it is still a concern.

The window increment should be specified as a percentage of the window size of the |TVS| calculation to avoid gaps between spectral measurements. Typically 80 to 90% overlap between windows is desired.

The window length in these experiments is 0.2s. The window increment in the initial |TVS| calculation in the operator design stage of NSD was varied from 0.01s (overlap of 95%), 0.04s (overlap of 80%), 0.1s (overlap of 50%) to 0.2s (overlap of 0%) to determine how it affects the results from minimum-phase residual-smoothing NSD. Figure 4.21 shows the |TVS| of the gained input trace calculated with these differing values of the window increment. The |TVS| calculated with the smallest window increment (0.01s) looks more finely sampled in time than the |TVS| calculated with the largest window increment (0.2s). As the window increment increases, the |TVS| becomes more blocky.

The traces are shown in Figure 4.22 and the |TVS| in Figure 4.23. The traces and |TVS| look very similar to each other. Only very slight differences in the traces, such as can be seen just above 0.6s (marked by an arrow), can be discerned. Based on the |TVS| of Figure 4.21, a window increment of 0.04s (80% overlap of the window) has been chosen as the default value for NSD.

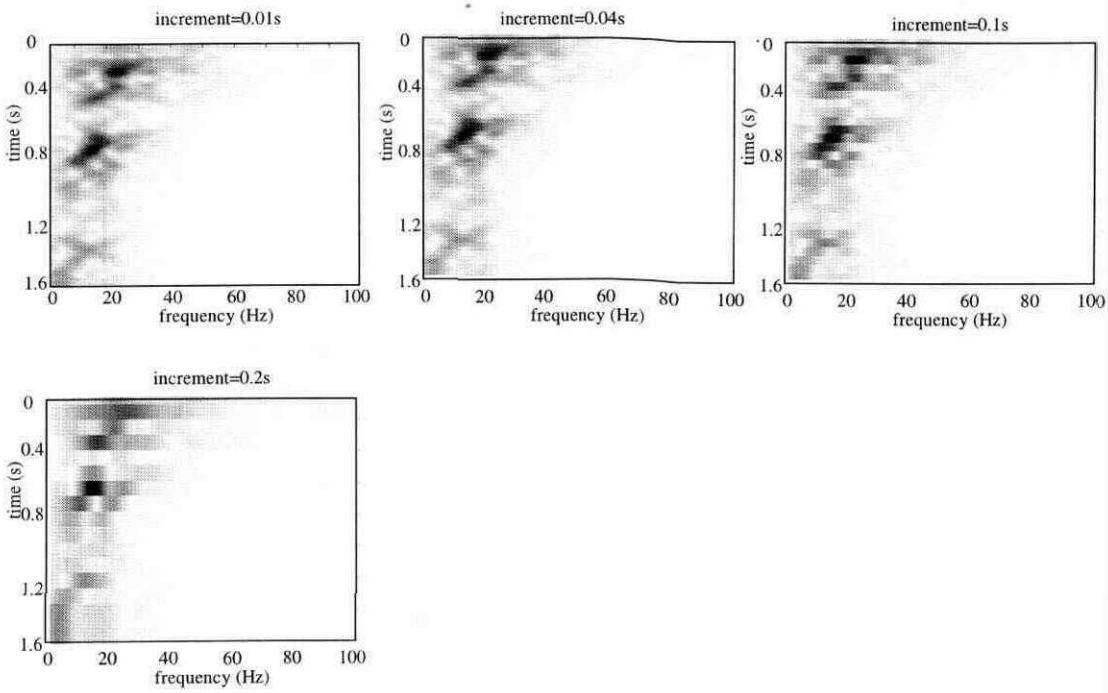

Figure 4.21: The |TVS| of the input trace created with varying window increments.

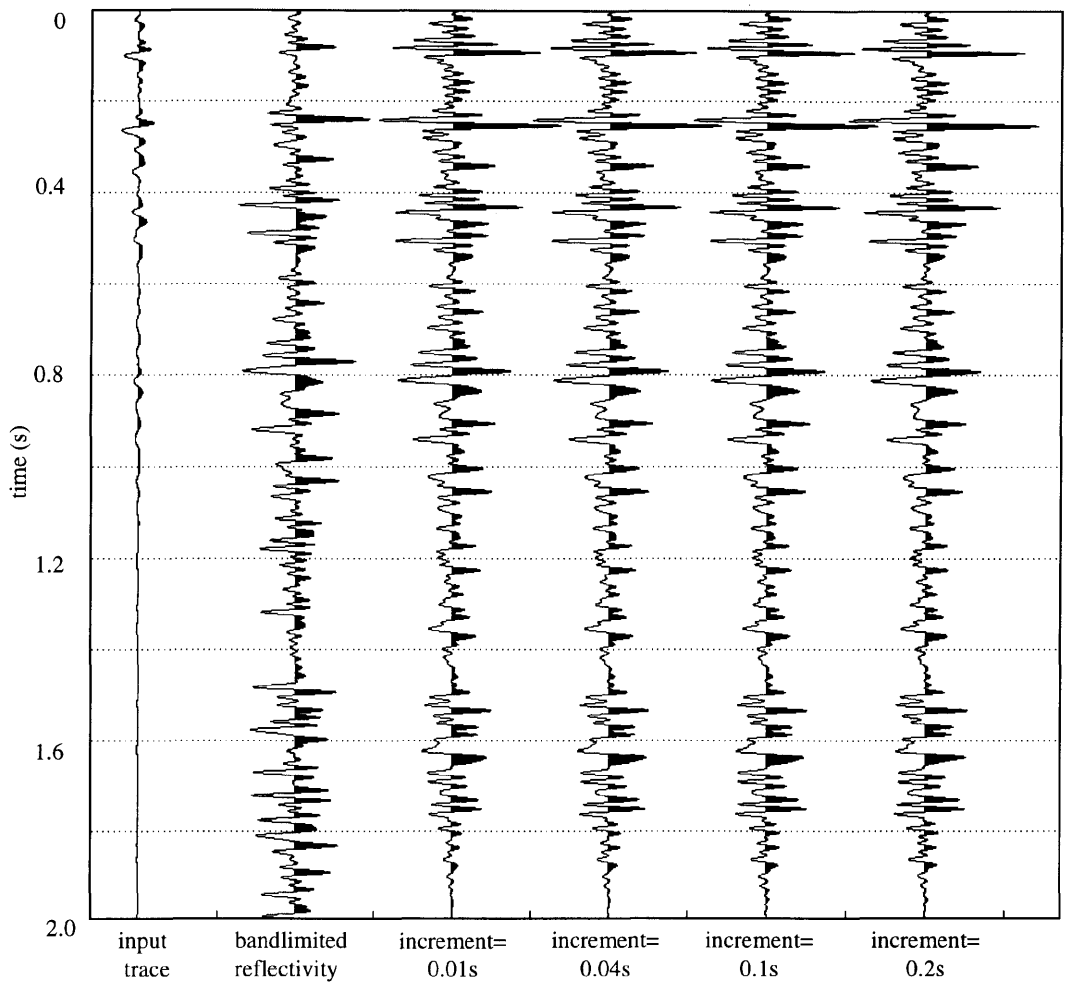

Figure 4.22: Test of the sensitivity of minimum-phase residual-smoothing NSD to the window increment of the |TVS| calculation in the operator design stage.

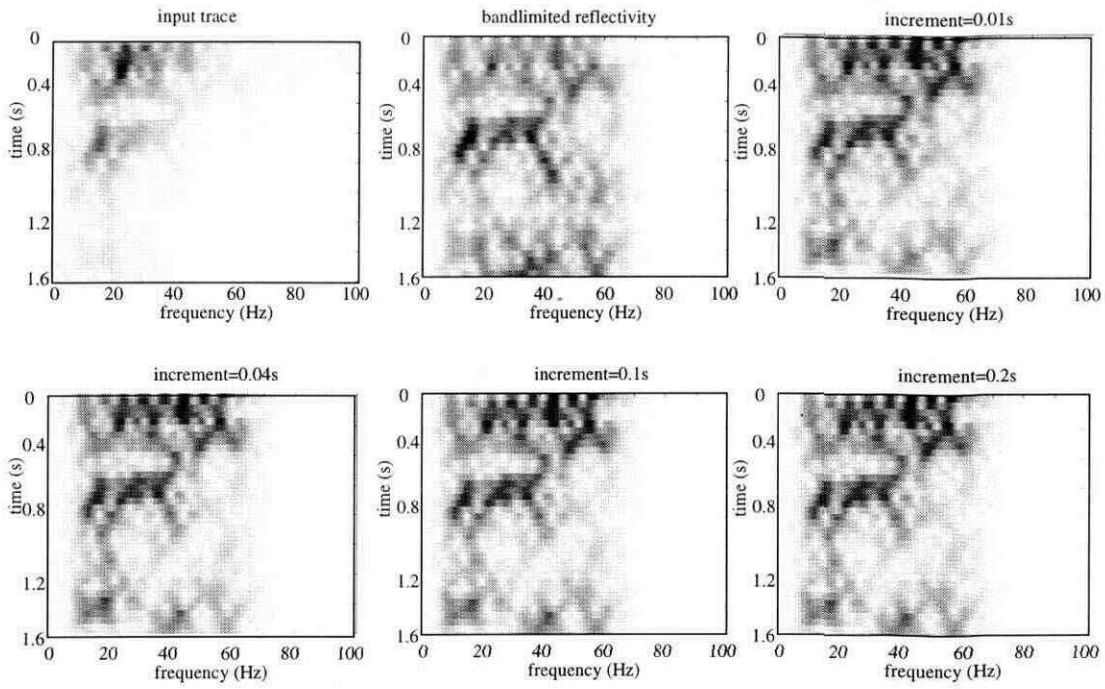

Figure 4.23: The |TVS| of the traces in Figure 4.22.

4.7 Exponential gain factor

As described in Section 3.2.2, the trace input to NSD needs to be gained. The gain is required so that the steep exponential decay surface of the input trace is well approximated by the |TVS|. However, if the exponential gain constant is too large, frequencies at later times of the |TVS| will be much stronger and become distorted during the smoothing process.

The input trace was gained with varying values and then deconvolved with minimum-phase residual-smoothing NSD to determine how sensitive NSD is to the

exponential gain constant. The gained input traces are shown in Figure 4.24. The input traces gained with an exponential gain constant of $0s^{-1}$ or $0.5s^{-1}$, still show amplitude decay. The traces with gain constants that are too large, such as $2s^{-1}$ or $3s^{-1}$, show exponential growth. The gain constant of $1s^{-1}$ approximately corrects for the amplitude decay and is expected to produce the best results in NSD.

The output traces from NSD are shown in Figure 4.25 and the |TVS| in Figure 4.26. Using a gain constant that is too large seems to distort the output trace relative to the bandlimited reflectivity, but using a gain constant that is too small does not seem to adversely affect the output trace. The phase seems affected when the gain constant is too large. The traces gained with large constants do not compare well to the bandlimited reflectivity. For example, the peak or trough at approximately 1.5s on the bandlimited reflectivity, pointed out by an arrow, is best approximated by the traces with small and intermediate gain constants. It looks reverse polarity on the traces with large gain constants. The |TVS| grow more distorted as the gain constant increases past $1s^{-1}$. Small and intermediate gain constants provide reasonable results. For this input trace a gain constant of $1s^{-1}$ has been chosen.

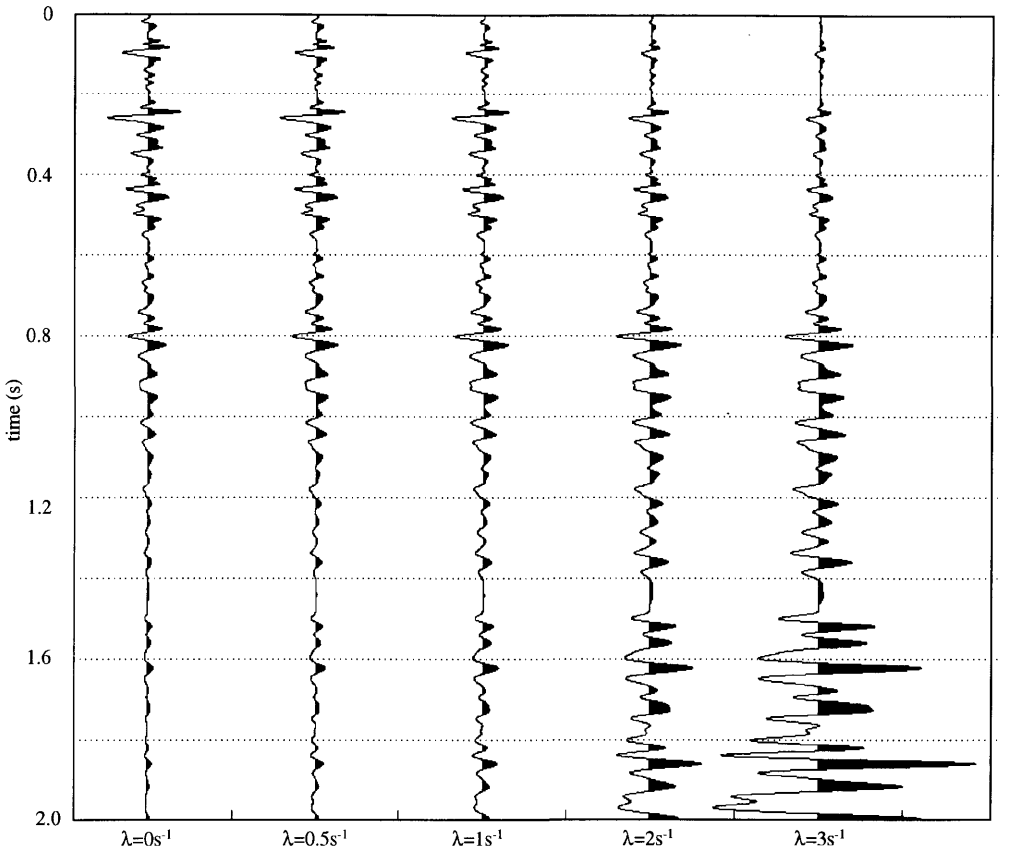

Figure 4.24: Input trace gained with different values of the exponential gain constant.

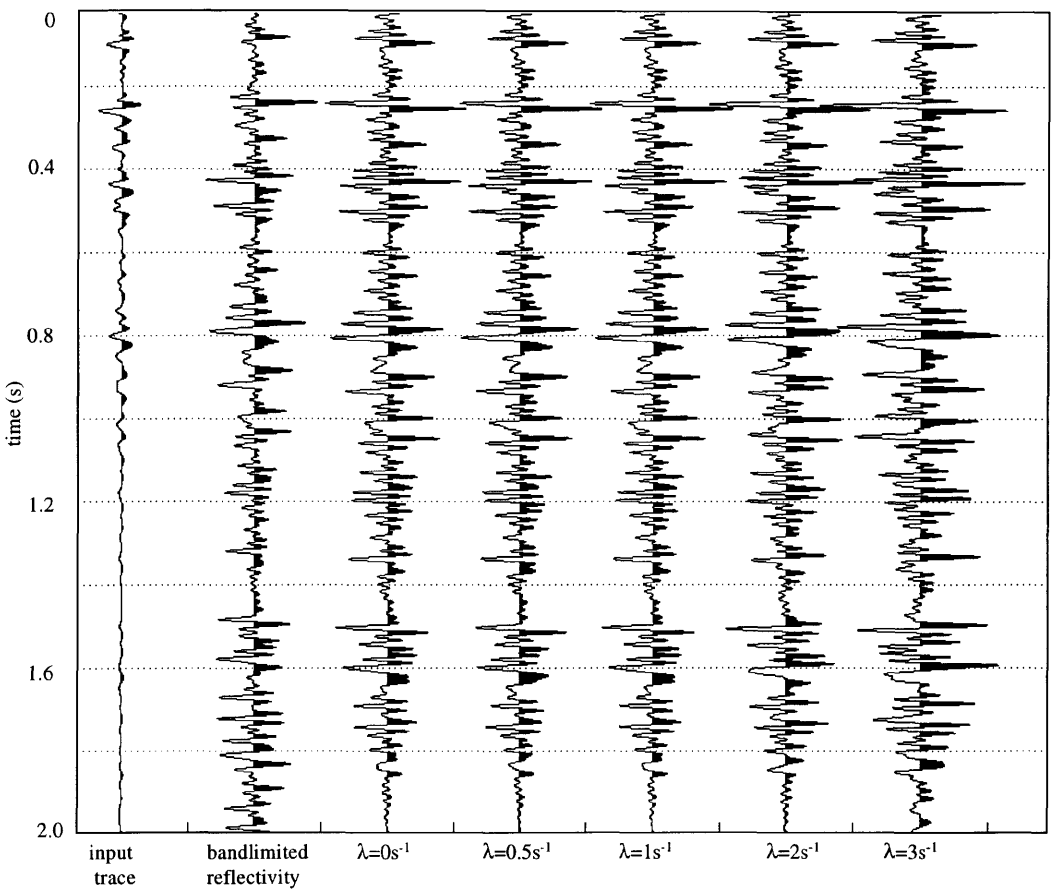

Figure 4.25: Test of sensitivity of minimum-phase residual-smoothing NSD to the exponential gain of the input trace.

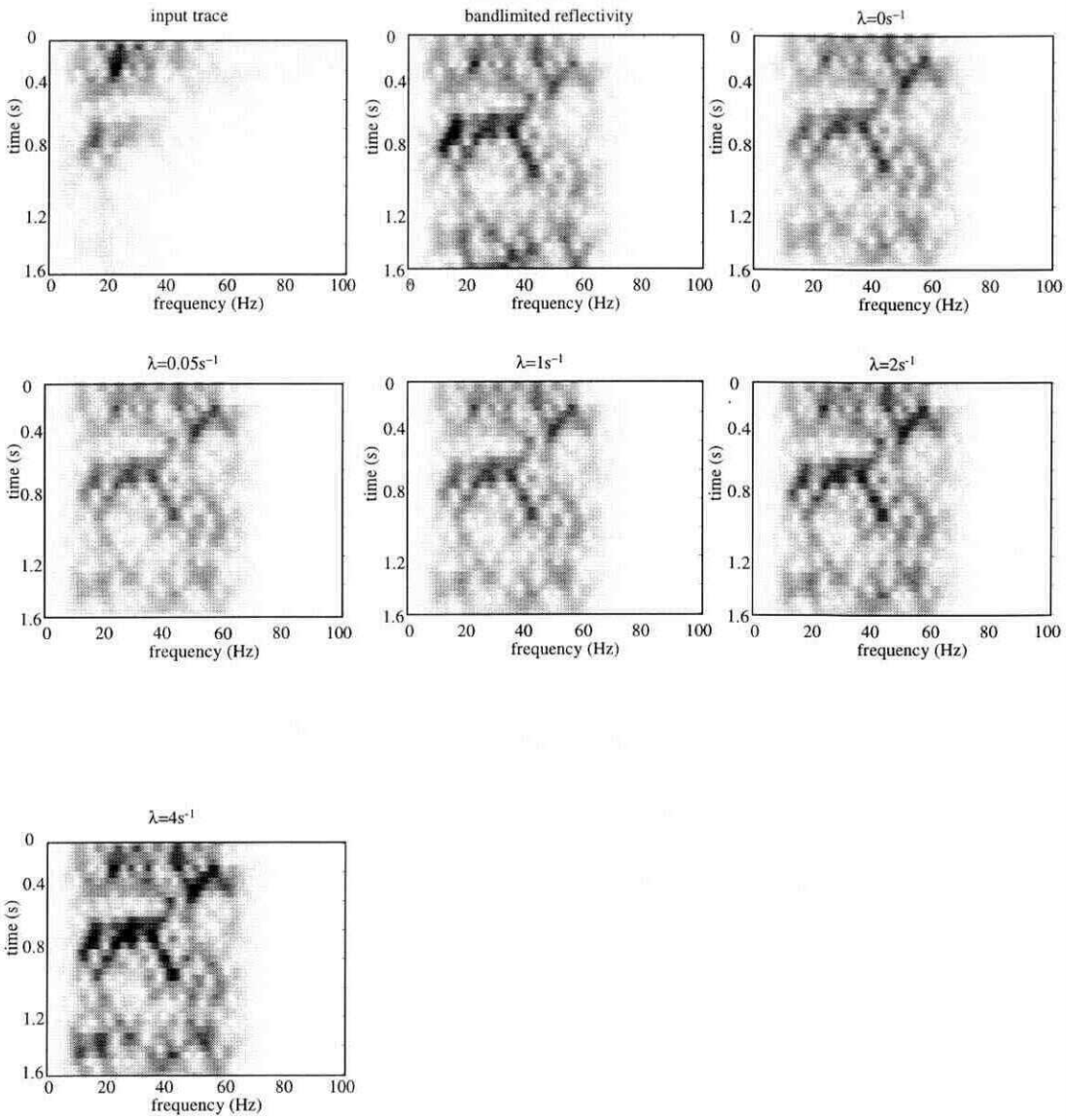

Figure 4.26: The |TVS| of Figure 4.25.

4.8 Comparison of NSD to stationary deconvolution

Figure 4.27 shows the results from four possible versions of NSD (minimum-phase or zero-phase, simple-smoothing or residual-smoothing). They are compared to the input trace, bandlimited reflectivity, results from time-variant spectral whitening (TVSW), and results from a combination of and gain and Wiener deconvolution. Time-variant spectral whitening (Yilmaz, 1987) is a technique to compensate seismic data for attenuation, but not for dispersion. The operators in both the simple-smoothing and residual-smoothing methods were smoothed with 10Hz frequency smoothers and 1.0s time smoothers. In NSD, a stabilization factor of 0.001 was used. The Wiener operator was designed on the first 0.3 seconds of the input trace and 25 autocorrelation lags were used in the operator design. The number of autocorrelation lags was chosen to be consistent with the smoothers used for nonstatioanry deconvolution, so that a comparison could be made of the two methods. Windowing at this autocorrelation lag is equivalent to a frequency domain smoother of 10 Hz. Wiener deconvolution had a stabilization factor of 0.0001 (the fraction of the zero lag of the autocorrelation) added before inversion of the operator.

The residual-smoothing process seems more effective than simple-smoothing. The minimum-phase residual-smoothing result has better reflectivity character than the minimum-phase simple-smoothing result. This is most obvious between 0.8s and 1.4s on the traces. For example, the doublet trough at 1.0s (pointed out by an arrow) in the bandlimited reflectivity is best reproduced by the result from minimum-phase residual-

smoothing. The peak at 0.8s on the bandlimited reflectivity (pointed out by an arrow) also compares most favorably to the result from minimum-phase residual-smoothing.

The |TVS| reinforce the idea that residual-smoothing NSD provides better results than simple-smoothing NSD. The |TVS| of the simple-smoothing results do not show the pattern in the |TVS| of the bandlimited reflectivity clearly. The |TVS| have been whitened but without the proper reflectivity character.

The improvement in performance of the residual-smoothing method over the simple-smoothing method is related directly to the removal of the exponential attenuation surface before smoothing. The exponential decay surface is distorted by any smoothing, although smaller smoothers have been used in an attempt to minimize this effect.

The minimum-phase output in both versions of NSD is more favorable than the zero-phase outputs. The result from the minimum-phase versions have better reflectivity character, as compared to the bandlimited reflectivity, than the results from the zero-phase operator. This can be seen by a comparison of the features at 0.8s and 1.0s on the minimum-phase and zero phase results. Although the minimum-phase methods produce results better than the zero-phase methods they do not completely correct for phase rotation. This is because, as mentioned in Section 1.8, digital minimum-phase estimation with a Hilbert transform is imperfect.

Deconvolution based on the zero-phase simple-smoothing version of NSD yields results similar to that of TVSW, as can be seen from Figure 4.27. The |TVS| of the output

from TVSW is strongly whitened however it does not match the TVS of the bandlimited reflectivity well at low frequencies, especially at later times. A zone in the |TVS| of the trace deconvolved with TVSW that does not match the |TVS| of the reflectivity is pointed out by an arrow on Figure 4.28. The last trace of Figure 4.27 is a result of the combination of gain and Wiener deconvolution and represents conventional processing. This trace still exhibits reflections that broaden in time, indicating that the effects of attenuation have not fully been removed. The |TVS| of gain and Wiener deconvolution (Figure 4.28) exhibits a corresponding strong loss of bandwidth with time. All of the deconvolved traces show an erroneous phase rotation just below 0.2s, pointed out by arrows on Figure 4.27. This may be an error caused by edge effects.

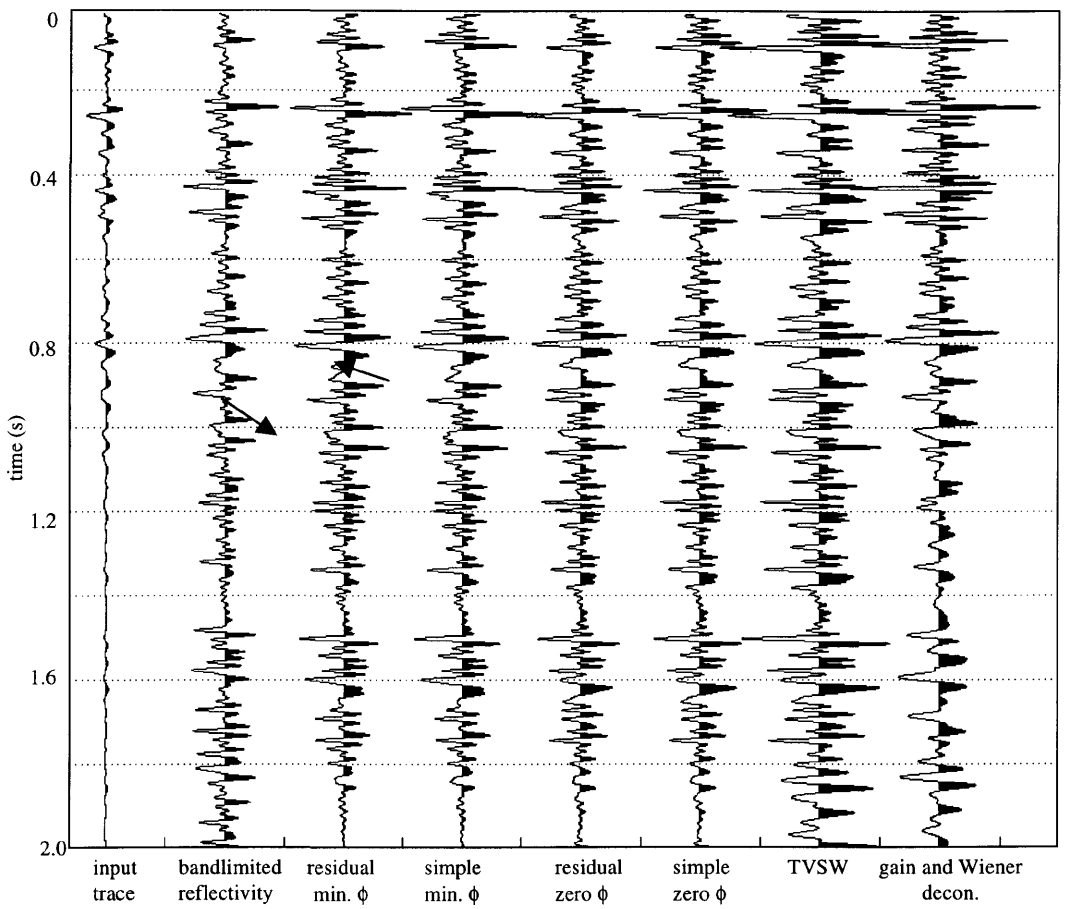

Figure 4.27: A comparison of output traces from various deconvolution algorithms. The four combinations of NSD are displayed next to each other in the middle of the diagram.

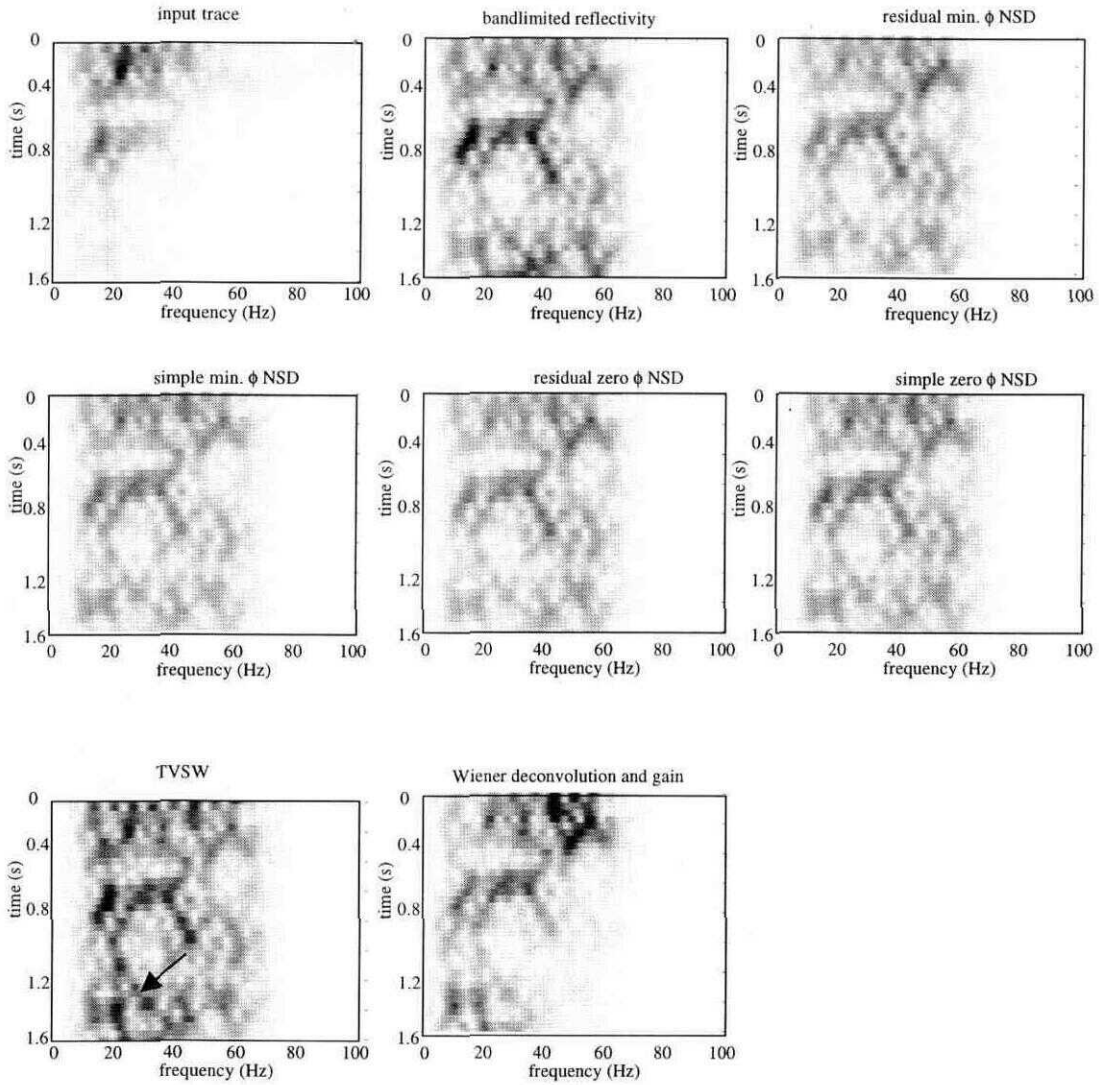

Figure 4.28: A comparison of the |TVS| of various deconvolution techniques, input trace and bandlimited reflectivity.

4.9 Comparison of NSD to bandlimited reflectivity with constant phase rotations

As explained in Section 1.8.4, a constant multiplied with the amplitude spectrum of a trace, S(f), can cause a constant phase error in the digital phase estimation. The digital minimum-phase estimate is computed as in Equation (1.29)

$$\phi(f) = H[\ln(C * A(f))], \tag{4.3}$$

where C is the constant multiplier. Therefore,

$$\phi(f) = H[\ln(C)] + H[\ln(A(f))]. \tag{4.4}$$

In real data it is unknown if the amplitude spectrum has been multiplied by a constant or, if it has, what that constant may be.

The bandlimited reflectivity has been rotated with constant phase rotations of 45° and compared to the output trace from minimum-phase residual-smoothing to determine if there is a constant phase shift in the NSD output. Based on Figure 4.29, the output from minimum-phase residual-smoothing NSD matches the zero-phase bandlimited reflectivity most closely. The trace from NSD seems to be shifted later in time with respect to the bandlimited reflectivity by approximately 0.15s. It would seem that the minimum-phase residual-smoothing version of NSD corrects the synthetic input trace reasonably well for minimum-phase rotation and dispersion. Although there is no phase rotation associated with the deconvolved synthetic data, real data may have a phase

rotation if the amplitude spectrum has been multiplied by a constant as previously explained.

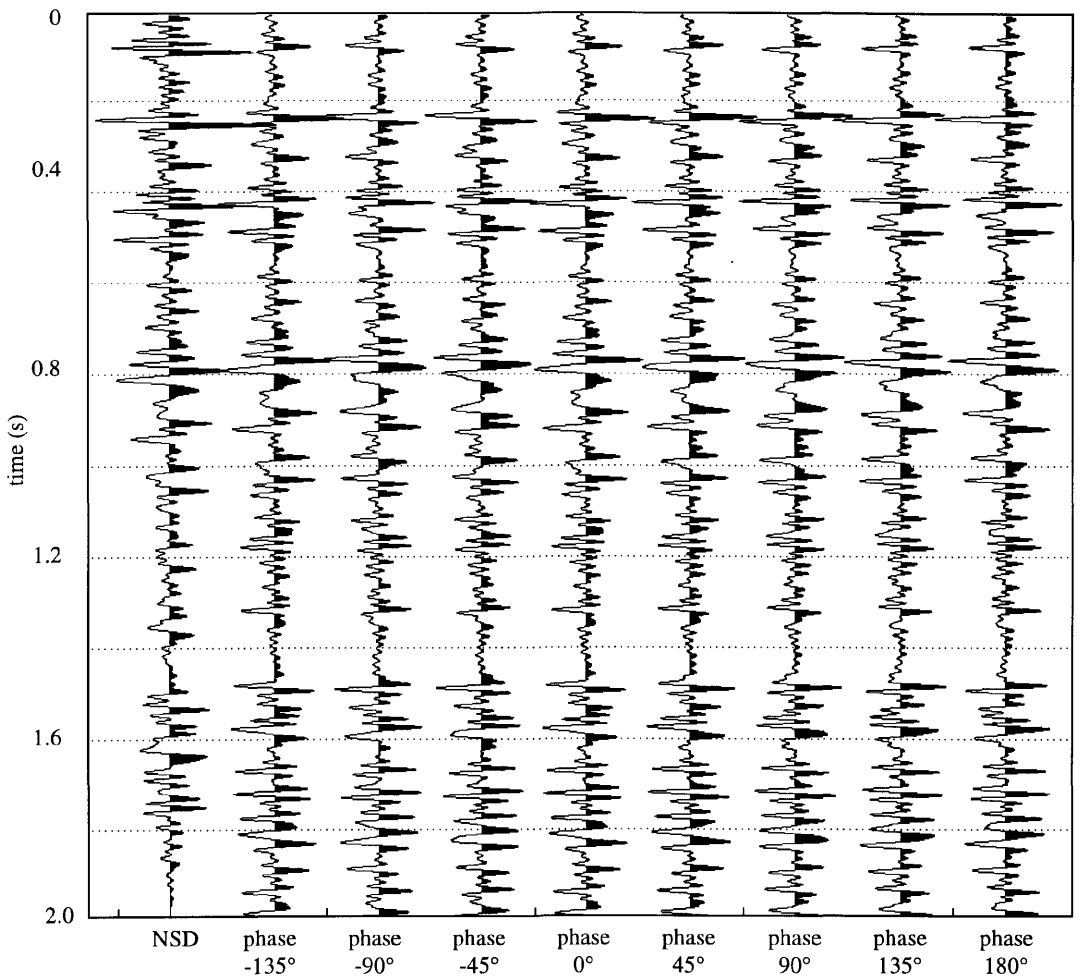

Figure 4.29: Comparison of minimum-phase residual-smoothing NSD to bandlimited reflectivity that has been phase rotated from -135 to 180 °.

4.10 Comparison of how finite numerical precision affects NSD

The NSD inversion procedure is limited by the finite numerical precision of the computing facilities, as explained in Section 4.1. Frequencies that have decayed beyond a certain limit are irretrievably lost. A test has been performed to examine how finite numerical precision affects minimum-phase residual-smoothing NSD.

Three synthetic traces were created with different Q values, 12.5, 25, and 50. These three traces were deconvolved with NSD (using the correct estimate of Q) and the output traces compared to the input trace and bandlimited reflectivity in Figure 4.30. The |TVS| are compared in Figure 4.31. Constant Q attenuation is dependent on t, f and Q ($e^{-\pi tf/Q}$). Therefore, if finite numerical precision is a problem, it should be manifest itself on each trace and |TVS| at the same ratio of t, f and Q.

The results from the three different Q values, shown in Figure 4.30, each show a lack of high frequency content after certain times. It is difficult to tell if these times are roughly multiples of each other, as predicted. The trace corresponding to Q=12.5 compares well to the bandlimited reflectivity only at very early times, approximately 0.3s. The trace corresponding to Q of 25 compares well to approximately 0.8s and after this time, it seems to have a low frequency appearance. The trace corresponding to Q of 50 seems to correspond to the bandlimited reflectivity well until late times.

The |TVS| of each output trace, (Figure 4.31) shows a diagonal distinction which separates the early area of the |TVS| which has power, from the later area of the |TVS|

that seems to be lacking power. The diagonal line has been roughly drawn on each |TVS| and occurs earlier for |TVS| of lower Q values. NSD seems unable to compensate for values attenuated past some unspecified threshold perhaps because of finite numerical precision.

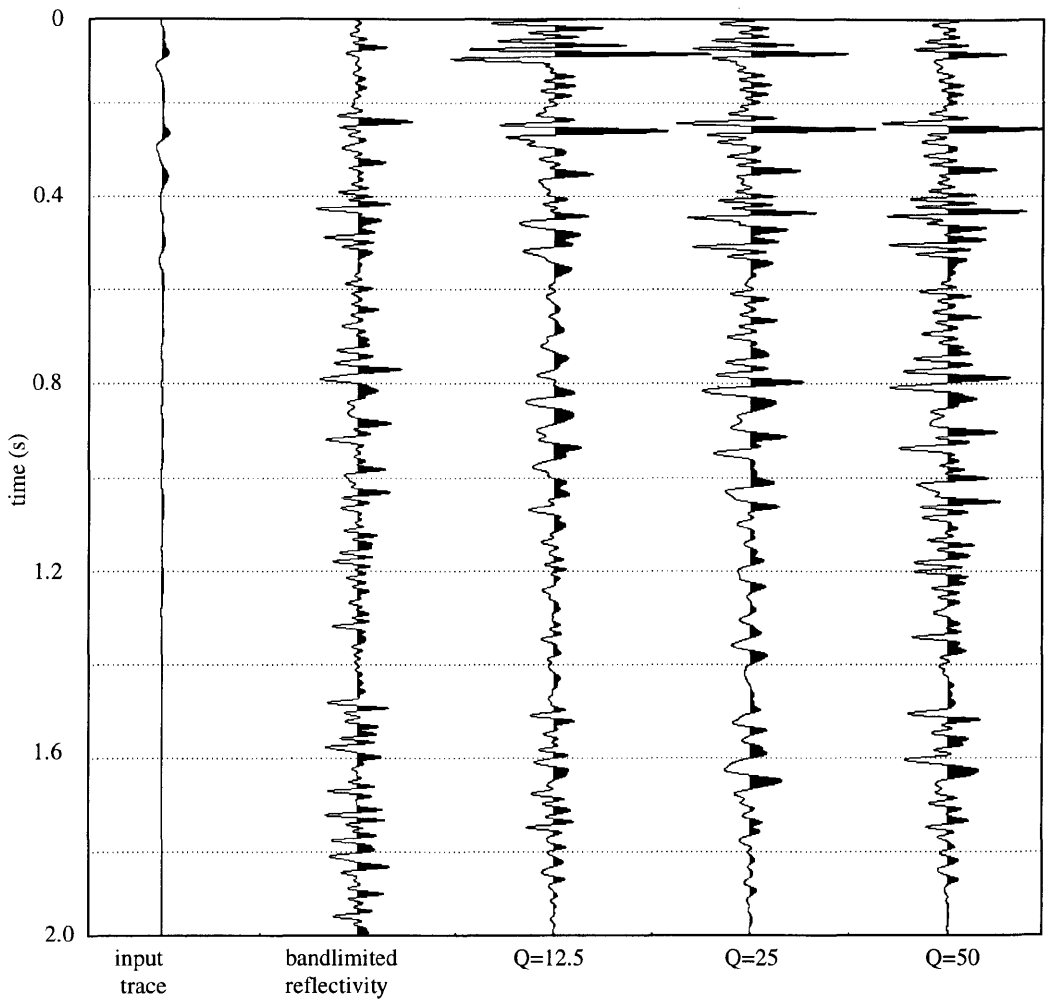

Figure 4.30: Comparison of traces created with different values of Q and deconvolved with minimum-phase residual smoothing NSD.

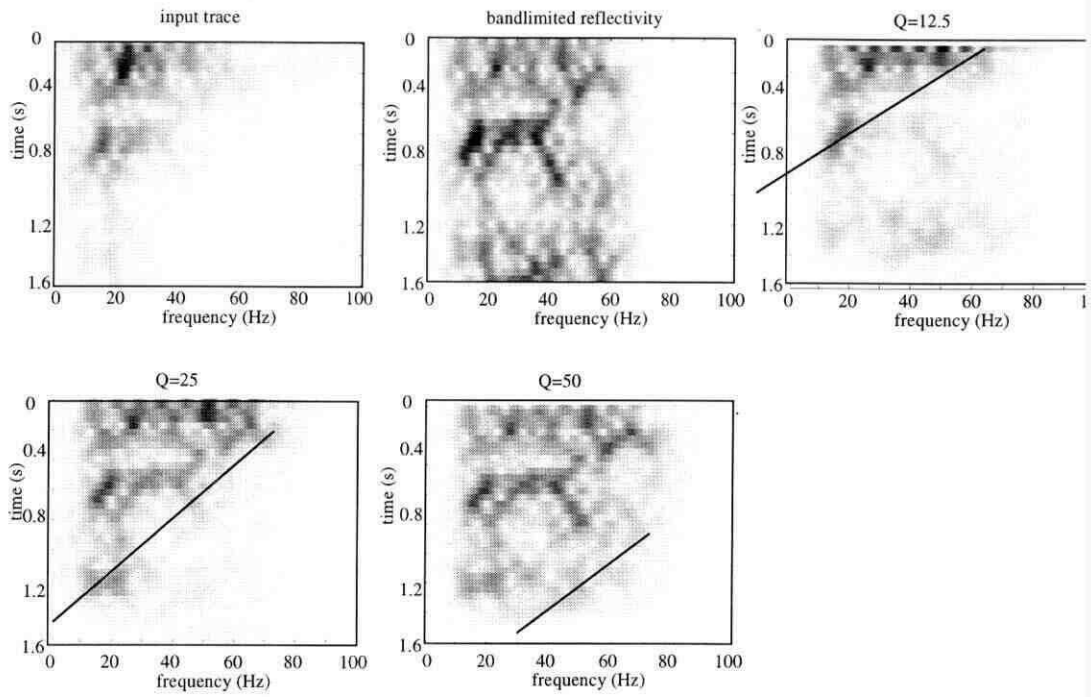

Figure 4.31: |TVS| of trace in Figure 4.30.

4.11 Chapter 4 summary

Various parameters in NSD have been tested in this chapter. Reasonable default parameters have been ascertained based on these examples. The sensitivity of NSD has been investigated with respect to time and frequency smoother lengths, smoother geometry, errors in the estimate of Q, window length and window increment in the calculation of |TVS|, and exponential gain constant. Table 4.1 shows default parameters for parameters where defaults can be chosen.

Table 4.1: Default parameters chosen for NSD

parameter	default parameter
frequency smoother length (Hz)	5
time smoother length- simple smoothing (s)	0.5
time smoother length- residual smoothing (s)	1
window length (s)	0.2
window increment (s)	0.04
window geometry	Hanning

NSD seems to be more sensitive to the length of the time smoother than the frequency smoother. Intermediate time smoothers, such as 0.5s or 1.0s, work best for the simple-smoothing method and long time smoothers, such as 1.0s or 1.5s, work best for the residual-smoothing method. Short frequency smoothers work best for both methods. An intermediate length time smoother is a smoother that is similar in length or slightly longer than the reflectivity packages. A reflectivity package is a time zone of similar reflectivity character. A long time smoother is considerably longer than the reflectivity packages.

Hanning smoothers were found to give superior results as compared to boxcar smoothers. Although, the test was biased because an optimal length had not been determined for the boxcar smoothers. The Hanning smoother may have performed better

because its Fourier transform has smaller sidelobes and greater dynamic range than the Fourier transform of the boxcar smoother. The simple-smoothing method was more sensitive to changes in smoother geometry than the residual-smoothing method.

Residual-smoothing NSD performs best when the correct value of Q is used although, when erroneous values of Q are used in residual-smoothing NSD, the results are similar to results from NSD with the correct value of Q. As Q is difficult to estimate in practice, the 'forgiving' nature of NSD with respect to Q is a strength of the method. NSD provides better results with a Q value estimated to be too high, rather than too low by the same amount.

The window length in the |TVS| calculation had a strong effect on the results from NSD. Window length determines the time and frequency resolution of the |TVS|. A relatively short window length of 0.2s was found to be suitable for this example.

Window increment in the |TVS| calculation is another important parameter in NSD. The window increment affects the time sample rate of the |TVS|. The window increment must be short enough to reduce aliassing in the |TVS|, however if it is too short the run time of the |TVS| calculation will be very long. In addition, the window increment must be shorter than the window length to avoid gaps in the spectral measurements. A window increment of 0.04s, which corresponds to an overlap of 80% between windows provides good results.

The trace input to NSD is gained before deconvolution to help reduce aliassing. The gain should be determined visually to balance the amplitudes of the trace.

Four versions of NSD (minimum-phase and zero phase, residual-smoothing and simple-smoothing) have been compared to TVSW and a combination of gain and Wiener deconvolution. Minimum-phase residual smoothing seems to provide the best result from the deconvolution methods investigated here. The success of the minimum-phase residual-smoothing version of NSD is related to the physical model on which the operator is designed, as well as the data-driven nature of the operator.

Minimum-phase residual-smoothing NSD has been compared to a bandlimited reflectivity trace with constant phase rotation. This version of NSD seems to produce a zero-phase deconvolved trace on synthetic data. Real data may have a constant phase rotation after deconvolution as described in Section 4.9.

Finally, an investigation was made of the effects of finite numerical precision on the results from NSD. NSD may be unable to compensate for extreme attenuation. Since constant Q attenuation is dependent on ft/Q, NSD may be ineffective at low Q values and moderate Q values at later times.

CHAPTER 5: EXAMPLES

5.1 Introduction

NSD has been applied to the Blackfoot broadband survey to test performance on real data. The Blackfoot broadband 2D survey was acquired in 1995 over the Blackfoot Field near Strathmore, Alberta. The target in this area is glauconitic channel sands, up to 35m in thickness, deposited in the Lower Cretaceous as incised valley fill (Stewart et al., 1996). The channel sands overlie carbonates of Mississippian age. The processing goal is to delineate the channel boundaries and image the target.

First, optimal parameters for NSD for the Blackfoot broadband dataset were determined. Some of the parameters have been determined already in Chapter 3. Other parameters however, such as time and frequency smoother lengths, stab factor, phase of operator, and method of smoothing must be determined specifically for this dataset. These parameters are determined by varying them and then comparing the results to synthetic seismograms. The parameter valuess that give the result best matching the synthetic seismogram are chosen for and used in NSD for this dataset.

After the parameters have been determined the data was processed. The data was processed several times, as described in Section 5.1.1 to allow for several comparisons. In Section 5.3, a dataset deconvolved with gain and Wiener deconvolution will be compared to a dataset deconvolved with Wiener deconvolution and inverse-Q filtering, and a dataset deconvolved with NSD. In Section 5.4, trace-by-trace NSD is compared

with profile-mode NSD and fx-NSD. The comparisons of the deconvolved data will involve:

1. entire stacked datasets

2. average |TVS| of datasets

3. comparison of the area thought to contain the channel

4. comparison of deconvolved traces to the synthetic seismograms of 14-09 and 4-16

5.1.1 Processing the Blackfoot Broadband survey

All examples in this chapter have been created with basically the same processing flow. Variations have been made to this basic flow only to accommodate different deconvolutions: Flow 1 is the NSD flow, Flow 2 is the Wiener deconvolution flow and Flow 3 includes Wiener deconvolution and inverse-Q filtering. NSD is applied separately in all forms: trace-by-trace NSD, profile-mode NSD, and fx-NSD. Therefore, five different datasets will result.

An estimate of Q is required for NSD and inverse-Q filtering. This estimate was calculated to be 100 with the spectral ratio method, described in Section 1.6. This Q value seems consistent with the lithology of the region (sands, shales, dolomites and limestones) based on Table 1.1.

NSD was applied post-stack for computational ease. This is acceptable because constant-Q attenuation is expected to be midpoint consistent based the surface-consistent model of Section 1.7. Therefore NSD can be applied to data stacked by common midpoint. Wiener deconvolution and inverse-Q filtering were also applied post-stack to provide a fair comparison with NSD.

Below is a description of the processing flow. Each processing technique was applied to every dataset unless specified otherwise.

1. *mute* A top mute was applied first to the shot records to remove the refracted arrivals and near surface noise.

2. *spherical divergence corrections* This is a correction of energy loss due to an expanding spherical wavefront as described in Section 1.3. These corrections were based on a function of time and velocity ($(tv)^{-2}$).

3. *gain* (Flows 1 and 2) A gain correction of 6dB/s was applied to the Wiener deconvolution dataset and the NSD dataset. The gain will be removed from the NSD dataset during the NSD process. Gain was not applied to the dataset that was inverse-Q filtered.

4. *elevation statics* These correct for the effects of topography and move the shot and receiver locations to a level datum (Yilmaz,1987). The datum was chosen to be 965m and the replacement velocity is 2500m/s.

5. *residual statics* These static corrections are for velocity variations in the near surface. Correlation autostatics were used in all of the processing flows.

6. *bandpass filter* A zero-phase Ormsby bandpass filter of 8-12-90-120 Hz was applied to the datasets.

7. *normal moveout (NMO) correction* Normal moveout refers to the time difference between a reflector on a non-zero offset trace and the same reflector on a zero offset trace. Normal moveout must be eliminated before stacking (Sheriff and Geldart, 1995).

8. *stack* The traces are sorted by common midpoint and averaged. This increases the signal to noise ratio.

9. *NSD* (Flow 1) The minimum-phase residual-smoothing version of NSD with a 1.0s time smoother and a 10 Hz frequency smoother was applied. A stabilization factor of 0.01 was used in the algorithm. A time-variant filter with a high cut of 160 Hz at 0s and 70 Hz at 2s was applied to the NSD datasets. A Q value of 100 was used in the NSD algorithm.

10. *Wiener deconvolution* (Flows 2 and 3). A minimum-phase Wiener deconvolution was applied to one of the datasets. An operator of 100ms in length and 0.01 stabilization factor was used. The operator was designed on the time zone of 500-1500ms. Again, these parameters were chosen to be consistent with NSD.

11. *inverse-Q filtering* (Flow 3) This is Promax's Q compensation algorithm which is based on Hale's algorithm (1982). Inverse-Q filtering was applied to only one dataset. A Q value of 100 was used for all traces at all times.

12. *trace equalization* This is a trace to trace amplitude balancing function. A scalar is applied to the entire trace.

13. *FX spatial prediction* In this processing technique, the traces are Fourier transformed and then a prediction filter is applied spatially to reduce noise. A Wiener-Levinson algorithm was used with 0% white noise, a spatial operator of 60 traces, and 5 samples in the prediction filter. The windows are 300ms in length with a 30ms overlap. Frequencies below 5Hz and above 160Hz were attenuated.

14. *phase shift migration* Migration involves repositioning data elements to make their locations appropriate to the locations of the associated reflectors and diffracting points (Sheriff and Geldart, 1995). Phase shift migration is a downward continuation in the frequency domain. The data was migrated from CDP 260 to CDP 550 to avoid end effects. Frequencies of 0 to 160 Hz were migrated.

15. *automatic gain control* (Flow 2) This was applied to the dataset with gain and Wiener deconvolution only for display purposes. Automatic gain control is a time-variant gain. It is computed by applying a window to a trace and calculating a scale factor for that window based on the mean amplitudes in the window. The scale factor is then applied to

the center sample. The window is then incremented along the trace. A 500 ms gate was used in the gain and Wiener deconvolution flow in these examples.

5.2 Determination of parameters for the Blackfoot broadband survey

Two wells near the Blackfoot broadband survey containing sonic and density logs, 14-09-023-23W4 and 4-16-023-23W4, allow for the construction of synthetic seismograms. Figure 5.1 is a map showing the location of the two wells in relation to the line. The two wells are pointed out in Figure 5.1 by arrows.

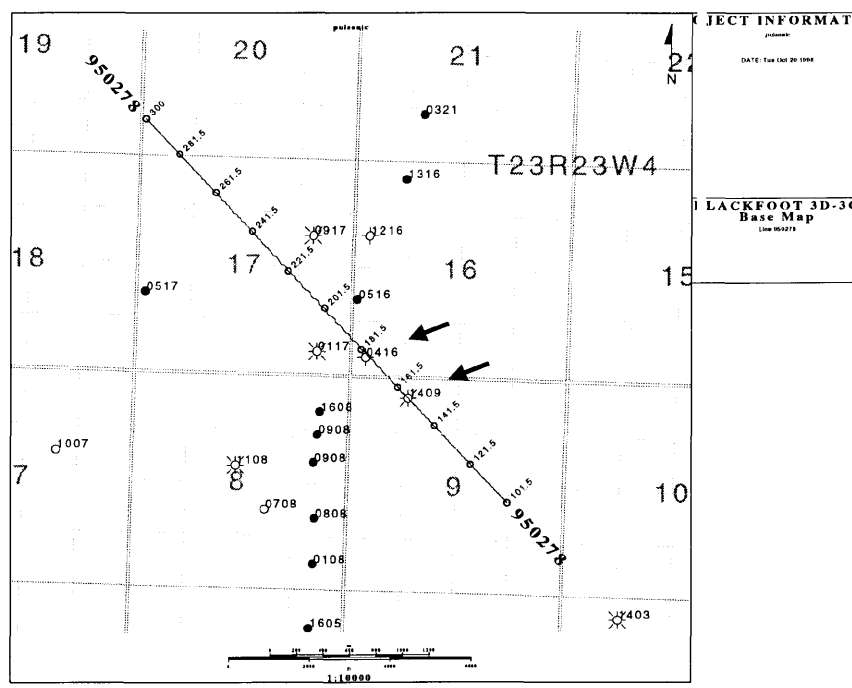

Figure 5.1: A map showing the location of 14-09 and 4-16 in relation to the Blackfoot broadband survey. Arrows in the figure point out the two wells.

Synthetic seismograms are a type of forward modeling based on the convolutional model of Equation (1.21). Sonic and density logs provide the information needed to construct a reflectivity estimate. Once the reflectivity is estimated, a wavelet can be convolved with the reflectivity series to compute the simplest type of synthetic seismogram. Synthetic seismograms in these examples are one-dimensional and do not contain multiple effects. The layers are assumed to be horizontal and the raypaths are assumed to be vertical (and therefore normally incident on the reflectors). In addition, diffractions and other wave modes are ignored. The wavelet used in the 4-16 synthetic seismogram is an Ormsby wavelet with corner frequencies of 8-12-90-110 Hz and the wavelet for the 14-09 synthetic seismogram is an Ormsby wavelet of corner frequencies 8-12-75-90 Hz.

Real seismic data may be different than the synthetic seismogram for several reasons. One reason is the approximations used in the calculation, as discussed above. Also, seismic wavelengths are so much longer than the distances over which the acoustic properties can be assumed to be constant and therefore the actual seismic waveform is the interference composite of many small events (Telford et. al. 1990). In addition, the sonic log used to calculate the reflectivity is also subject to errors (Telford et. al, 1990).

The frequencies used in sonic logs are on the order of 10's of KHz and are therefore much higher than the frequencies of seismic data (Waters, 1992). There is a time delay between two pulses propagating with two different frequencies (Stewart, 1983). Therefore synthetic seismograms must be stretched and shifted to match seismic

data. The 4-16 sonic log has been check-shot corrected to reduce the time delay between synthetic seismograms and seismic data. A check-shot survey is a survey with a sonde in the well and a seismic source at the surface (Waters, 1992). It records velocities down the well and can be used to attempt to correct a sonic log to seismic velocities.

Parameter testing must be performed to determine optimal parameters for NSD as applied to the Blackfoot broadband dataset. Some of the parameters determined in Chapter 3 will be used. The window length for the |TVS| calculation is 0.2s and the window increment is 0.04s. Hanning smoothers are used. The gain was determined to be $0.6908s^{-1}$. Other parameters, such as type of smoothing (residual or simple), phase of the NSD operator, time and frequency smoother lengths, and stab factor will be determined through testing. The tests will include:

1) comparison of zero-phase residual-smoothing, minimum-phase residual-smoothing, zero-phase simple-smoothing and minimum-phase simple-smoothing

2) time and frequency smoother lengths were tested for the minimum-phase residual-smoothing method.

3) constant phase rotations of the synthetic seismograms compared to the minimum-phase residual-smoothing result

4) stab factor for the minimum-phase residual-smoothing version

The comparisons in this section will be done only with a zoomed section of the synthetic seismogram created from the logs of the 4-16 well. This is because the 4-16 synthetic seismogram ties to the seismic data better. The zoomed section is 0.8s to 1.1s and includes the target area. Ten seismic traces centered at the well location of 4-16 are displayed in each figure and compared to the synthetic seismogram. The synthetic has been rotated by a constant phase rotation of 90° (this constant phase rotation is shown to provide the best tie to the deconvolved datasets in Section 5.2.3).

5.2.1 Method of smoothing and operator phase

Figure 5.2 shows a parameter test comparing the minimum-phase residual-smoothing version with the zero-phase simple-smoothing version, zero-phase residual-smoothing version and minimum-phase simple-smoothing version. The minimum-phase residual-smoothing version matches the synthetic seismogram most closely. For example, the trough doublet at 0.92s on the synthetic seismogram (pointed out by an arrow on Figure 5.2) is most closely reproduced by the result from minimum-phase residual-smoothing NSD. The zero phase versions look similar to each other. These results match with theory and the results of tests on synthetic data in Chapter 4.

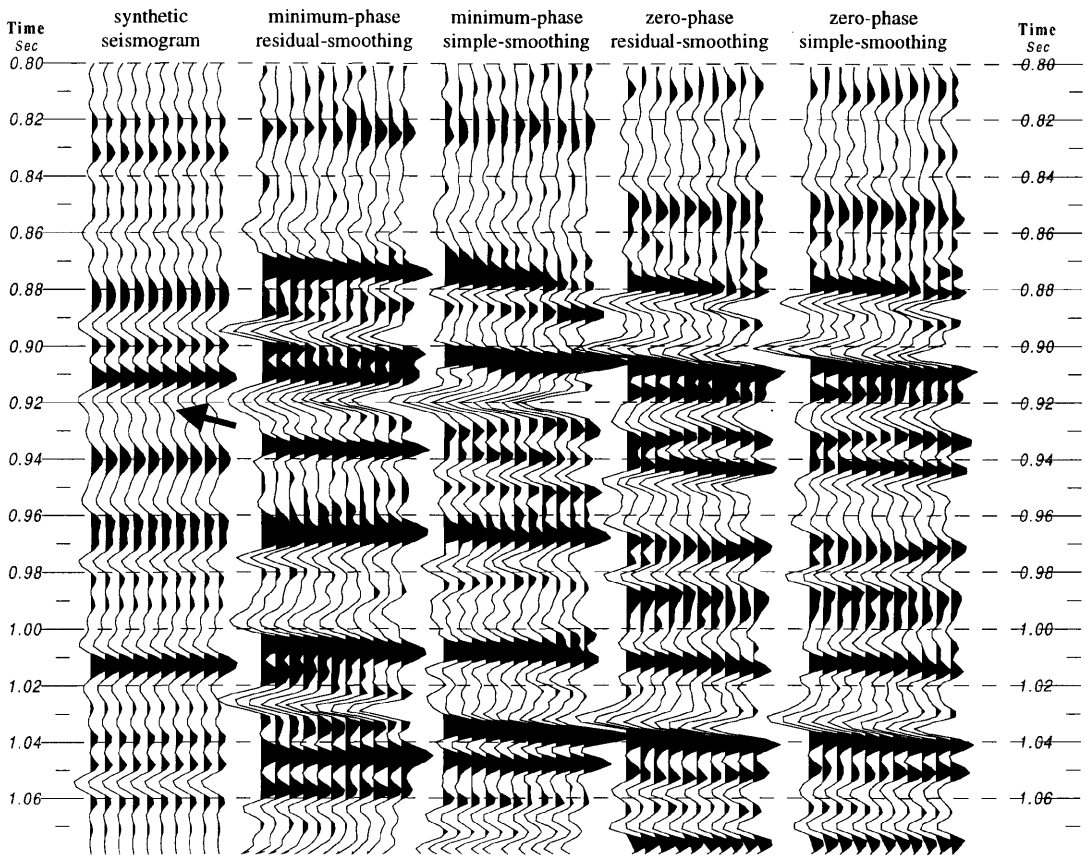

Figure 5.2: A comparison of the 4-16 synthetic seismogram to results from minimum-phase residual-smoothing NSD, minimum-phase simple-smoothing NSD, zero-phase residual-smoothing NSD and zero-phase simple-smoothing NSD. The arrow points to a section of the synthetic seismogram that is best reproduced by the minimum-phase residual-smoothing method.

5.2.2 Smoother lengths

Next, the lengths of the time and frequency smoothers of the minimum-phase residual-smoothing version were varied to determine their influence on the tie to the synthetic seismogram. The results are shown in Figures 5.3 and 5.4. Variation in temporal and frequency smoothers has little effect on the data. The reflectivity packages in this dataset appear to vary between 200ms and 500ms based on the stacked sections, such as Figure 5.8. Therefore the temporal smoother should be longer than 500ms. A temporal smoother of 1.0s and frequency smoother of 10 Hz will be used based on the duration of the reflectivity packages, theory and the conclusions of Chapter 3.

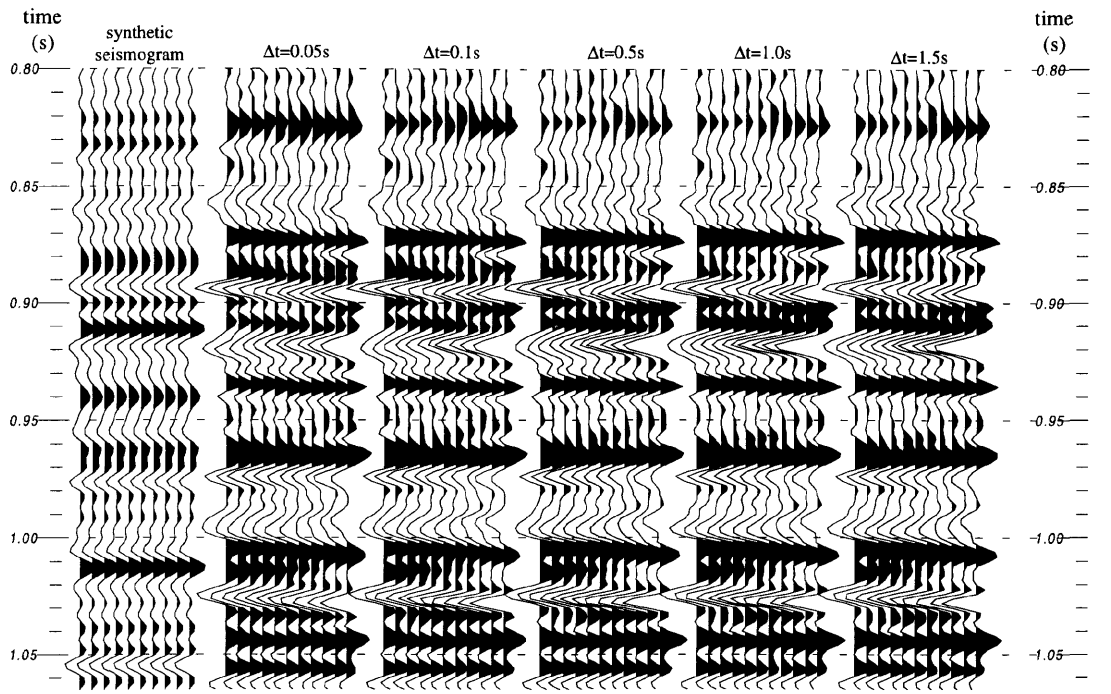

Figure 5.3: The time smoother of the minimum-phase residual-smoothing method was varied from 0.05s to 1.5s and compared to the synthetic seismogram from the 4-16 well. The frequency smoother was held constant at 10 Hz.

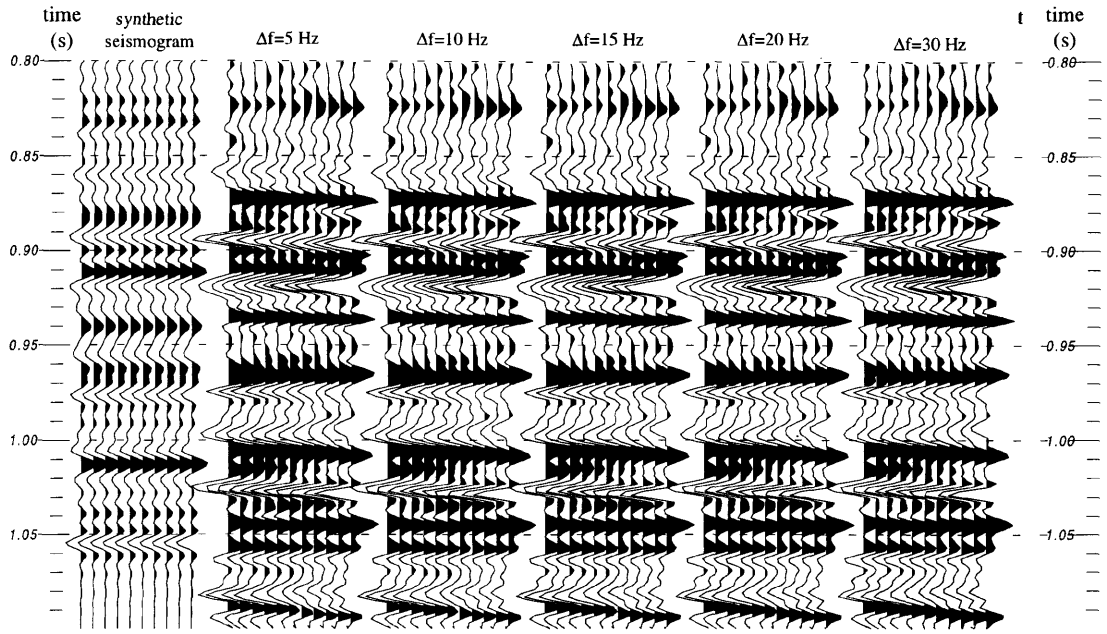

Figure 5.4: The frequency smoother in the minimum-phase residual-smoothing method was varied from 5 Hz to 30 Hz and compared to the synthetic seismogram from the 4-16 well. The time smoother was held constant at 1.0s.

5.2.3 Phase of synthetic seismograms

The Ormsby wavelet used in the creation of the synthetic seismogram was rotated from 0° to 180° through constant rotations of 45° increments to determine if a phase shift is present in the NSD deconvolved section. The rotated seismograms and NSD result are shown in Figure 5.5. The synthetic seismogram created with a 90° rotated Ormsby wavelet ties best to the section of the minimum-phase residual-smoothing version of NSD shown. For example, the trough at 0.93s and the time zone between 0.98s to 1.01s

(pointed out by arrows in Figure 5.5) on the minimum-phase residual-smoothing method are best matched by the synthetic seismogram rotated by a constant 90°. The phase rotation is a result of a constant multiplied with the amplitude spectrum of the seismic data as described in Section 1.8.4 and Section 4.10. The nature of the constant multiplier is unknown.

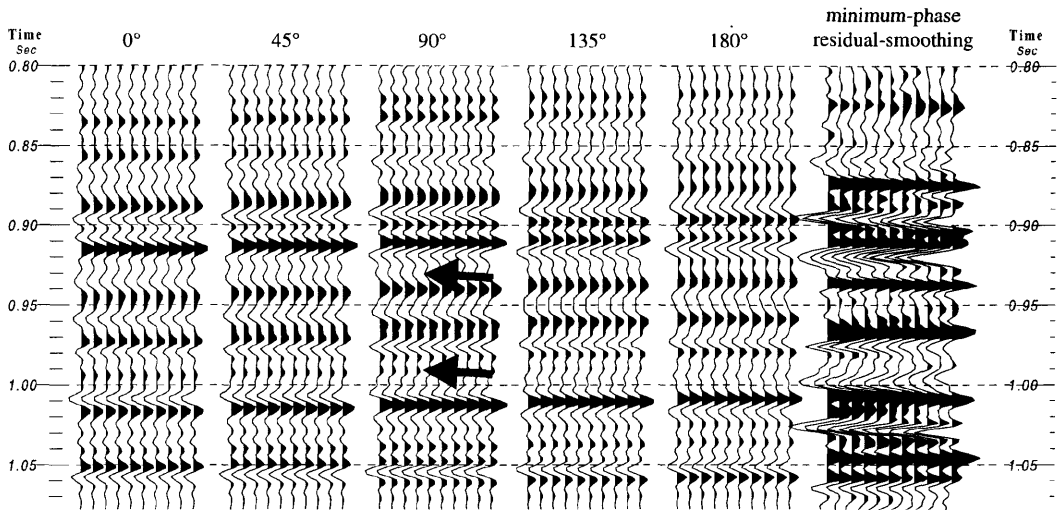

Figure 5.5: The synthetic seismogram is rotated through constant phase rotations from 0 to 180° with 45° increments. The synthetic seismogram rotated by 90° seems to best match the result from minimum-phase residual-smoothing NSD.

5.2.4 Variation of stab factor

In the NSD algorithm a small constant needs to be added to a matrix in certain equations for stability. It is added to the Q/gain surface before it is inverted (Equation

3.10) and to the forward operator before the minimum-phase calculation and inversion (Equation 3.14). The small constant is the maximum value of the Q/gain surface or |TVS| multiplied by some number called the stability factor, which is typically between 10^{-7} and 10^{-1}. The stability factor must be chosen so that it is small enough to avoid significantly altering the quantity that it is added to, but it must be large enough to prevent an operation from becoming unstable. The stability factor is most crucial in real data when low values in the |TVS| become dominated by noise.

The stab factor was varied from 10^{-1} to 10^{-6} to determine how it affects the results, which are shown in Figure 5.6. The results with stab of 10^{-2}, 10^{-3}, 10^{-4}, and 10^{-5} seem strongly similar. The result with stab of 10^{-1} looks worse in comparison to the synthetic seismogram than the others results. A stab factor of 0.1 is too large and is affecting the numerical values of the operator. A stab factor of 10^{-2} will be used in the examples of this chapter.

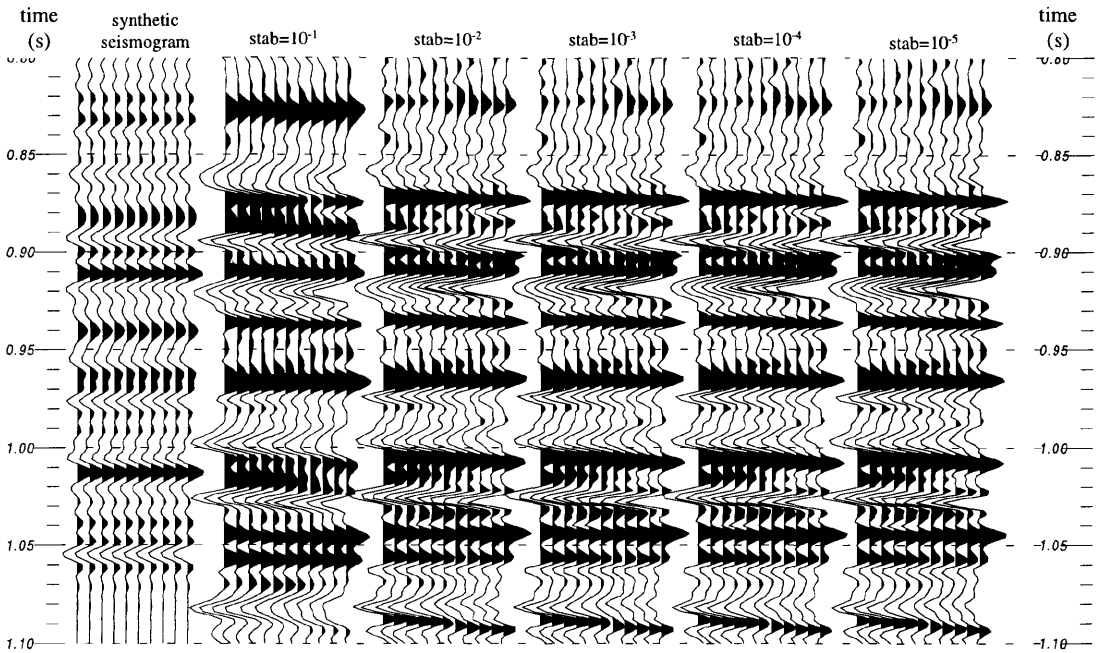

Figure 5.6: The stab factor was varied from 10^{-1} to 10^{-5} in the minimum-phase residual-smoothing result.

5.2.5 *Conclusions from parameter testing*

Based on the tests of this section, the minimum-phase residual-smoothing version of NSD provides a good comparison to the synthetic seismogram. In addition, a time smoother of 1.0s, a frequency smoother of 10 Hz and a stab factor of 10^{-2} also provide reasonable results. These parameters will be used in the remaining examples.

5.3 Comparison of NSD to other deconvolution techniques

In this section, the results from profile-mode NSD will be compared to results from a combination of gain and Wiener deconvolution, and Wiener deconvolution and inverse-Q filtering. Figure 5.7 shows the stacked data set after pre-stack processing without application of any deconvolution. The stack with gain and Wiener deconvolution applied to it is shown in Figure 5.8. The stack with Wiener deconvolution and inverse-Q filtering is shown in Figure 5.9, and the stack with profile-mode NSD is shown in Figure 5.10. Figure 5.11 shows an average |TVS| for each stacked section. The average |TVS| were calculated by averaging the |TVS| of traces 50 to 100. A zoom of the area thought to contain the channel of each of the three stacks is shown in Figure 5.12 and a comparison of the datasets to the synthetic seismograms is shown in Figures 5.13 and 5.14.

All deconvolved sections show increased resolution as compared to the stack before post-stack processing (Figure 5.7). The stacked section with post-stack NSD deconvolution seems to be of better resolution than the other two sections, although comparison is difficult at this scale. The reflectors in the 1300 to 1600 ms time zone seem to be more resolved on the NSD section.

The average |TVS| are shown in Figure 5.11. In these grey level plots, white is zero and black is a large positive number. The average |TVS| of the sections processed with gain and Wiener deconvolution, and Wiener deconvolution and inverse-Q filtering are dominated by two separate high amplitude areas. In addition, both average |TVS| are

lacking high frequencies at later times. In contrast, the average |TVS| of the NSD result is more even and consistent. The bandwidth is approximately 10 to 110 Hz.

As stated previously, the target in this area is channel sands. Figure 5.12 focuses in on the area of each of the deconvolved sections thought to contain the target. The geological feature thought to be the channel is pointed out with arrows. The channel is difficult to discern on the section deconvolved with post-stack Wiener deconvolution and on the section that had Wiener deconvolution and inverse-Q filter applied to it. The section with NSD shows the best image of the target. The channel in the NSD section is outlined by the underlying Mississippian carbonates. In addition there is an internal marker in the channel sands at approximately 1060ms in the NSD section that stands out clearly. This internal marker is absent in the other sections. The vertical resolution of the NSD result seems improved as compared to the others.

The comparisons of the different processing flows with the 14-09 synthetic seismogram are shown in Figure 5.13. The 14-09 synthetic seismogram ties reasonably well to the seismic sections. The NSD section ties better to the synthetic seismogram at later times, such as 0.7s to 0.8s, than the other seismic sections.

The 4-16 synthetic seismogram ties more closely to the Blackfoot broadband survey, as can be seen from Figure 5.14. Again, the NSD result matches the synthetic better than the other two sections. The trough at 0.92s (shown by an arrow in the figure) on the synthetic seismogram of 4-16 is best approximated by the NSD result. The time

zone between 0.97s and 1.01s (also pointed out by an arrow) is also best matched by the NSD result.

NSD has proved effective as applied to the Blackfoot broadband survey. It enhanced the vertical resolution of the stacked section as compared to the combinations of gain and Wiener deconvolution, and Wiener deconvolution and inverse-Q filtering. In addition, the section deconvolved with NSD has improved reflectivity character as compared to the other techniques. This is evident from the close-up view of the channel (Figure 5.12) and from the ties to the synthetic seismograms (Figures 5.13 and 5.14). In addition, the average |TVS| of NSD is more even and consistent than the average |TVS| of the other methods. NSD delineated the target channel more clearly than the other processing techniques. The success of NSD as compared to the other techniques is related to the physical model on which the operator is built and its data-driven nature.

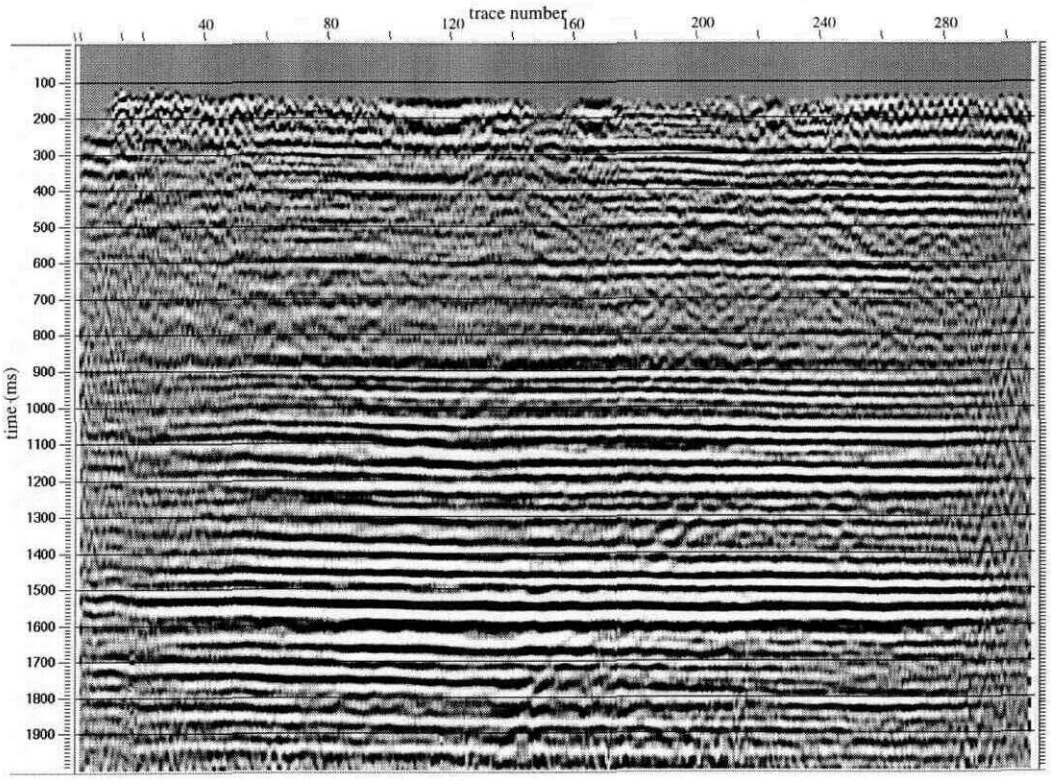

Figure 5.7: The Blackfoot broadband survey after pre-stack processing and without application of any deconvolution.

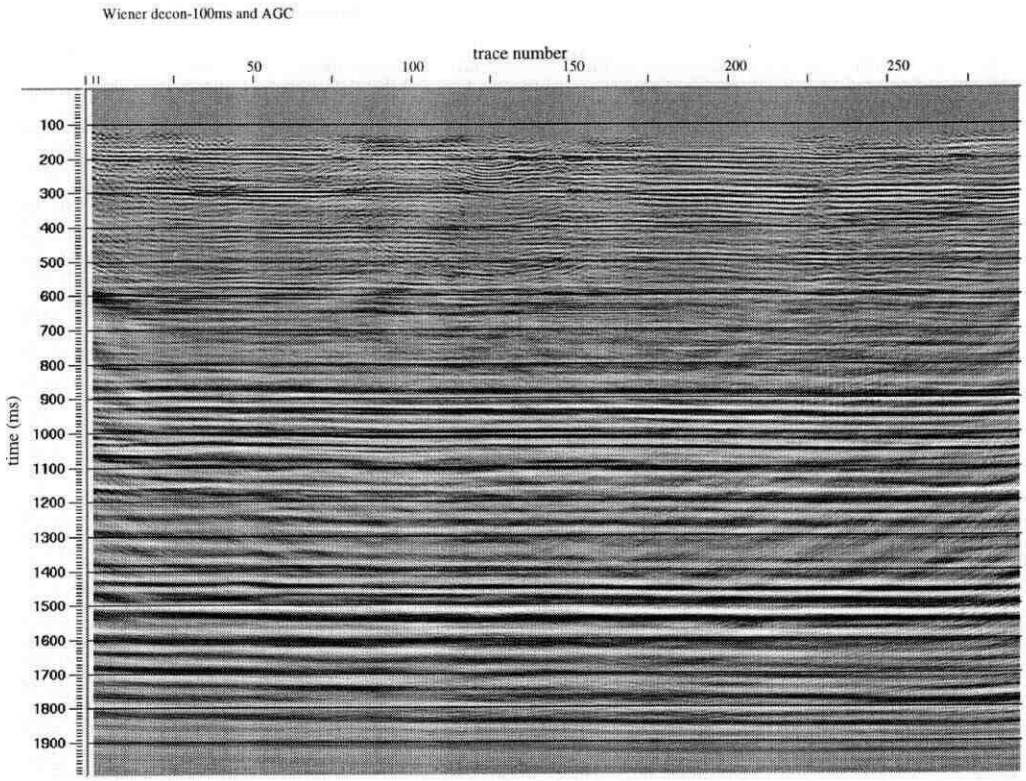

Figure 5.8: The Blackfoot broadband survey with gain and post-stack Wiener deconvolution and the complete post-stack processing described in Section 5.4.

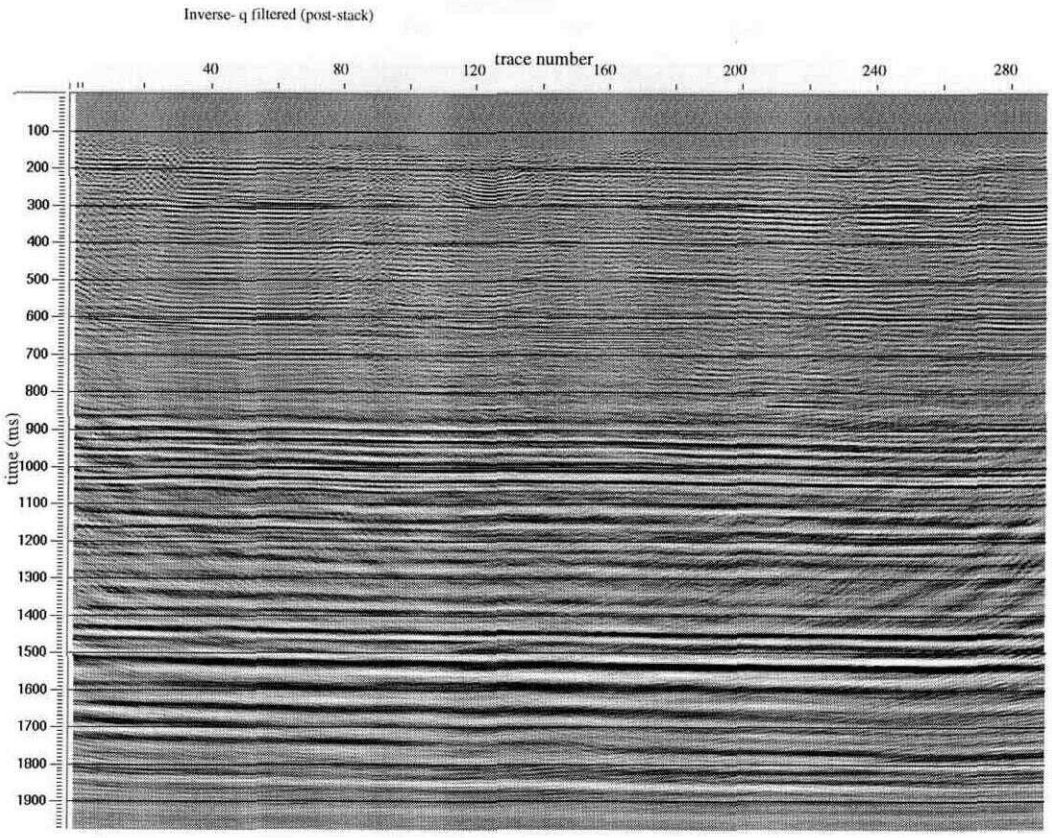

Figure 5.9: The Blackfoot broadband survey with post-stack Wiener deconvolution and post-stack inverse-Q filtering and the complete post-stack flow described in Section 5.4.

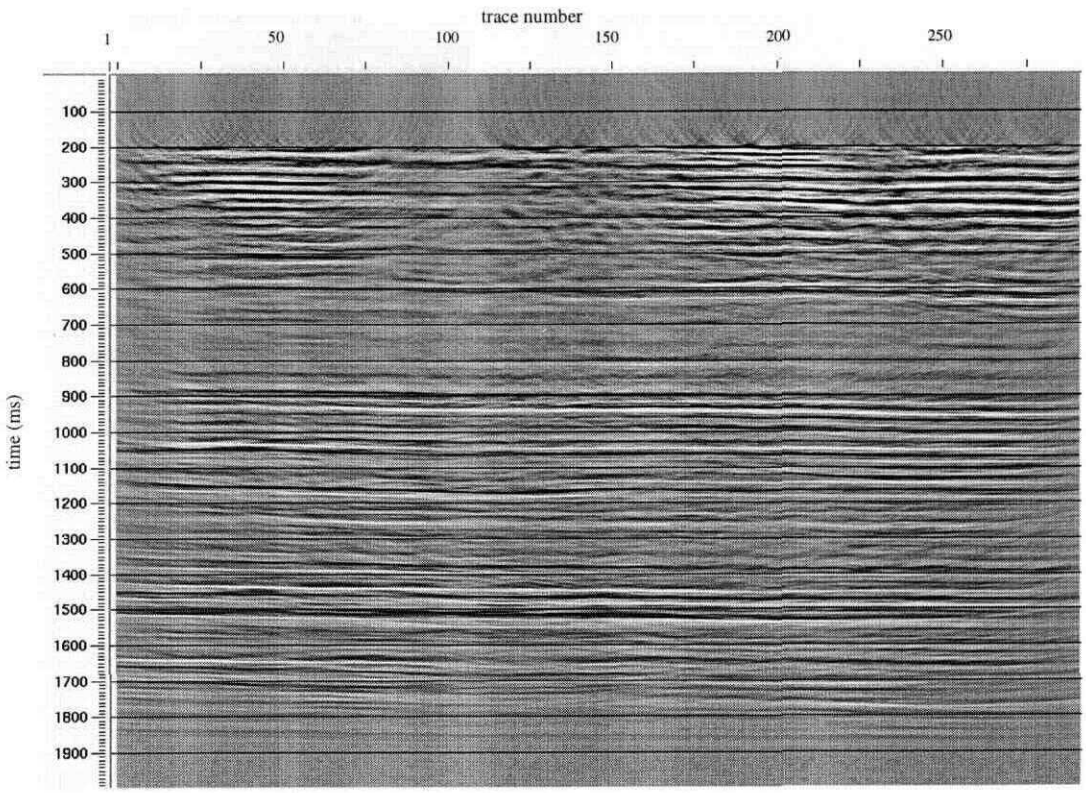

Figure 5.10: The Blackfoot broadband survey with post-stack profile-mode NSD and the complete post-stack processing as described in Section 5.4.

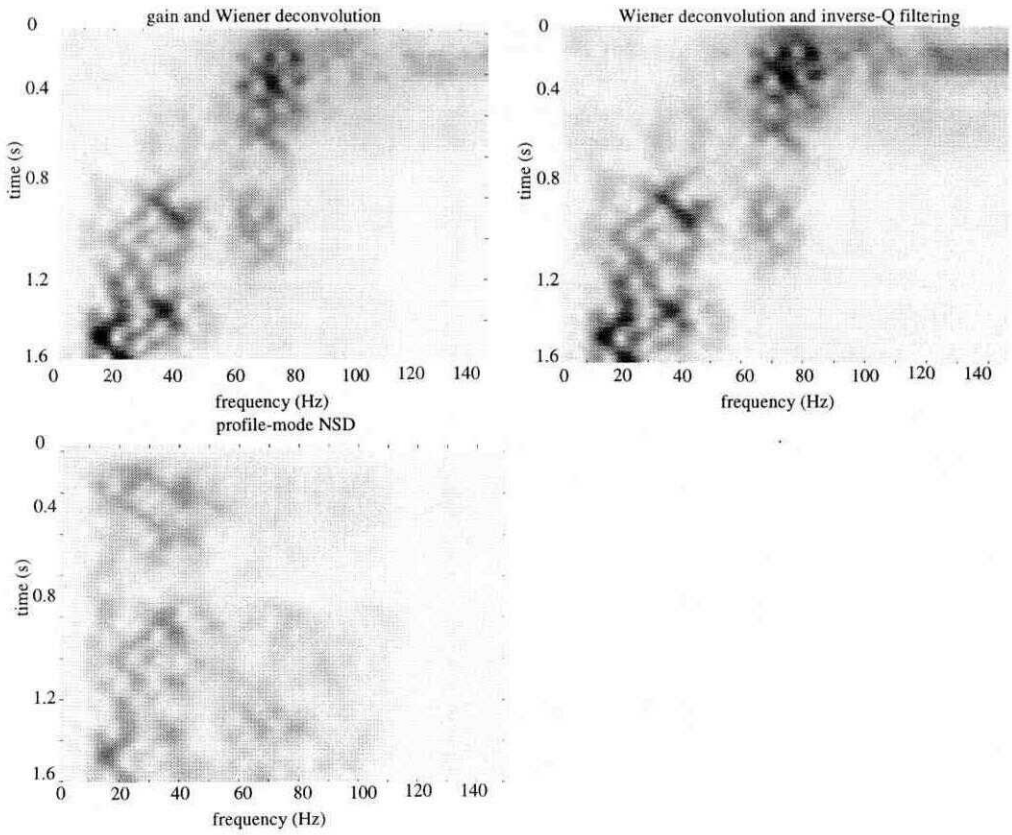

Figure 5.11: The average |TVS|, calculated by averaging the |TVS| of traces 50 to 100, of the stacked sections from Figures 5.8 to 5.10.

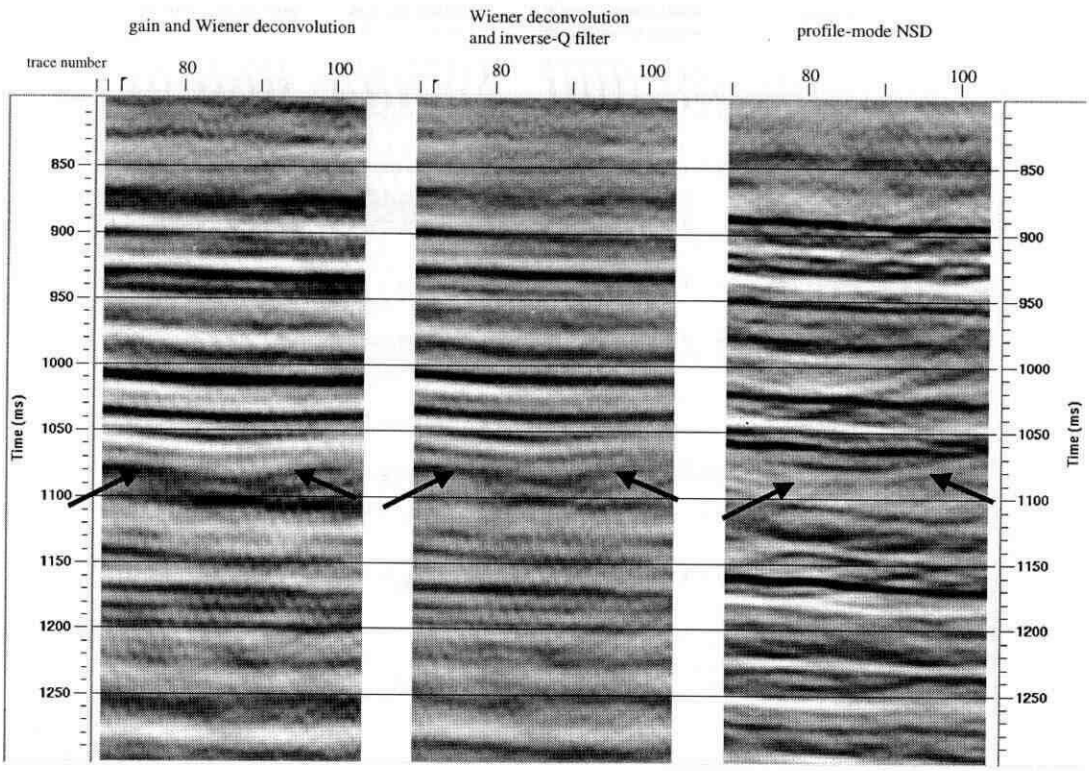

Figure 5.12: The target area of each of the deconvolved sections. The feature thought to be the channel is pointed out with arrows in the figure.

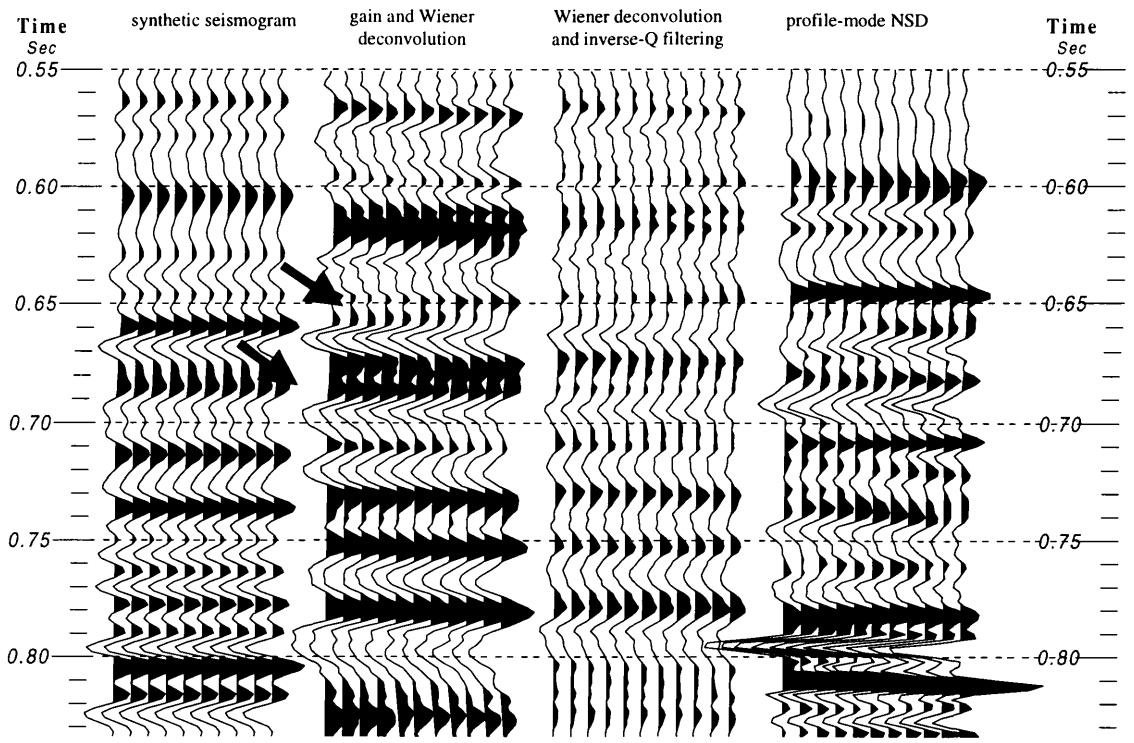

Figure 5.13: The 14-09 synthetic seismogram compared to the result from gain and post-stack Wiener deconvolution, post-stack Wiener deconvolution and post-stack inverse-Q filtering and post-stack profile-mode NSD.

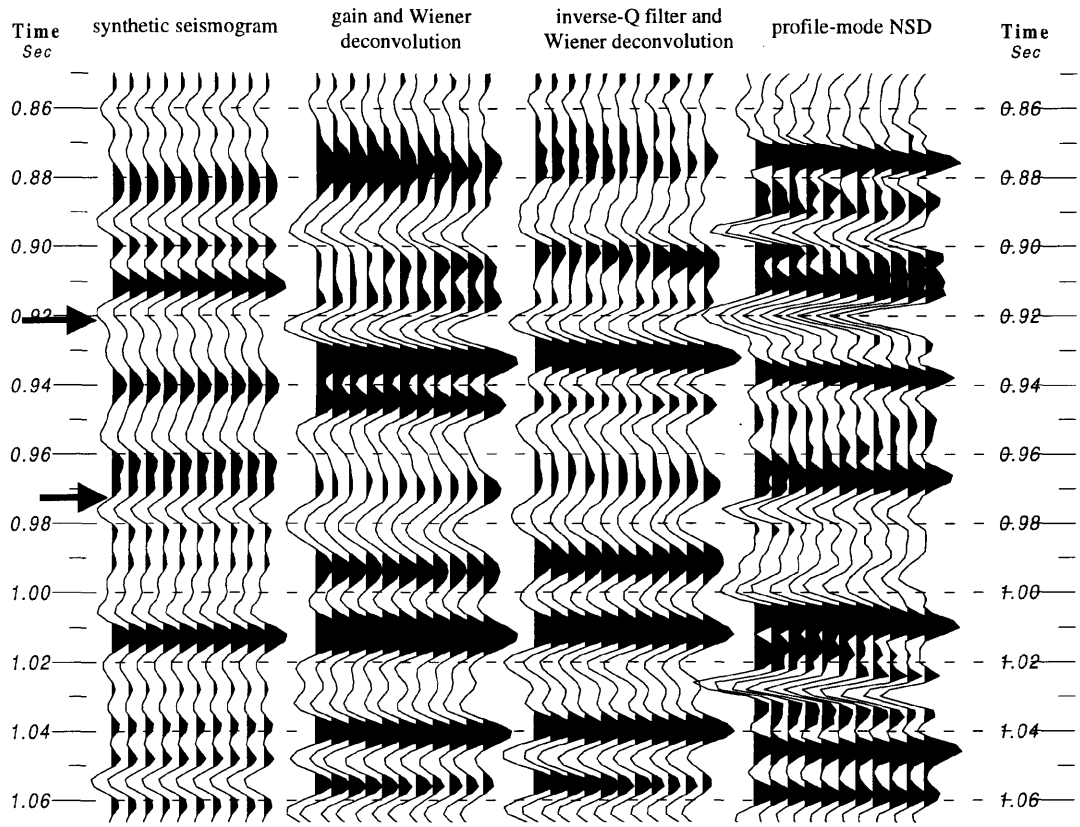

Figure 5.14: The 4-16 synthetic seismogram compared to the result from gain and post-stack Wiener deconvolution, post-stack Wiener deconvolution and post-stack inverse-Q filtering and post-stack profile-mode NSD. The arrows point to places on the synthetic seismogram that tie best with the NSD result.

5.4 Comparison of extensions of NSD

Trace-by-trace mode NSD, profile-mode NSD and fx-NSD were tested on the Blackfoot broadband survey and compared to each other. NSD was applied post-stack in

all examples, as described in Section 5.2. The parameters used for NSD are also described in Section 5.2. The full seismic sections of the Blackfoot Broadband survey processed with each version of NSD are not shown as they were indistinguishable from each other. The result from profile-mode NSD is shown in Figure 5.10. The average |TVS| created by averaging the |TVS| of traces 50 to 100, of each section deconvolved with NSD, are shown in Figure 5.15. Figure 5.16 is a comparison of a zoom of each of these sections in the area where the channel is thought to be.

The average |TVS| and the zoom of the channel look very similar for both versions of NSD. Slight differences however can be seen in the zoomed section of the comparison to synthetic seismograms in Figures 5.20 and 5.21. The reflectors in the trace-by-trace NSD result appear less consistent. For example the peak at 0.62s on Figure 13, as pointed out with an arrow, is more consistent in the profile-mode NSD and fx-NSD. This is expected because applying a single operator to an ensemble of traces will reduce trace-to-trace differences. In general, the results from both types of NSD yield similar results. The advantage of profile-mode NSD lies in statistical leverage and trace-to-trace stability. In general, the results from all three types of NSD yield similar results and no single type of NSD stands out as being clearly superior. This similarity is a strength of the method and indicates that NSD is robust. The advantages of profile-mode and fx-NSD are the reduction of trace-to-trace differences induced by the operator and statistical advantage in the operator design.

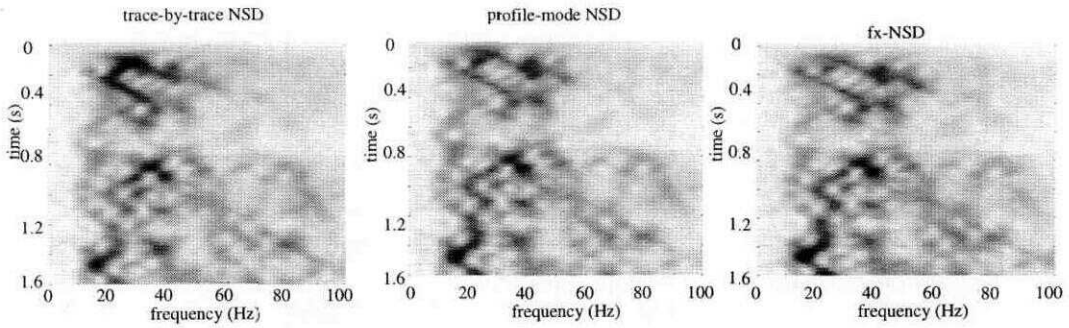

Figure 5.15: Average |TVS| of trace-by-trace NSD, profile mode NSD and fx-NSD. The average |TVS| were calculated by averaging the |TVS| of traces 50 to 100.

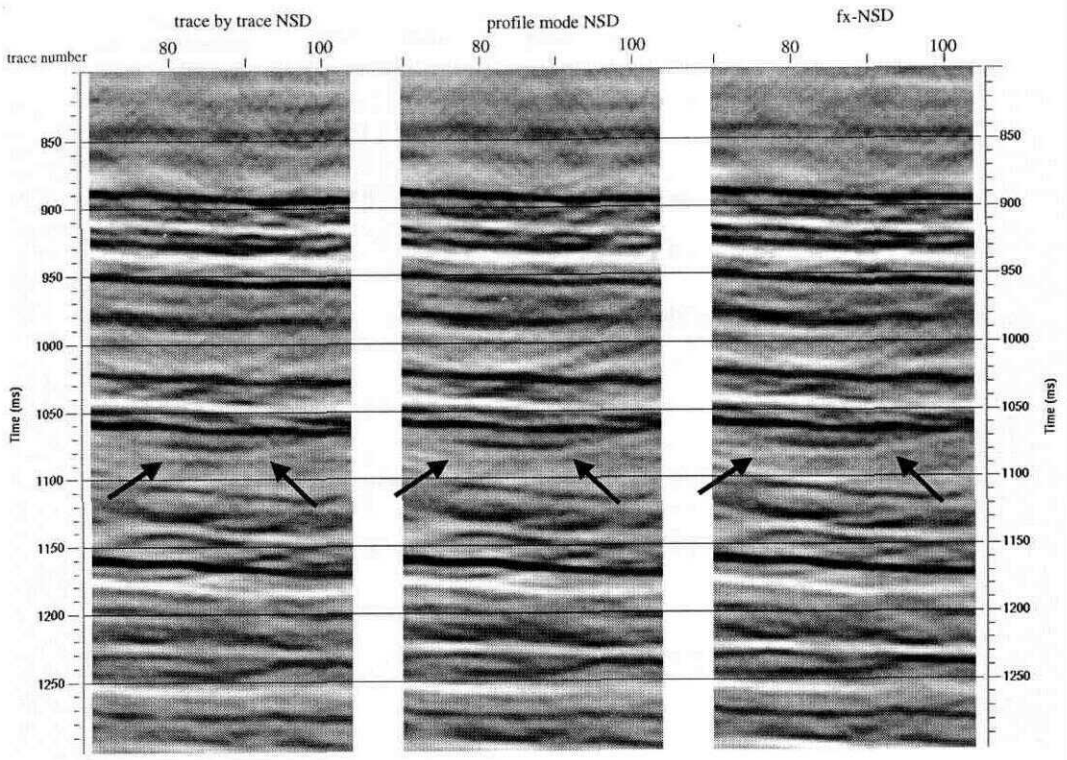

Figure 5.16: A comparison of profile-mode NSD, trace-by-trace NSD and fx-NSD in the channel zone. The feature thought to be the channel is pointed out with arrows.

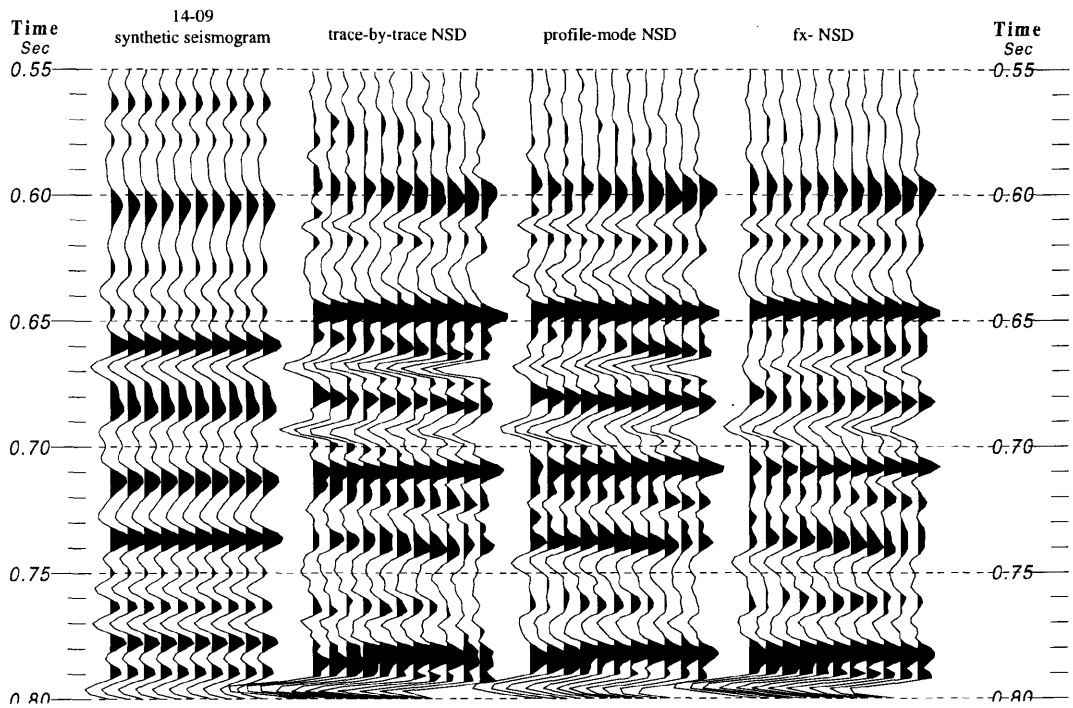

Figure 5.17: The 14-09 synthetic compared to trace-by-trace NSD, profile-mode NSD and fx-NSD. Ten traces centered at the well for each NSD result are shown.

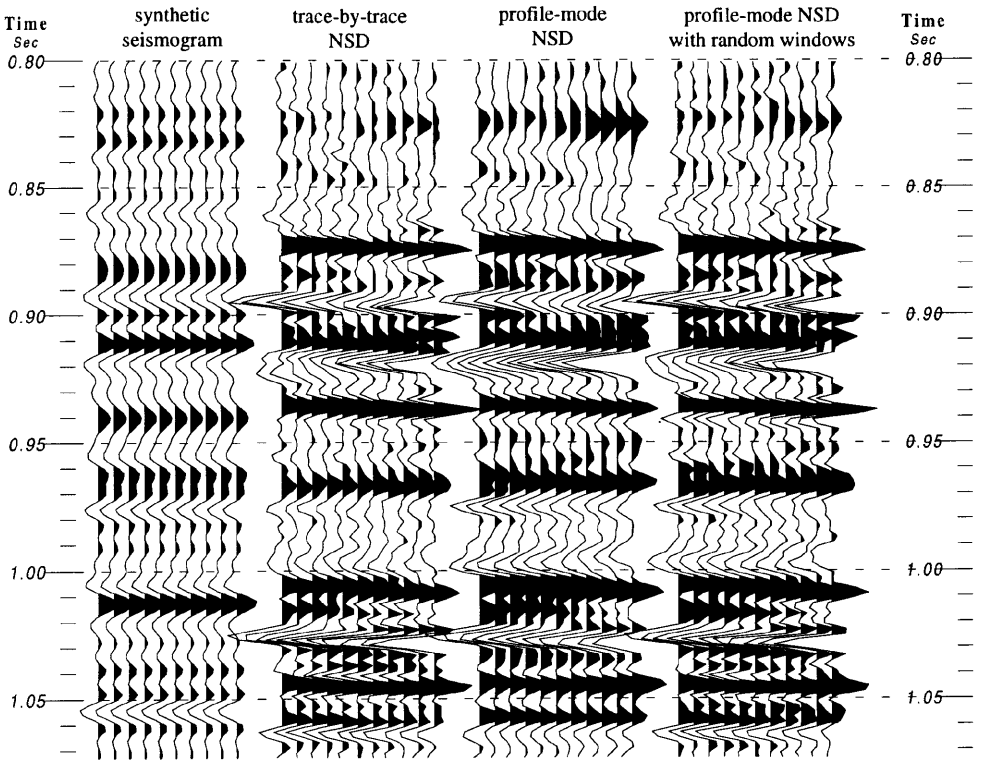

Figure 5.18: The 4-16 synthetic compared to trace-by-trace NSD, profile-mode NSD and fx-NSD.

CHAPTER 6: CONCLUSIONS AND FUTURE WORK

6.1 Conclusions

NSD has been developed as an extension of stationary Fourier domain deconvolution. It uses a data-dependent operator derived from the time-variant amplitude spectrum, |TVS| of the input trace to approximately correct for the effects of attenuation, dispersion, multiple effects and source signature.

The first step in the NSD algorithm is to calculate the |TVS| of the gained input trace. This |TVS| is then smoothed in an attempt to separate the reflectivity from the source signatrue and anelastic attenuation. Two versions of the deconvolution method are available and they differ in the way the nonstationary spectrum of the input data is smoothed in the operator design stage. The first version, the simple-smoothing method, directly smoothes the |TVS| of the input trace. The alternate version, the residual-smoothing method, is a type of data-driven inverse-Q filter. The residual-smoothing method removes an estimated exponential attenuation trend from the |TVS| of the input trace, smoothes the residual spectrum and restores the exponential attenuation trend. The resulting amplitude spectrum of the forward operator from either version can then be coupled with a minimum-phase spectrum (computed digitally from the amplitude spectrum) or left as zero phase before being inverted to form the inverse operator. The

inverse operator is applied continuously to the data using nonstationary filter theory (Margrave, 1998).

NSD is limited by the assumptions described in Section 3.2.2 and by the smoothing process. Smoothing limits the NSD procedure in at least two ways. First, in the residual-smoothing method, an estimate of Q is required. If this estimate is wrong then the smoothing biases the exponential decay surface. However, even if the estimate of Q is correct and the attenuation/gain surface is exactly removed, the smoothing process is still imperfect because the smoothers are of finite length. Infinite smoothers are required to perfectly remove attenuation. In addition, the spectrum to be smoothed is of finite length and so end effects are an issue.

NSD can be applied in two modes, trace-by-trace and profile-mode. In trace-by-trace mode an NSD operator can be designed and applied separately to each trace in an ensemble. In profile mode a single operator can be designed from an ensemble and applied to each trace. The profile-mode NSD approach is useful when a physical model indicates that a single operator is more appropriate. Profile-mode NSD reduces trace-to-trace differences induced by the operator and has a statistical advantage in the operator design.

NSD has many parameters and testing has been performed to see how parameter changes affect the NSD results. The effects of the time and frequency smoother lengths, smoother geometry, window length, window increment, exponential gain constant, errors

in the estimate of Q, minimum-phase or zero-phase NSD operator, residual-smoothing or simple-smoothing, and sensitivity of NSD to finite numerical precision were investigated.

A brief summary of the results from these parameter tests will be listed. The time smoothers should be similar in length to the duration of the reflectivity packages for the simple-smoothing version and much longer than the reflectivity packages in the residual-smoothing version. The frequency smoother length should be kept very short (~5Hz) for both simple and residual-smoothing. A Hanning smoother appears to perform better than a boxcar smoother. The window length of the |TVS| calculation should be moderate, to provide good resolution of the |TVS| in both time and frequency. The window increment of the |TVS| calculation should very short and provide 80-90% overlap between windows. The trace input to NSD should be gained so that the trace is balanced and not growing or decaying with time. A minimum-phase operator appears to correct for minimum-phase dispersion with more success than the zero-phase operator. The residual-smoothing version of NSD provides results superior to smoothing with the simple-smoothing method. NSD cannot correct for amplitudes with extreme decay due to finite numerical precision of computing facilities.

NSD has proved effective as applied to the Blackfoot broadband survey. It enhanced the vertical resolution of the stacked section as compared to the combinations of gain and Wiener deconvolution, and Wiener deconvolution and inverse-Q filtering. In addition, the section deconvolved with NSD has improved reflectivity character as compared to the other techniques. This is evident from the close-up view of the channel

and from the ties to the synthetic seismograms. In addition, the average |TVS| of NSD is more even and consistent than the average |TVS| of the other methods. NSD delineated the target channel more clearly than the other processing techniques. The success of NSD as compared to the other techniques is related to the physical model on which the operator is built and its data-driven nature.

NSD has advantages over similar processing techniques. It approximately corrects for anelastic attenuation and source signature simultaneously. In addition, the operator is continuously time-variant and applied without the use of windows. As well, NSD can handle nonstationary multiples in addition to stationary multiples. A further advantage is that the operator is data-driven and based on a strong physical model. It seems to be robust with respect to errors in the estimate of Q.

6.2 Future work

Although much of the groundwork has been laid out in this thesis there are many possibilities left to explore regarding NSD. A few ideas for future work are listed below, although they certainly do not comprise a comprehensive list of possibilities.

A fundamental change to the algorithm would be to design the NSD operator using a wavelet transform instead of using a |TVS|. The flexibility of the choice of mother wavelet in the wavelet transform, and the excellent joint time-frequency resolution of this method may offer advantages for NSD.

The effectiveness of NSD in nonstationary multiple removal needs to be investigated. NSD can potentially handle a wider class of multiples than stationary techniques because the NSD operator is nonstationary.

NSD could be implemented in a surface-consistent deconvolution approach. NSD could be applied as the midpoint-consistent term to correct for Q attenuation.

As mentioned in the conclusions, the smoothing process of NSD is imperfect. Well log data, if available, may offer an alternate method in separating reflectivity from attenuation effects. The |TVS| of the input trace could be divided by the |TVS| of the reflectivity instead of, or in addition to, smoothing.

REFERENCES

Aki, K., and Richards, P. G., 1980, Quantitative Seismology, Theory and Methods, **2**, W. H. Freeman and Company.

Barnes, A. E., 1992, The calculation of instantaneous frequency and instantaneous bandwidth: Geophysics, **57**, 1520-1524.

Bickel, S., H., 1993, Similarity and the inverse-Q filter: the Pareto-Levy stretch: Geophysics, **58**, 1629-1633.

Bickel, S., H., and Natarajan, R., R, 1985, Plane-wave Q deconvolution: Geophysics, **50**, 1426-1439.

Chakraborty, A., and Okaya, D., 1995, Frequency-time decomposition of seismic data using wavelet based methods: Geophysics, **60**, 1906-1916.

Claasen, T. A. C. M., Mecklenbrauker, W. F. G., 1980, The Wigner distribution-a tool for time-frequency signal analysis, Part I: Continuous-time signals; Philips J. Res., **35**, 217-250.

Claasen, T. A. C. M., Mecklenbrauker, W. F. G., 1980, The Wigner distribution-a tool for time-frequency signal analysis, Part II: Discrete-time signals; Philips J. Res., **35**, 276-300.

Claasen, T. A. C. M., Mecklenbrauker, W. F. G., 1980, The Wigner distribution-a tool for time-frequency signal analysis, Part II: Discrete-time signals; Philips J. Res., **35**, 276-300.

Cohen, L., 1995, Time-Frequency Analysis: Prentice Hall.

Eisner, E., 1984, Minimum phase for continuous time and discrete time functions: Geophysical Prospecting, **32**, 533-541.

Ellender, S. A., 1986, Considerations in estimating the minimum- phase properties of sampled data: Geophysical Prospecting, **34**, 1200-1212.

Futterman, W. I., 1962, Dispersive body waves: Journal of Geophysical Research, **73**, 3917-393.

Gelius, L.J., 1987, Inverse-Q filtering. A spectral balancing technique, Geophysical Prospecting, **35**, 656-667.

Graps, A., 1995, An introduction to wavelets: IEEE computational science and engineering, **2**, 50-61.

Hale, D., 1981, An inverse-Q filter: Stanford Exploration Project, **26**, 231-243.

Hale, D., 1982, Q adaptive deconvolution: Stanford Exploration Project, **30**, 133-158.

Hargreaves, N. D., 1992, Air-gun signatures and the minimum-phase assumption: Geophysics, **57**, 263-271.

Hargreaves, N. D., 1992, Similarity and the inverse-Q filter: some simple algorithms for inverse-Q filtering: Geophysics, **57**, 944-947.

Hargreaves, N. D., and Calvert, A. J., 1991, Inverse-Q filtering by Fourier transform: Geophysics, **56**, 519-527.

Hatton, L., Worthington, M. H., and Makin, J., 1986, Seismic Data Processing: Theory and Practice, Blackwell Scientific Publications.

Karl, J. H., 1989, An introduction to digital signal processing, Academic Press.

Kets, F. B., 1987, Deconvolution of sampled signals: E.A.E.G.49th Meeting.

Kjartannson, E., 1979, Constant Q wave propagation and attenuation: Journal of Geophysical Research, **84**, 4737-4748.

Knopoff, L., 1964, Reviews of Geophysics, **2**, 625-660.

Lay and Wallace, 1995, Modern Global Seismology, Academic Press.

Levin, S., 1989, Surface consistent deconvolution: Geophysics, **54**, 1123-1133.

Lewalle, J., 1995, Tutorial on wavelet analysis of experimental data: http://www.mame.syr.edu/faculty/lewalle/tutor.html.

Margrave, G. F., 1998, Methods of Seismic data processing, Geophysics 657 course lecture notes: University of Calgary

Margrave, G. F., 1998, Theory of nonstationary linear filtering in the Fourier domain with application to time variant filtering: Geophysics, **63**, 244-259.

Margrave, G. F., 1999, Seismic signal band estimation by interpretation of f-x spectra: Geophysics, in press.

Mitchel, A. R., and Stokes, W. D., 1986, Sampling and minimum phase from both a continuous and discrete point of view: Geophysical Prospecting, **34**, 807-821.

Peacock, K., and Treitel, S., 1968, Predictive deconvolution-theory and practice: Geophysics, **34**, 155-169.

Polikar, R., 1994, The engineers ultimate guide to wavelet analysis: http://www.public.iastate.edu/~rpolikar/WAVELETS/Wttutorial.html.

Ricker, N., 1977, Transient waves in visco-elastic media: Developments in solid earth geophysics, **10**, Elsevier, Amsterdam.

Robinson, E. A., 1966, Multichannel z-transforms and minimum-delay: Geophysics, **31**, 482-500.

Robinson, E. A., 1967, Predicitive decomposition of time series with application to seismic exploration: Geophysics, **32**, 418-484.

Sheriff, R. E., and Geldart, L. P., 1995, Exploration Seismology, University Cambridge Press.

Schoenberger, M., and Levin, F. K., 1974, Apparent attenuation due to intrabed multiples: Geophysics, **39**, 278-291.

Stewart, R., 1983, Vertical seismic profiling: the one-dimensional forward and inverse problems, Unpublished Ph.D. thesis from Massachusetts Institute of Technology.

Stewart, R., Ferguson, R., Miller, S., Gallant, E., Margrave, G., F., 1996, The Blackfoot seismic experiments: broad-band, 3C-3D and 3D VSP surveys, CSEG Recorder (June, 1996).

Taner, M. T.,Koehler, F., and Sheriff, R. E., 1981, Surface consistent corrections: Geophysics, **48**, 17-22.

Taner, M. T.,Koehler, F., and Sheriff, R. E., 1979, Complex seismic trace analysis: Geophysics, **44**, 1041-1063.

Toksov, M. N., and Johnston, D. H., 1981, Seismic wave attenuation, Geophysics Reprint Series No. 2.

Tonn, R., 1991, The determination of the seismic quality factor Q from VSP data: a comparison of different computational techniques: Geophysical Prospecting, **39**, 1-27.

Torrence, C., Compo, G. P., 1998, A practical guide to wavelet analysis: Bulletin of the American Meteorological Society, **79**, 61-78.

Trorey, A. W., 1962, Theoretical seismograms with frequency and depth dependent absorption: Geophysics, **27**, 766-785.

Waters, K., 1992, Reflection Seismology. A Tool for Energy Resource Exploration, Krieger Publishing Company.

White, R. E., 1992, The accuracy of estimating Q from seismic data: Geophysics, **57**, 1508-1511.

Yilmaz, 0., 1987, Seismic Data Processing, Society of Exploration Geophysicists.

Ziolkowski, A., 1991, Why don't we measure seismic signatures?: Geophysics, **56**, 190-201.